Quantifying Galloway: Fluvial, Tidal and Wave Influence on Experimental and Field Deltas

A DISSERTATION
SUBMITTED TO THE FACULTY OF
UNIVERSITY OF MINNESOTA
BY

Sarah E Baumgardner

IN PARTIAL FULFILLMENT OF THE REQUIREMENTS
FOR THE DEGREE OF
DOCTOR OF PHILOSOPHY

Adviser: Professor Chris Paola

April, 2016

Acknowledgements

No research project exists in a vacuum, and there are more people who have contributed to data collection and analysis than can be listed here. Without the assistance and technical expertise of Dr. Chris Ellis and Mr. Jim Mullin, however, the experiments that make up this dissertation would not have been possible.

Dedication

From source to sink:
To my parents, who started me down this road, in all senses of the phrase, and who have rolled along beside me ever since. To Ms. Anita Honkonen, who introduced me to the wonders of stream tables and in doing so breached the levee to lead me out into the wide world of Earth-surface dynamics. And to the technical staff and assistants at the St. Anthony Laboratory: you helped me out of more eddies than I thought could possibly exist, and now you finally get to be rid of me.

Table of Contents

List of Tables

List of Figures

Chapter 1:

Deltas are vital: Among the landforms most important to life on Earth is the delta. Their position at the crossroads of land and open water allow an incredible amount of mixing: of sediment and water, of marine and terrestrial, and of plant and animal life. The sediment carried by the river and deposited at its mouth drives the incredible biological productivity that makes this land such a priceless resource. Deltas are prime real estate for agriculture and aquaculture, and as such are among the most consistently and densely populated areas in the world. (Syvitski and Milliman, 2007).

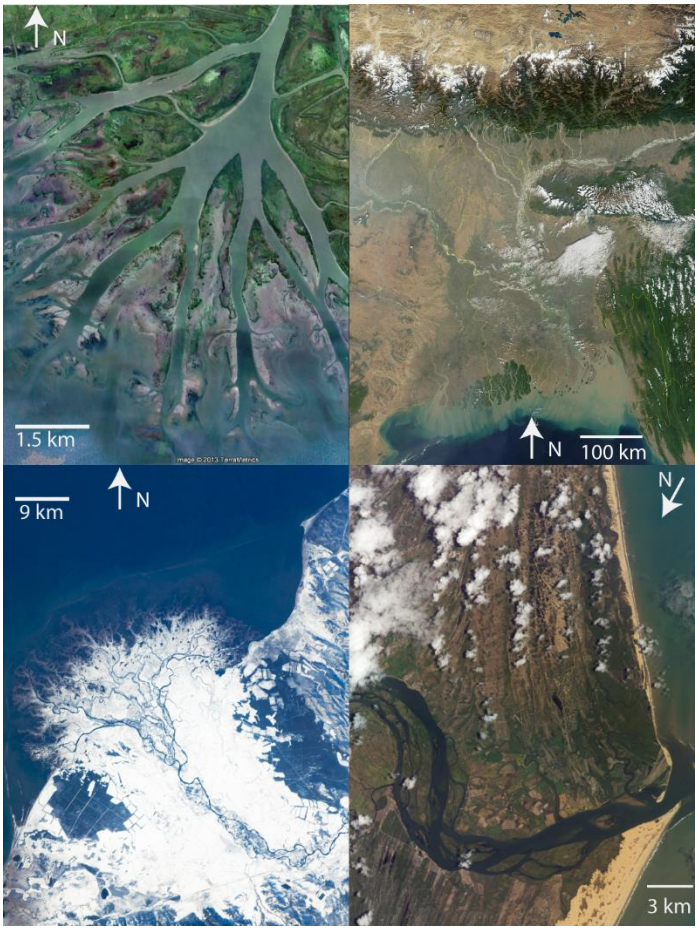

Figure 1: Clockwise from the upper left, the Wax Lake Delta, Mississippi, USA, the Ganges-Brahmaputra-Meghna Delta, the Sao Francisco Delta and the Selenga Delta.

Deltas are vulnerable: The low elevation and relief that allow consistent deposition of sediment onto the floodplain are also a source of vulnerability to global eustatic sea level rise. With slopes on the order of 10^{-5}, even a modest 0.1m increase in sea level can affect areas 10 km inland (Wilson and Goodbred, 2015). Multiplied over the width of a delta, this is an enormous amount of land lost to agriculture, aquaculture and recreation.

Deltas are valuable: Humans depend on modern deltas for food production, but they depend on ancient deltas for energy. Much of the oil, gas and other petrochemicals needed for daily life as we know it come from delta deposits that formed and were buried millions of years ago (Rainwater, 1966). We use these products not only for comfort and convenience, but to drive the global economy.

Deltas are therefore fully integrated into the lives of nearly every person on the planet, either directly through the food they eat or indirectly through the products they consume—but what are deltas? The most basic definition of a delta is the landform that results when sediment-laden water slows as it enters a standing body of water and can no longer transport the entirety of its sediment load.

Deltas in the field evolve over timescales of tens to tens of thousands of years (Reitz and Jerolmack, 2012, Paola *et al*., 2009). We are therefore limited to studying the dynamics of field-scale deltas through the imperfect lens of the rock record (Bhattacharya and Walker, 1991, Legler *et al*., 2013, Longhitano *et al*., 2012), or through computational (Ashton *et al*., 2013, Hutton and Syvitski, 2008, Edmonds and Slingerland, 2010) and physical analogs (Martin, *et al*., 2009, Kim *et al*., 2012), which evolve much more quickly and allow the study of their dynamics. We create small deltas in a laboratory setting in which the major parameters governing delta evolution are strictly controlled. These physical experiments are not models: spatial and temporal scaling is not (and cannot be) explicit. Instead, they are related to their counterparts in the field through parameters such as channel depth and avulsion timescales (Paola *et al*., 2009).

Deltas form when the net sediment transport into an area is greater than the rate of

creation of accommodation by subsidence or by base level rise (Miall, 1976). Subaerial deltas cannot form where space is being created faster than the net rate of sediment delivery. Subsidence is driven by regional tectonics as well as by the local tectonics created by the weight of the delta itself (e.g., Cohen and McClay, 1996). Accommodation may also be created (or removed) by base level change at the local (Walcott, 1972) or global levels (Han and Wu, 1995).

Not every river mouth is associated with a delta: sediment deposited into a basin by the river may be removed or redistributed by many processes: Aeolian transport, ice from the river (Baeltaos, 1997), and from the basin (Reimnitz and Bruder, 1972), wind-driven waves (Neinhuis, *et al*., 2013, Ashton and Murray, 2006), tidal currents (Wright *et al*., 1973, Fagherazzi *et al*., 2004), human intervention (Syvitski *et al*., 2005) and the river itself (Shaw and Mohrig, 2014). Because each of these processes has different mechanisms by which they mobilize sediment, they should have different geomorphic signatures. In the following chapters, we focus on the morphological impact on the delta of the fluvial input, the tidal regime and the wave climate because they are considered the primary influences to which deltas are exposed.

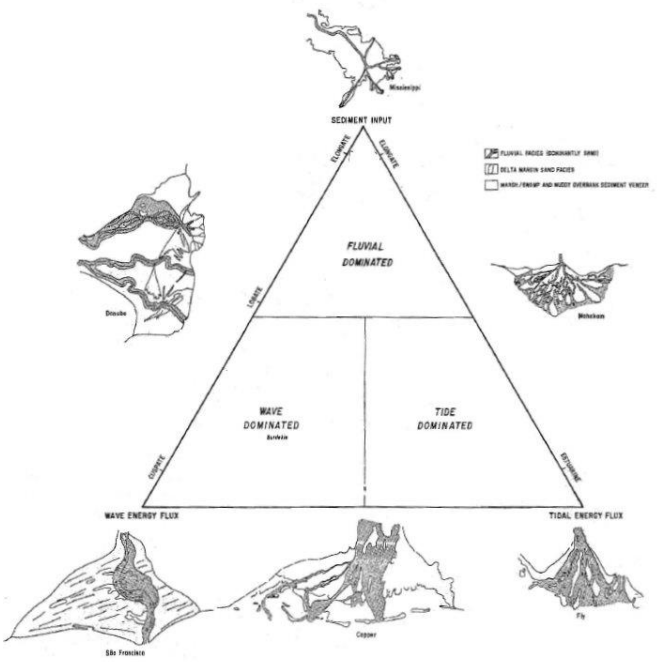

Figure 2: Galloway's (1975) original ternary diagram.

The river-wave-tide paradigm was first proposed by Wright and Coleman (1972) and Galloway (1975) (Fig. 2). Since then, it has been widely adopted, primarily because the effects of waves and tides on delta morphology appear to be readily discernable in plan view and are of first-order importance for both modern and ancient deltas. The central goal of this thesis is to quantify that paradigm. To do this, we must develop two sets of metrics: one for the process strength, and one for the geomorphology they produce. For the latter, we focus on planform information, including planform change with time. In order to maximize the utility of these metrics, we derive them specifically for use with data that is widely available (e.g., wave and tide height) or measurable from satellite imagery. Following the work of Davis and Hays (1984), the energy metrics must have the same units for direct comparison of the process strengths. The geomorphic metrics must also describe features of universal delta morphology (*i.e.*, they cannot depend on the existence of an extensive distributary network.) We designed these metrics to be useful in a global context.

Fluvial input to the delta is crucial: without the sediment provided by the river, the

delta would not exist and that portion of the basin could be treated as a part of the rest of the coastline (Boyd *et al*., 1992). The ratio of water to sediment carried by the river controls the delta slope (see, *e.g*., Hutton and Syvitski, 2008), and the size of the sediment particles carried by the river in part determine the cohesivity, and thence the planform morphology (Edmonds and Slingerland, 2010, Orton and Reading, 1992). Channel dynamics (avulsion and migration) control the location(s) of channels within the delta plain (Reitz and Jerolmack, 2013). We derive two metrics for fluvial energy: one based on the frictional dissipation of energy to heat as water flows over the riverbed and the other from the flux of kinetic energy contained within the water as it moves downstream.

The inundation and emergence of a delta during a tidal cycle creates tidal currents: periodically reversing unidirectional flows within a channel. These currents can be either flood- or ebb-dominated, and generally rearrange sediment into features parallel (or anti-parallel) to the current direction (Fagherazzi *et al*., 2004). Morphologies associated with this forcing include funnel-shaped, shoreward-widening channels, often disconnected from the main fluvial flow, and extensive networks of highly sinuous channels (Wright *et al.*, 1973).

The essential feature of tidal forcing is the vertical movement of the water surface; it is the slope created by the passage of the tidal wave over the delta that generates the currents. Current strength is therefore related at first order to the total vertical variation in the water surface. We derive a parameter for the tidal energy impinging upon a delta based upon the potential energy needed to lift the water of the tidal wave from its low

water elevation to its high tide level.

Energy from wind-driven gravity waves strikes the delta at the shoreline. Although the crests of the waves are generally subparallel to the coast and moving towards it, the currents produced by wave action are directed in the alongshore direction. As a consequence, waves tend to produce features which are parallel to the coast, *i.e.*, in the direction of transport (Komar, 1971, Ashton and Murray, 2006, Ashton and Giosan, 2011). Morphological features interpreted as wave-generated include spits, longshore bars, barriers, and beach ridges. We derive and use a modified form of the Coastal Engineering Resource Manual (CERC) equation for wave transport of sediment to quantitatively describe the energy contained within the wave.

We develop metrics that quantify the properties of features seen in planform view. These can be applied to overhead photographs of experimental deltas grown under a variety of fluvial, tidal, and wave regimes as well as to satellite imagery. Because the shoreline is a feature found in all deltas, we focus on deriving metrics to quantify its roughness ("rugosity", or shoreline sinuosity), degree of dissection by distributary channels, and directional distribution.

We apply both geomorphic measures and energy metrics to two experimentally-produced deltas which grow under a range of fluvial, tidal and wave inputs in order to test the relationship between incident energy and morphology.

We tackle the central question of quantifying the effects of waves, tides, and rivers on delta morphology via three interrelated papers. The first, Chapter 2, describes a laboratory experiment in which we successfully used pumps to create a pseudotide that

acted on a self-formed, fluvial delta, which then developed morphologic features (headward-cutting, shoreward-widening sinuous channels) consistent with those observed in the field and interpreted to be tidal in origin. We also describe a change in the channel dynamics of the delta: an increase in channel stability and a decrease in "hard" avulsion rate due to tidal action on the delta. The second paper (Chapter 3) introduces a new global database of river mouth locations, including the presence or absence of a delta at each mouth, along with data on the basinal processes (waves and tides) impinging on the mouth. We present a set of energy-based metrics to describe the relative strengths of those processes compared to the fluvial input, and relate delta presence/absence and morphology to those strengths. The third paper (Chapter 4) describes a second laboratory experiment, this time incorporating the previously described tides as well as waves (generated by an oscillating arm) that impinge upon an actively-evolving delta to create morphologies consistent with field examples that are interpreted to have formed under mixed wave and tidal influence. We use the previously developed energy metrics to quantify both the absolute and relative process conditions under which these features formed and apply the statistical methods introduced in Chapter 3 to overhead imagery of the experiment in progress.

Finally, the thesis closes with a set of overall conclusions from the work in Chapter 5.

Chapter 2:

Title: Morphology and Dynamics of an Experimental Delta Under Tidal Influence

Authors: Baumgardner, S., Abeyta, A. and Paola, C.

Abstract:

The effects of tides on deltas are well known and pronounced in the field-, but the interaction between a fluvial system and an impinging tidal wave under controlled conditions have so far received limited study through either computational modeling or experimentation. In the Delta Basin facility at St. Anthony Falls Laboratory we successfully used a paired set of pumps to simulate the effects of tides on a small experimental delta, which developed a set of morphological features consistent with those seen in the field, including a clearly delimited intertidal zone, and a set of headward-cutting, shoreward-widening blind channels.

Introduction:

Deltas are recognized as some of the most densely populated and heavily farmed landscapes on Earth (Syvitski, *et al.,* 2009). (Fig. 3) Many deltas, including some of the largest and most extensively used by humans, display morphology that indicates significant modification by tidal currents. Classical morphologic indicators of tidal influence include flaring, sinuous to straight channels disconnected from the main fluvial flow, inlets through shoreline-parallel features, and deeply embayed coasts (Galloway, 1975, Boyd *et al*., 1992, Harris, *et al*. 2004). To understand the development and potential future evolution of these deltas in the face of changes to land use and climate,

we must understand the effects of both tidal and fluvial processes. A more nuanced understanding of the interaction between the two will enhance our ability to predict the likely response of a delta to changing conditions and is essential to the management of these valuable tracts of land. In addition, studies of ancient deltas show clearly that tidal influences have been important in the past (see, *e.g.*, the review by Longhitano *et al.*, 2012). Understanding the interplay of tides with rivers in shaping deltas, and its effect on delta evolution, is clearly also an important part of understanding and predicting the architecture of subsurface delta deposits.

Figure 3: The Irrawaddy Delta (Myanmar) displays morphological features associated with tidal influence, including headward-narrowing channels, high channel sinuosity, and a network of 'tie' channels perpendicular to the main flow linking larger distributaries.

The mechanisms of sediment transport and deposition on delta topsets have been the subject of numerous field studies, numerical models, and physical experiments (see, e.g., Geylense *et al*., 2011, Hutton and Syvitski, 2008, Martin *et al.*, 2009, Reitz and Jerolmack, 2011), but these studies have largely focused on the fluvial component. The dynamics of individual tidal inlets and channels have been studied in the field and through the use of numerical modeling. With the exception of the work of Geleynse *et al*. (2010), these have largely focused on tidal inlets and channels away from river mouths, rather than the interaction of such features with fluvial systems. Physical experiments exploring the effects of tides are rare: Vlaswinkel and Cantelli (2011) showed that a network of erosional channels could be produced

experimentally by short-period changes in base level. More recently, Kleinhans *et al*. (2012) report only five other morphodynamic experiments involving tides, and none, including those of Kleinhans *et al.*, involve the interaction of tides with self-formed fluvial channels.

The success of physical experiments in the study of the development and evolution of delta morphology generally is due to their short timescales of evolution (tens of hours to days, rather than the years to decades and longer found in the field) and the control they allow over input parameters (*e.g*., sediment and water supply and base level). The morphology and dynamics of deltas formed under laboratory conditions are also much more easily measured than those of field-scale deltas: topography data for the entire topset does not require extensive field deployments or removal of vegetation cover, and can thus be obtained at relatively high temporal and spatial resolution. Similarly, time lapse photography provides a complete record of the evolution of the subaerial portion of the delta. Incorporating laboratory-generated tides into an experimental basin therefore opens a range of new possibilities for studying the interaction between fluvial and tidal processes on an actively depositing delta.

A major obstacle to adding tides to experimental delta studies has been the apparent difficulty of scaling the tidal period. It is not clear how best to do this. One idea might be to reason as follows: We can establish a rough scaling of experimental time by comparing the time scales of events common to both experimental and field deltas, for example, the time between avulsions (Reitz and Jerolmack, 2012, Kim and Paola, 2007). For a large field-scale delta like the Ganges-Brahmaputra-Meghna or the Mississippi, this time scale

is in the range of 10^3 yr. In the laboratory, it is measured in hours. The time-scale ratio (field/laboratory) is thus of the order of 10^6. A 12-hr tide at field scale translates to a laboratory tidal period of less than a second, which is not only impractical but also would produce a surface gravity wave (*i.e*. a flow dominated by temporal acceleration) rather than a tide. Thus, one must look beyond this kind of formal scaling and ask what, fundamentally, gives the tide its morphodynamic characteristics? From the point of view of coastal morphodynamics, a first-order definition of a tidal cycle is a relatively high frequency fluctuation in base level that creates reversing, unidirectional currents roughly perpendicular to the shoreline, that occurs on a time scale that is long enough to produce a quasi-steady current but shorter than the main morphodynamic time scales for the delta, such as the avulsion time scale. Additionally, to shape morphology, these currents must be able to move sediment on both phases of the tidal cycle. These conditions can be created in a laboratory delta by adding and removing water from the basin over very short timescales, such as the method described below or by mechanically inducing currents by tilting the basin (as developed and described by Kleinhans *et al*., 2012.)

Methods:

The Delta Basin facility at St. Anthony Falls Laboratory at the University of Minnesota consists of a 5 m by 5 m by 0.5 m basin connected to a smaller (2 m by 2 m by 0.5 m) auxiliary basin via a system of pumps (Fig. 4). The experimental deltas are grown from a corner of the larger basin, which is equipped with a motorized weir for base level control. The weir, sediment feeder and water supply are controlled by a computer (as described in Martin, *et al*., 2009) to ensure precise control. The basin is also equipped with a water-elevation meter accurate to 0.1 mm, an overhead digital camera with a wide-angle lens, and a data cart with laser topography scanners.

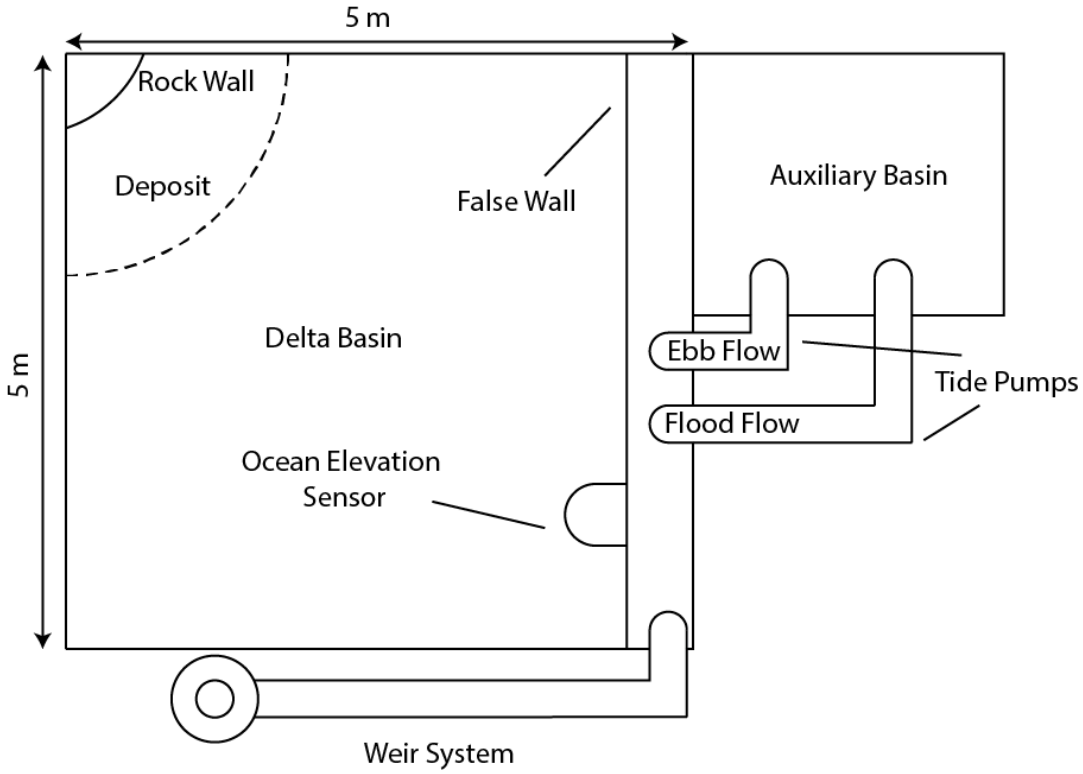

Figure 4: Diagram of delta basin facility. Water and sediment enter at the upper left.

Sand-sized walnut-shell ($D_{50} \approx 1$ mm) particles were the primary sediment used to create the deltas. This material was selected for its low density (1350 kg/m^3), which makes it mobile enough to be entrained and re-deposited under tidal action, including the weaker flood phase. As a consequence of its organic nature, however, this sediment begins to age upon contact with water: an area not reworked for >20 hours darkens in color and develops a film of bacterial growth, which creates weak cohesion.

Before each run, a wedge or step of coarse (1-2mm) quartz sand, roughly 2m in radius and 140mm in height, was placed in an arc around the sediment and water source, and capped with several centimeters of the same walnut shell sand as was to be used in the experiment. The purpose of the wedge is to fill part of the target volume for the delta and thus eliminate the need for a lengthy initial phase of the experiment, to ensure that the delta rapidly progrades in the first hours of the experiment, and to provide a layer of well-draining material to assist in post-experimental cleanup. The walnut sand cap ensures that the sediment composing the bed and banks of newly-formed channels matches that in transport.

During the run, water, dye, and sediment were thoroughly mixed in a funnel and coil of PVC tubing before entering the basin through a momentum-diffusing gravel column. The dye was highly concentrated food-grade colorant (Acid Blue 9) delivered by an IV pump; this added a negligible amount to the total water flux. Aside from the placement of roughness elements along the walls of the basin, the water and sediment were allowed to deposit sediment, form channels, and select preferred flow paths without interference. The delta was allowed to completely cover the preformed step with

fluvially deposited sediment before tidal forcing was begun.

Scaling for this experiment was not strict: rigorous geometric scaling of even the smallest of deltas would require an impractically small median experimental grain size. In addition, our objective in these experiments is to recreate a suite of deltaic environments and study generic processes, rather than to make a model of any particular field example. Comparisons to field-scale deltas can be made through features (e.g. channels) and dynamics common to both: our representative vertical length scale is the channel depth; the time scale is the time it takes for the channel(s) to resurface the entire delta topset (see Wickert, *et al*., 2013) for a discussion of similar methods). In this experiment, the tidal ranges were constrained to be comparable to maximum channel scour depths (20-40 mm). The tidal period was very short (120 s) in comparison to the fluvial response time (on the order of 10^4s) so that the topset of the delta was unable to fully adjust to either high or low tide water surface elevation. In this way, tidal forcing is differentiated from base level cycles: although they are both fluctuations in water surface elevation, as discussed above, tidal forcing occurs over time scales that are short compared to those of overall delta evolution.

Tide generation:

Tidal forcing was produced by varying the water surface elevation within the main basin by transferring water to and from the auxiliary basin through computer-controlled pumps, one for each limb of the tidal wave. These pumps were programmed such that the water elevation in the main basin varied in a pseudo-sinusoid around a mean base level,

with user-defined period and amplitude. The tidal sinusoid was broken into 12 linearized sections, and the pump discharge rate determined for each section so as to produce the desired rate of rise or fall given the current water-surface area. Deviation of the water surface from the target elevation in each section was then used as feedback data to refine the pump discharge for subsequent tidal cycles. Average elevation errors during tidal forcing were under 0.5 mm.

This method of generating tides differs significantly from that employed by Kleinhans *et al*. (2012). In those experiments, the basin itself is tilted back and forth across a shoreline-parallel axis in order to cause flow perpendicular to the shoreline. The flow is enhanced by returning water that exited the lower side of the basin to the higher side—making the supply of water from the basin effectively infinite and thus prolonging the length of ebb and flood tides. The amplitude of the tide in Kleinhans' system is defined as the (maximum) vertical distance over which the bed is tilted; both the reported amplitude and period are of the same order as those used in our experiments. While the Kleinhans method is more effective in mobilizing sediment on both flood and ebb limbs of the tide than our base level fluctuation method described above, the tilting required to produce the tidal currents makes it unsuitable for investigations of systems undergoing simultaneous fluvial and tidal action—the fluvial slope would be ill-defined–and it is impractical for large experiments.

The tidal range and period were constrained by the velocity of the tidal currents needed to entrain sediment, and the capacity of the pumps. The pumps have a maximum discharge that limits the rate of change of water surface elevation to 0.66 mm/s for typical

water-surface areas (equivalent to a 40 mm range, 120 s period tide). While the pump system has no lower limit for discharge, very low tidal amplitudes (or very long tidal periods) would generate tidal currents with insufficient shear stress to mobilize sediment. Tidal ranges greater than 40mm were not possible because the volume of the auxiliary basin would be insufficient to store the water at low tide.

Data Collection:

For the experiments described in this paper, topographic scans were taken every 5 run hours at a resolution of 2 mm by 2 mm by 0.1 mm; overhead images were taken every 30 seconds under non-tidal conditions and every 10 seconds under tidal conditions, with an image resolution of approximately 1mm/pixel. Water and sediment input fluxes were kept constant throughout the experiments to minimize potential interactions between the imposed upstream and offshore conditions; for further discussion of run parameters see Table 1 and below.

Run Hour	Parameter	Description	Value
All	BL	Base Level	0.150 m
All	Q_w	Water discharge	10^{-4} m^3/s
All	Q_s	Sediment discharge	10^{-6} m^3/s
All	D_{50}	Sediment Size	10^{-3} m
All	ρ_s	Sediment Density	1350 kg/m^3
0-80	H_T	Tide Height	0
80-90	“	“	0.005m
90-120	“	“	0.0075m

Table 1: Experimental parameters used during the run.

Data Analysis:

Time-lapse photography from an overhead camera (Fig. 5) was orthorectified using standard image-processing methods: prior to the experiment, a regular grid of crosshairs with known spacing and position was placed in the basin, and the camera and lens distortion was calculated from the apparent deflection of these points. We then analyzed the corrected images via pixel-counting methods to create a timeseries of subaerial (topset) area, as well as to find average channel widths.

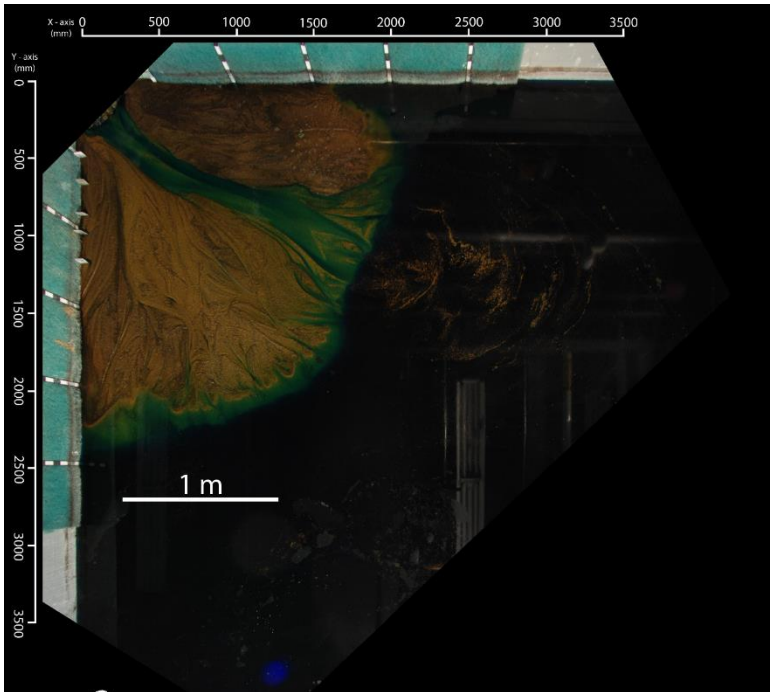

Figure 5: Orthorectified image of the experiment in progress, run hour 60. Note the color difference between water (turquoise) and sediment (tan/brown). Flow is from the upper left corner. Deposit radius is ≈ 2 m.

We created binary land-water maps from orthorectified overhead photographs to analyze shoreline and channel dynamics. Each image was split into its red, green and blue channels, and the ratio of the values of the red to blue channels was calculated for each pixel. A single threshold value was defined to discriminate between land and water

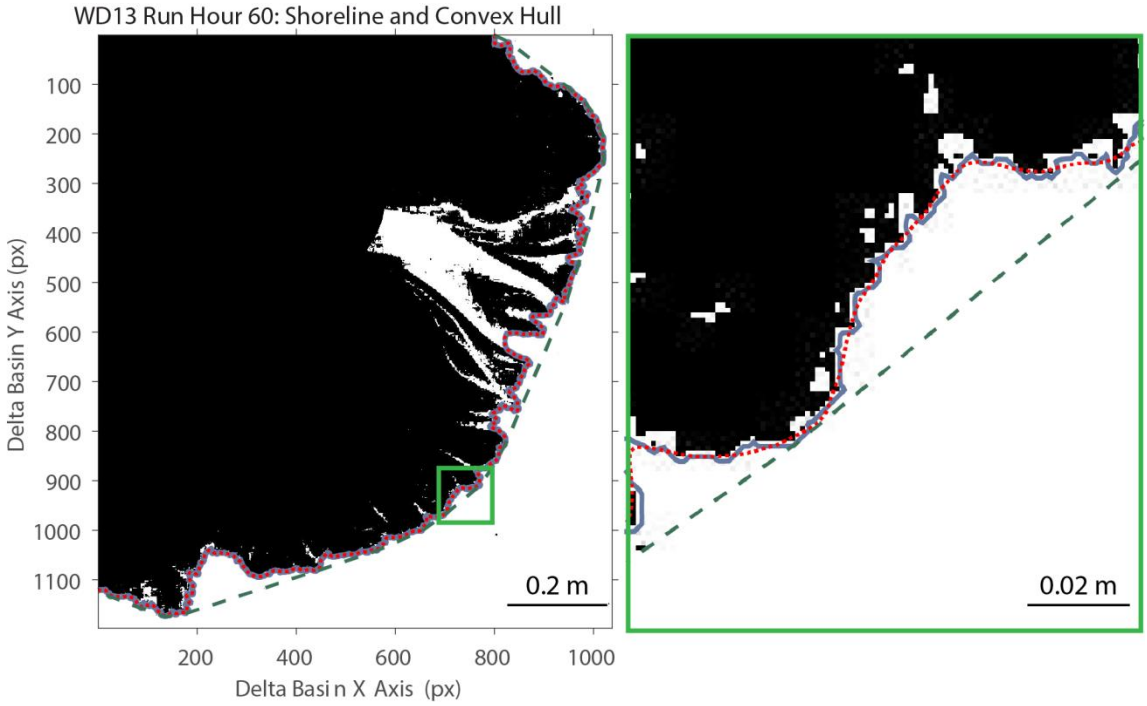

Figure 6: Raw shoreline (solid gray line), smoothed shoreline (dotted red line) and convex hull (dashed green line) plotted on a land-water map. At right, detail of the full image.

based on visual comparison of the computer-picked wet maps with the original images. These black and white images were then used to generate time series of the delta shoreline and the position of channel(s) on the exposed portion of the topset of the deposit.

The shoreline was defined using the opening angle method (OAM) of Shaw *et al.* (2008). This method evaluates the total angle through which open water can be viewed from every point along the land-water interface on a binary land-water map. A contour of a threshold angle—here, 45°—is then defined as the shoreline. This method produces a continuous shoreline that extends some distance into channel mouths and around islands, depending on the threshold angle, essentially defining that section of the land-water boundary that is exposed to basinal processes (*e.g.*, tides). Shorelines were defined

with this automatic method, rather than hand-picking the land-water boundaries, because the pixel-by-pixel results of the method allowed further analysis of the distribution of land and water within the topset. Because Shaw's method is computationally intensive, the shoreline was defined only once every ten run hours.

We define shoreline rugosity as the length of the shoreline (as measured at the highest spatial resolution) normalized by the length of the convex hull that encloses the same area. The use of the convex hull, rather than the linear distance between the two 'ends' of the shoreline, eliminates the effect of the gross shape of the delta; rugosity is therefore a measure of shoreline geometry at scales smaller than that of the entire deposit (Edmonds *et al.*, 2011).

We calculated fractal dimension of the shoreline via a simple box-counting method as described by Feder (1988). The length of the shoreline as defined above is measured with a succession of rulers and the lengths plotted against the ruler size on logarithmic axes. We fitted a line to the data using a simple least-squares regression; the fractal dimension is (1- m), where m is the slope.

Curvature is the rate of change in direction with respect to arc length. Because differentiation amplifies noise, we smoothed the shorelines using a Savitzky-Golay filter (order = 2, filter size = 51) before calculating the direction as a function of the distance traveled along the shoreline. Example raw and smoothed shorelines are shown in Figure 6 along with the associated convex hull. The direction data were detrended to remove the effects of the overall shape of the delta, and the mean value set to zero. To calculate the curvature, we applied a smoothing differentiator developed by Holoborodko (2008) to the

smoothed, detrended direction data.

Channel stability was evaluated by measuring the change in location of water pixels on the topset through time. A series of binarized land-water maps with a 120 s interval was created using the method described above. This interval was chosen to coincide with the tidal period; we selected images from the tidal portion of the run to be as close to low tide as possible for each cycle. We compared each image to the preceding and following images to find the area which changed state (from water to land or vice versa) between successive images. The changed area was then normalized by the total area of the topset and by the time between the images.

Results:

Under purely fluvial conditions, the delta grew radially at a rate proportional to the square root of runtime, consistent with the growth laws predicted by the work of Muto and Steel (1992) (see also Lorenzo-Trueba *et al*., 2012 and Kim and Jerolmack, 2008 for discussion of potential complications to this model). Figure 7 shows the topset area throughout the experiment; because the delta was nearly radially symmetric, linear areal growth indicates that radius is proportional to the square root of run time. Once tides were introduced topset area fell dramatically due to redistribution of sediment to form a wide shelf. However, if the area exposed at low tide is included, there is no loss of topset area.

Average along-channel slopes varied between 9.8×10^{-3} and 1.9×10^{-2} for the purely fluvial run segments, and between 9.4×10^{-3} and 1.5×10^{-2} for the tidal segments.

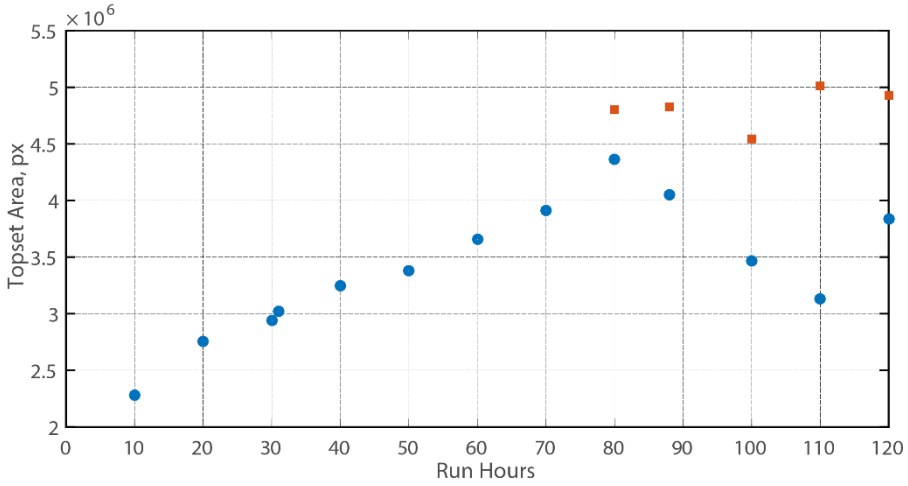

Figure 7: Plot of topset area against run time. Blue circles represent the area above the mean base level; orange squares the area above the low tide level.

Although total water discharge remained constant, channel cross sections were dynamic—typical widths ranged from 0.05 m to 0.2 m, depths were on the order of 10^{-3} to 10^{-2} m and flow velocities varied between 0.1-0.3 m/s.

During the fluvial portion of the run and in areas above the intertidal zone, the flow style varied among diffuse sheet-like flow (during the earliest stages), braiding behavior, and single-threaded channel flow (Fig. 8, left). The Reynolds number for channels ranged between 10^5 and 10^7, indicating that the flow was fully turbulent. The flow was nearly critical—Froude numbers varied between 0.95 (single threaded) and 1.01 (sheet flow).

Under tidal action, slightly-sinuous, headward-cutting channels developed in the intertidal zone. These channels were not related to fluvial discharge—they were disconnected from fluvial channels unless avulsion or continued growth forced a connection (Figure 8, below, shows an example of capture of fluvial flow by such a channel). These tidal channels are persistent: once formed they evolve over >10 run

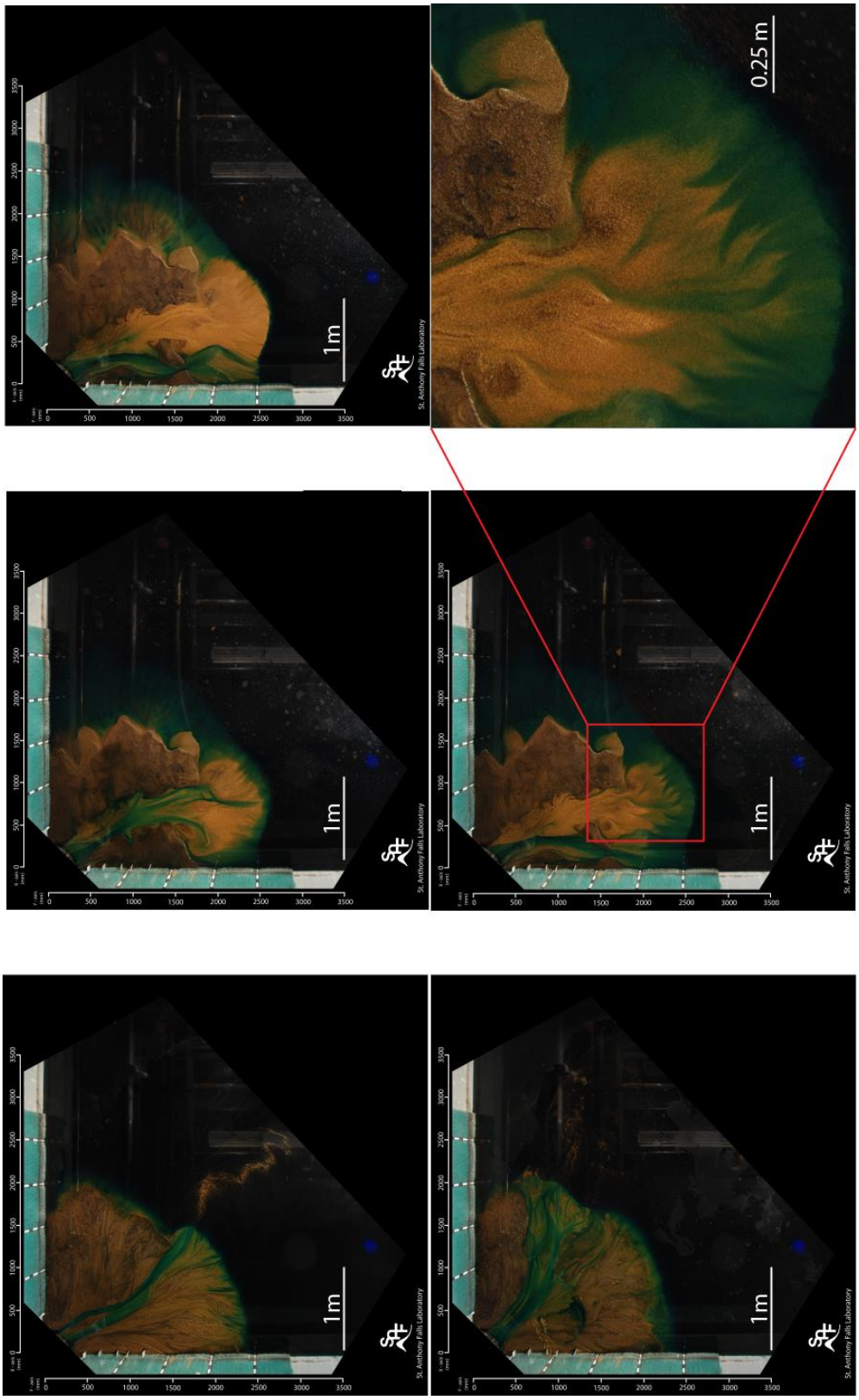
1m
St. Anthony Falls Laboratory
0.25 m

Figure 8 (previous page): Overhead images of the delta in progress. At left, flow in single-threaded (top) and braided (bottom) modes. Clockwise from top center, the avulsion of the main fluvial flow into a headward-cutting tidal creek. Bottom right, inset showing detail of tidal channels. Note the slight sinuosity and widening towards the mouth.

hours. Sinuosity increases with age as the meanders grow. These channels also display the shoreward-widening morphology associated with field-scale tidal creeks.

Unlike the main fluvial channel, the tidal channels evolve in place: while the head of the channel moves inland, the mouth of the channel remains relatively fixed. The channels also deepen and widen with time, in contrast to fluvial channels, which tend to backfill as they prograde and fluvial slope decreases.

Both shoreline rugosities and fractal dimensions were significantly higher under tidal conditions in this experiment as compared to their values under purely fluvial conditions (Student t-test, significance level = 0.05; Table 2).

	Fluvial	Tidal
Rugosity	μ=1.5877, σ=0.1552	μ=1.9482, σ=0.1951
Fractal Dimension	μ=1.0595, σ=0.0204	μ=1.1184, σ=0.0392

Table 2: Geometric properties of the shoreline under fluvial and tidal influence.

Histograms of shoreline curvature (Fig. 9) for both fluvial and tidal portions of the run were visually similar and indeed the combined curvatures of all fluvial and all tidal shorelines from this experiment were found to have no significant statistical difference.

Channel Stability:

Sequential differencing of overhead images of the delta yields a time series of the number of pixels, and thus area, of the topset that changed from wet to dry or vice versa within a given step. Purely fluvial portions of the experiment show a low background rate

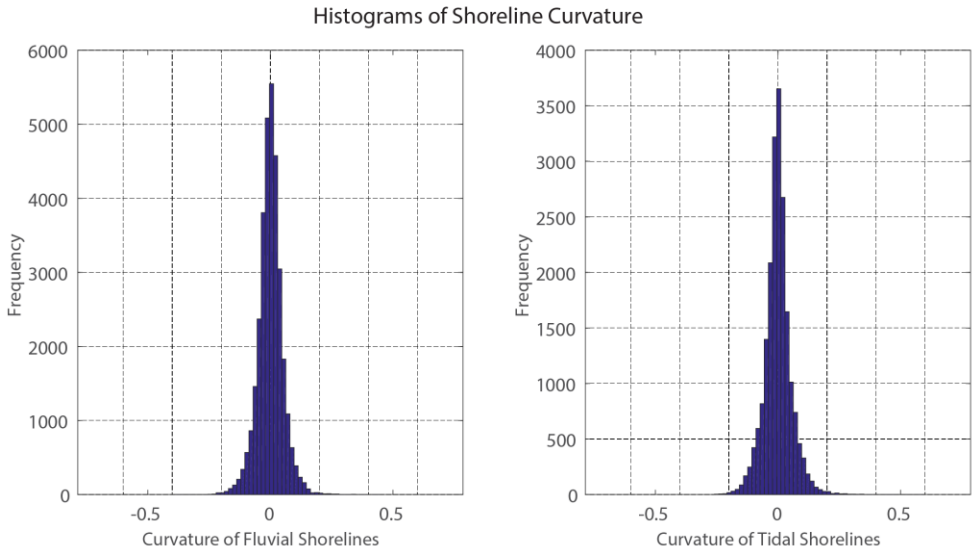

Figure 9: Histograms of shoreline curvature for fluvial (left) and tidal (right) segments of the run.

of change (~3-4%) punctuated by short (5-10 minute) episodes of much greater activity, which are associated with channel avulsions. During tidal action, the background rate of change was higher (5-6%) and excursions from this were of greater duration (tens of minutes) and lower intensity. Avulsive events are defined as peaks that exceed two standard deviations above the mean rate-of-change.

Discussion:

There was no significant, systematic variation in the instantaneous flow conditions (depth, width, and slope) within the channels on the topset between purely fluvial and mixed fluviotidal conditions. While the exact controls on these parameters are still a matter of discussion (e.g., Parker *et al.*, 2007) all three measured quantities have been shown to vary with the water flux through the channel. Although the onset of tidal forcing increased this rate, the additional volume of water transported by the main fluvial

channel(s) due to the tidal wave (as calculated from the tidal prism within the channel) is a small portion (~5-10%) of the background fluvial discharge. This likely accounts for the lack of significant change in (fluvial) channel geometry. Instead, most of the additional water discharge associated with the tidal forcing is accommodated by creating the additional channels of the tidal network.

The headward cutting tidal channels appear to be the result primarily of ebb tidal flow. During ebb tide, the water placed on the topset but outside a channel drains back toward the basin (D'Alpaos *et al*., 2005). Small dips in the surface of the topset—generally former channel mouths—focus the flow and, in so doing, promote the entrainment and removal of sediment. The depressions grow as they capture more and more of the retreating tidal flow, in a process nearly identical to erosion at the head of a (fluvial) channel.

Both rugosity and the fractal dimension of the shoreline increased modestly with the introduction of tides. While statistically significant, there seems to be no systematic dependence of shoreline complexity as measured by these two parameters on the tidal range. Most of the increase in both metrics is due to the presence of tidal inlets, which increase the total length of the shoreline by forcing a landward excursion without significantly changing the gross shape of the subaerial portion of the deposit. The co-occurrence of increased presence of erosional/excavational features and higher fractal dimension is not surprising; the type example for a self-similar landscape is an erosional coastline (Mandelbrot, 1967). But overall, the effect of tidal forcing on the delta is mainly to create additional active (tidal) channels rather than to change fundamentally the

geometry of the shoreline.

The rate of change in wetted location is a measure of the activity of the channels: a topset with an unmoving channel would experience wetting and drying only as a consequence of small fluctuations in base level or water discharge. By contrast, a migrating channel results in a systematic change in location of wetting and drying and an overall rate of change above that of a static channel. Avulsive events are characterized as an abrupt change in the location of a channel; therefore they appear as sharp peaks in topset wetting/drying within the time series.

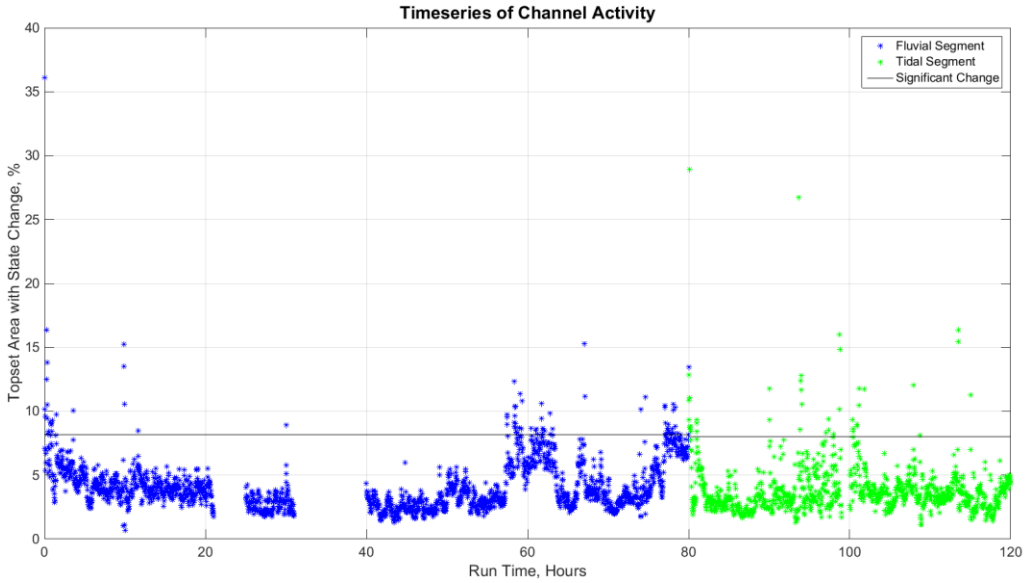

Figure 10: Timeseries of topset proportion wetted or dried in a 2 minute period

The time series of the fluvial portion of the run (Fig. 10, in blue) shows the low rate of change expected of a nearly stationary channel, with the sharp peaks in activity that characterize avulsions. By contrast, the wetting and drying of the topset under tidal action occurs at a lower, but more consistent rate. Channel dynamics on the topset are

therefore dominated by avulsion during purely fluvial run segments and by relatively more consistent lateral migration during periods of tidal influence.

The most likely explanation for this is the disruption by tidal sediment transport of a major mechanism that drives avulsion. Small amounts of sediment deposited at the mouth of a fluvial channel encourage the deposition of more sediment upstream (behind) them (Edmonds *et al*., 2009). As this wedge of sediment propagates upstream, it elevates the bed and can allow the flow to escape the banks of the channel. This often leads to an avulsion at the site of the escape. The incoming (and outgoing) tide does not allow the initial small wedge to persist, and avulsions are therefore much less frequent.

Conclusions:

Using a system of pumps and an auxiliary tank to rapidly raise and lower base level, we have produced experimental deltas that display some of the principal morphologic features of tidal deltas in the field. These deltas vary in both morphology and depositional mechanics from those produced solely under the influence of fluvial processes. From the analysis of overhead imagery and topographic data, we find that:

- Ebb flow causes the formation of downstream-widening, slightly sinuous headward-cutting blind channels at the shoreline
- the shoreline of experimental tidal deltas is more rugose and has a higher fractal dimension but is not significantly different in its distribution of curvature, relative to fluvial-only conditions

- tidal action leads to more consistent short-scale channel variability in time but less frequent large-scale change via avulsion.

Chapter 3:

Title: A new global census of delta occurrence.

Authors: Baumgardner, S., Caldwell, R., Edmonds, D., and Paola, C.

Abstract:

Rivers are of the utmost importance to geomorphology as both sculptors and subjects of the landscape. Their mouths exist at the confluence of terrestrial and marine geomorphic processes and the landforms that occur there reflect both the influence of the river and of the basin. We present a database derived from Google Earth of 6050 active river mouths > 30 m in width, of which 24.7% have deltas as defined by the following criteria: basinward projection of shoreline and presence of a spatial or temporal distributary channel network. We also estimate the strength of the processes influencing them via measures of power/unit length delivered by rivers, waves, and tides derived from global data bases and empirical models. Comparison of basic geometric measures of delta morphology with these forcing energy parameters shows only a weak correlation between relative wave energy and shoreline smoothness.

Introduction:

Rivers occupy a middle ground in geomorphology: they are both agents and subjects of landscape evolution. River deltas are the ultimate expression of rivers as both active and passive elements of the landscape. They represent creation of land via deposition and redistribution of sediments by marine processes. Rivers and deltas are

natural laboratories for the study of sediment transport from the grain to the landscape scale.

While many individual reaches and even entire deltas have been subjects for detailed studies of fluvial dynamics, there have been no broad censuses of the global delta population. Aggregations of data (*e.g.*, the work of Milliman and Farnsworth, 2011; Milliman and Syvitski, 1992, Syvitski *et al*., 2005) have been limited to large rivers and rivers of interest to previous researchers, which in turn have been limited by access to the rivers in question. We present a database of the locations of ~6K rivers of which ~1.5K are associated with deltas and a preliminary analysis of their geographic distribution and geomorphic characteristics. For that subset of the rivers for which data on input parameters (e.g. water discharge, wave and tide inputs), we analyze the dependence of morphology on these inputs.

Methods: Delta Identification

There is no publicly available census of every coastal river in the world—though there are several extensive datasets, such as the one published by Milliman and Farnsworth (2011) and another by Milliman and Syvitski (1992)—and therefore no census of the global population of (river) deltas. We used Google Earth to search the global coastline, recording the locations of each river mouth encountered, and then determining whether a delta existed at each. This search was conducted manually on imagery available through the public version of Google Earth.

We used the following criteria to identify river mouths:

1. width of ≥30m upstream of the limit of (observable) tidal influence as indicated by features such as rapid width change and tidal creeks, and
2. evidence of flow within the timescale of available imagery, generally within a timeframe of 1-10 years.

These criteria eliminate the effects of variable resolution of available imagery (a 30 m channel is visible even on the lowest resolution imagery available) and climate (requiring recent, rather than continuous, flow allows the inclusion of seasonal and intermittent rivers), while still excluding those features that no longer transport water and sediment to the coast. We deliberately excluded blind tidal channels from this analysis; those tidal channels which connected to a river channel were considered to be associated with that river. Rivers with multiple mouths were assigned a single identity, and the location marker was placed at the upstream-most distributary bifurcation. Tributary streams were not separately identified; distributary systems fed by more than one river (e.g. the mouths of the Ganges-Brahmaputra-Meghna system) were assigned a single moniker. In order to maintain objectivity when determining the presence or absence of a delta, each river was assigned a unique moniker when identified from the overhead imagery, rather than labeled with its local or English name. For a given stretch of coastline, the search was executed by selecting an arbitrary but readily identifiable point (e.g., the intersection of the coastline with a national border) and following the coastline, marking river mouth locations as needed.

Once river mouths along a section of coastline had been identified, we evaluated them for the presence or absence of a delta. Because many definitions of "delta" include sedimentological criteria impossible to determine from imagery alone, we developed a set of purely morphologic indicators to allow us to determine objectively whether a delta is present at a river mouth. These criteria are by design very broad: because we were restricted to satellite imagery and because the spectrum of morphological features needed to classify a landscape as being 'deltaic' is broad, our goal was to create as inclusive a definition as possible. In addition to the implicit requirement that a delta must be located at the outlet of at least one river, we determined that a delta was a coastal feature that fulfilled at least one of the following conditions:

1) a basinward projection of the shoreline,
2) a spatial (concurrently active) network of distributary channels, or,
3) evidence of a temporal (serially active) network of distributary channels.

A basinward projection of the shoreline is the classic lobe- or cusp-shaped extension of the land that is the result of spatially focused sediment accumulation at the coastline. Locations where the shoreline was basinward of the projection of the shoreline to either side (e.g., a river mouth within an embayment) were also considered deltaic (Fig. 11).

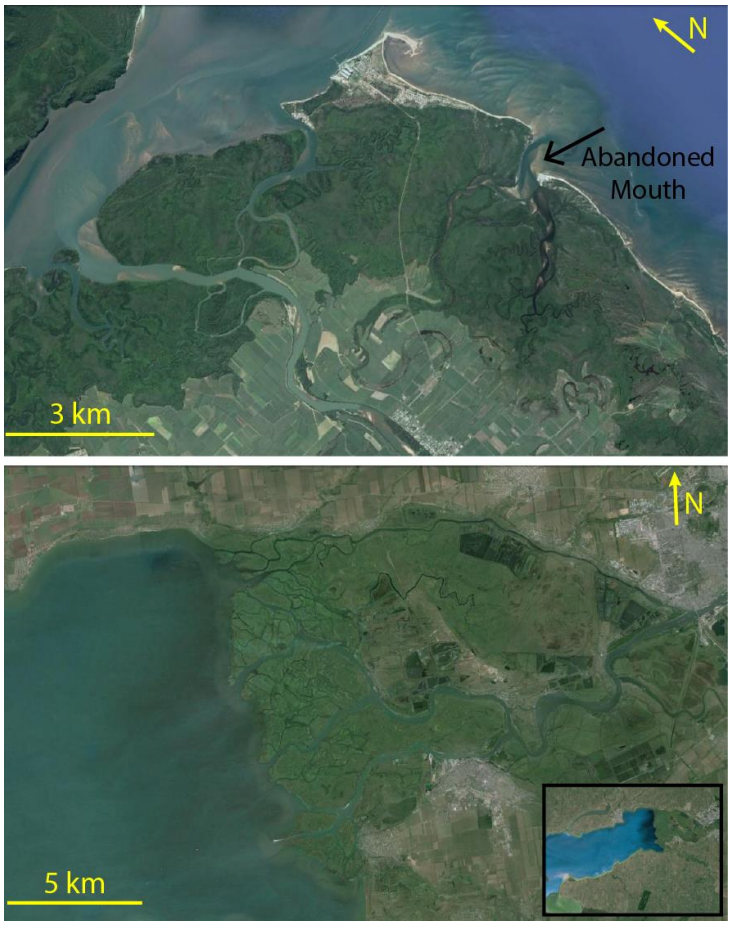

Figure 11: Example deltas. AU0088 (Herbert River, Australia, top) showing two active mouths and an abandoned outlet. BS0083 (Don River, Russia), showing spatial distributary network in an embayed environment (see inset map, lower right). Images from Google Earth.

A spatial network of distributary channels is one that consists of a set of two or more channels that *simultaneously* transport water and/or sediment to the coast (e.g., any river with more than one mouth); this is the archetypical "delta" with more channel bifurcations than confluences. A temporal network of distributary channels could take the form of a single, migrating, channel that sweeps across a section of coastline, a set of (abandoned) channels activated intermittently via avulsion, or some combination of the two; the channels need not be simultaneously active as long as they are active in a serial sense. The crux of these conditions is the lateral distribution of sediment across a section of coastline by fluvial, rather than marine, processes: either the river supplies multiple points along the shore with sediment simultaneously, or it distributes the sediment by moving its mouth(s). For the purposes of this study, any one

of the above criteria is a sufficient condition to determine that a delta is present at the mouth of a river.

Metrics:

The distribution of rivers with deltas along the global coastline is not arbitrary; rivers are products of regional and local precipitation patterns, topography, and geology (Syvitski and Milliman, 2007). The existence of a delta at the mouth of a river requires significant throughput of sediment, for basinward perturbations of the shoreline—one criteria for delta occurrence— can form only when the river supplies sediment faster than processes in the basin (e.g., waves and tides) can redistribute them. The ability of a process to move sediment can be related to the energy of the process. Energy based metrics, then, are physically significant ways to assess the geomorphic potential of a given process. In keeping with the use of readily available data to identify river mouths with deltas, we aim to define metrics that are as simple as possible and use inputs that can be obtained from readily available data. For example, though it is commonly done locally, collection of samples from the field for grain size analysis is too sporadic globally to allow us to use grain size for this survey.

Fluvial power:

A measure of the strength of the river—and thus its ability to transport sediment—is essential in order to compare deltas fed by rivers of different sizes. Such

metrics are often derived either from measures of the stress exerted on the riverbed by the water, or from the throughput of energy contained in the water itself.

If shear stress, τ, represents the frictional force exerted on the bed by flowing water, normalized by area, and flow velocity, u, is a distance per unit time, the product of the two can be cast as force exerted across a distance, per some unit area, per unit of time—in other words, energy dissipated by the bed per unit time, normalized by area—which has SI units of W/m^2. Under uniform, steady flow conditions, shear stress is commonly written as the depth-slope product:

$$\tau = \rho g h S \tag{1}$$

where ρ is the water density, g is gravitational acceleration, h is the depth of the flow, and S the water surface slope. The product of shear stress and velocity represents the energy provided by the river per unit time, normalized in both the downstream and cross-stream directions. In order to normalize by only the direction of sediment transport, we multiply the product by the width of the stream, B:

$$\tau u B = \rho g h S u B \tag{2}$$

Assuming a (relatively) rectangular cross section, Q, volumetric river discharge, may be substituted for the product of width, depth and flow velocity:

$$\Omega_f = \tau u B = \rho g Q S \tag{3}$$

which is a form of the stream power equation. This quantity represents the energy transferred from the stream to its bed per unit time per unit length in the direction of sediment transport.

Approaching the fluvial power metric from the standpoint of energy throughput, we can start with the standard equation for the kinetic energy of an object: $\frac{1}{2}mv^2$. If we treat a parcel of some unit volume as the object, its mass is simply its volume multiplied by its density; discharge Q is a relevant value with units of volume per time. Average along-channel flow velocity is a similarly simple choice for the velocity component. The result of substituting these into the kinetic energy equation is

$$P = \frac{1}{2}\rho Q u^2 \tag{4}$$

which has dimensions of power. Because the dimensions of other metrics are power per unit length, this must be normalized by some representative length scale. Normalizing by a measure of the width of the river—or that of its active distributaries or the channel belt, L_s—would produce a measure of average fluvial power over that portion of the shoreline intersected by the river:

$$\Omega_f = \frac{1}{2}\frac{\rho Q u^2}{L_s} \tag{5}$$

Both the stress-based and energy-based fluvial power metrics are physically reasonable methods for calculating the ability of the river to transport sediment. They measure energy in different ways: the stress-based measure (eq. 3) is aimed at the local rate of dissipation of energy to heat, while the energy flux (eq. 5) measures the discharge of kinetic energy through a vertical plane normal to flow. Although the two metrics require different data inputs, both have dimensions of power per length and the values are generally comparable (Fig. 12).

For our purposes here, water density and gravity are constant and represent a negligibly small potential variation in the value of the parameters described above. Both proposed metrics are linearly dependent upon discharge—a property that cannot be (directly) measured through publicly-available satellite imagery. The discharge of a river, however, is one of the most common measurements performed and is therefore a datum likely to be available for the greatest number of rivers. The discharge data used

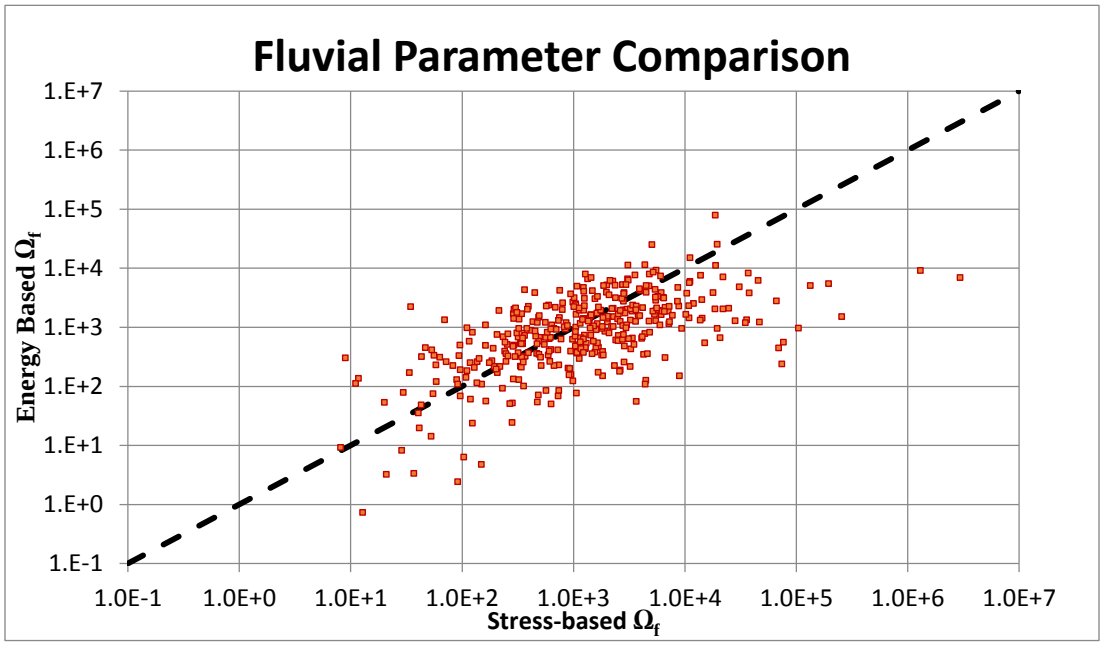

Figure 12: Comparison of the results of the two formulations for fluvial energy parameter: energy dissipation (stress-based) and energy throughput (energy-based) for the suite of rivers for which we have discharge data. Flow velocity was set at a constant 1.5 m/s for all rivers. Parity line shown dashed in black.

for this study was largely drawn from Milliman and Farnsworth's (2011) database as well as from internationally-supported river-gauging projects (e.g., GEMS-GLORI (Maybeck and Alain, 2012), and the GRDC). Additionally, fluvial discharge may be estimated from

empirical models of river scaling, and topographical and climatological data (Syvitski and Milliman, 2007).

The channel width length scale is easily measured from satellite imagery, but flow velocity cannot be extracted. Mean flow velocity has relatively low variability among rivers, however (Vörösmarty et al., 1989); flow velocity for most rivers in bankfull conditions is on the order of one to a few meters per second. (The common hydraulic-geometry relationship $V \propto Q^{0.1}$ presented by Leopold and Maddock (1953) indicates that velocity is not strongly related to discharge within a basin; we do not currently know if this applies also to deltaic distributary channels, but the geomorphic processes that drive channel adjustment such that velocity is almost invariant in the downstream direction likely also act to limit the variability of velocities in deltas.)

Coastal slope, by contrast, is far more variable among river systems: these span several orders of magnitude, from of the order of 10^{-5} (e.g., Ganges-Brahmaputra-Meghna, (Wilson and Goodbred, 2015)) to of the order of 10^{-2} (e.g., small fan deltas (Piper et al., 1990)). Coastal gradient can be measured on large scale from publicly-available DEMs, but in low-gradient systems the limited vertical resolution of the DEMs substantially overestimates the slopes near the coastline.

Although the results of both metrics are generally comparable, it is best to use the formulation which measures the quantity (energy dissipation or throughput) of greatest interest to a project. The near parity of the two measures means that approximation of one by calculation of the other is feasible, if no other options are available.

Wave Power:

Wind-driven gravity waves (e.g., swell) are a near-ubiquitous feature of nearshore environments and are a significant source of energy for the redistribution of sediment. The energy density (J/m^2) of a wave is

$$E = \frac{1}{8}\rho g H_w^2 \tag{6}$$

where H_w is the wave height. The product of the energy density with velocity of the wave yields a wave power parameter with the units of energy per unit time per unit length. For a near-breaking wave, the group velocity c_g is a function of the water depth:

$$c_g = \sqrt{gh} \tag{7}$$

where h is the water depth. Waves break when the water depth is three-quarters of the wave height (Battjes, 1974), so the wave power equation can be written:

$$P = \frac{1}{8}\rho g H_w^2 \sqrt{\frac{3}{4} g H_w} \tag{8}$$

or

$$P = \frac{\sqrt{3}}{16}\rho g^{\frac{3}{2}} H_w^{\frac{5}{2}} \tag{9}$$

As above, density of the water (either seawater or lake water) varies only slightly across the globe, as does the value of gravitational acceleration; ρ and g can therefore be considered constants. We used daily satellite measurements of global significant wave

height data to create a mean annual wave height map (Fig. 13) at a resolution of 1° (available from AVISO); meteorological records would contain more local data but are not included in this analysis.

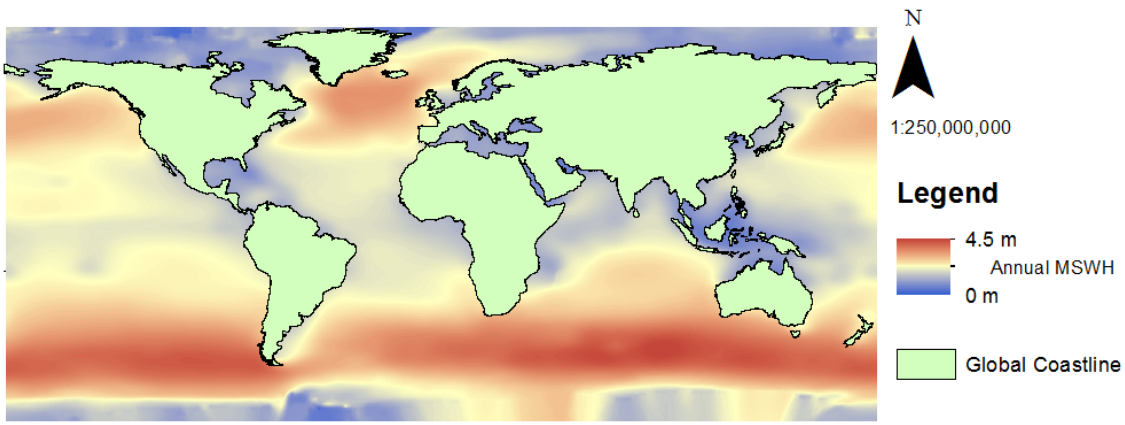

Figure 13: Global annual average of mean significant wave height, as measured by satellite. Note that wave heights are highest in the open ocean.

Tidal Power:

Although tides, like the river that feeds the delta, mainly transport sediment and water perpendicular to the coastline, the use of a 'tide power' equation derived from shear stress produced by tidal currents is not feasible. The velocity and duration of tidal currents are highly variable across the length of a single tidal channel; many tidally influenced deltas have extensive networks of channels. A metric similar to the stream power described above would need to determine a single representative point in space and time in order to calculate discharge.

Tides are, like their smaller wind-driven cousins, waves, and previous workers (*e.g.*, Harris, *et al.*, 2002) have used a version of the equation for wave energy derived above to describe their strength. However, that equation is predicated on the existence of

an infinite field of regular waves: the tidal wave is global in scale and we therefore believe it is not well represented by that model.

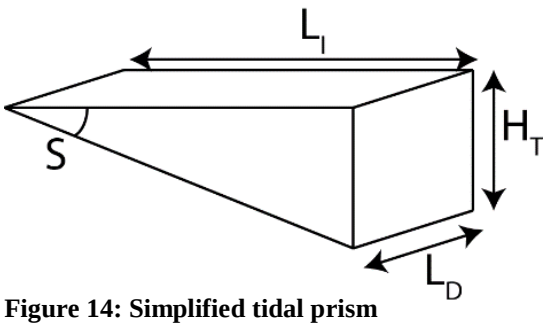

Figure 14: Simplified tidal prism

Instead, we represent the energy of the tidal wave as the potential energy needed to lift the water within the tidal prism (Fig. 14) from low to high tide. In cross section, the tidal prism can be represented by a triangle of height H_T, the height of the tide and a base the length of the intertidal zone, L_I. This length can be written as a function of the tide height and the near-shore slope S:

$$L_I = \frac{H_T}{S} \tag{10}$$

The cross-sectional area A_T of the tidal prism is therefore

$$A_T = \frac{1}{2}\frac{H_T^2}{S} \tag{11}$$

Multiplying the area of the tidal prism by the width of the delta, L_D, yields the volume of water moved onto the delta topset between low and high tide. This volume multiplied by gravitational acceleration and the density of the water is the total weight of the water. The potential energy is the total weight multiplied by the distance (the tide height) over which it has moved:

$$E_T = \frac{1}{2}\rho g \frac{H_T^2}{S} L_D H_T = \frac{1}{2}\rho g \frac{H_T^3}{S} L_D \tag{12}$$

In order to match the dimensions (energy per unit time per unit length of transport) of the previous metrics, we must divide the energy by the length of time needed to lift the water

from low to high tide, half the tidal period, *T*. We also must normalize the energy by a length scale: here, we use the width of the delta:

$$P_T = \frac{\frac{1}{2}\rho g \frac{H_T^3}{S} L_D}{\frac{1}{2} T L_D} = \frac{\rho g H_T^3}{ST} \quad (13)$$

Tidal period is a function of the ratio of the semidiurnal and diurnal components of the tides. The tidal form ratio (Steacy, 2006, Harris *et al*., 2002) is a quantitative metric of the type of tide (e.g., diurnal, mixed or semidiurnal), but does not yield the smooth variation in tidal period that exists in the field. Instead we treated the main semidiurnal and diurnal components of the tide as two interacting sine waves of periods π and 2π and varying phase shifts and amplitude ratios in order to create a simplified representation of water surface elevation through time. For each combination, we then found the shortest time between extrema (Fig 15).

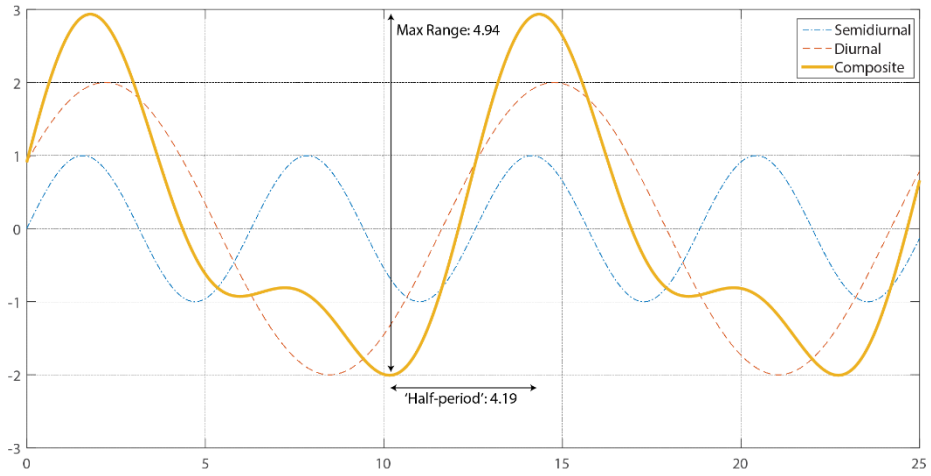

Figure 15: Interacting sine waves of periods π ('semidiurnal', dot-dashed blue line) and 2π ('diurnal', dashed red line), and their sum ('composite', solid gold line). The amplitude ratio of the diurnal to semidiurnal tide was 2, and the phase lag 0.15π

We averaged the results across all phase shifts to generate an empirical equation for tidal "half-period" as a function of the relative amplitudes of the original sine waves (Fig. 16).

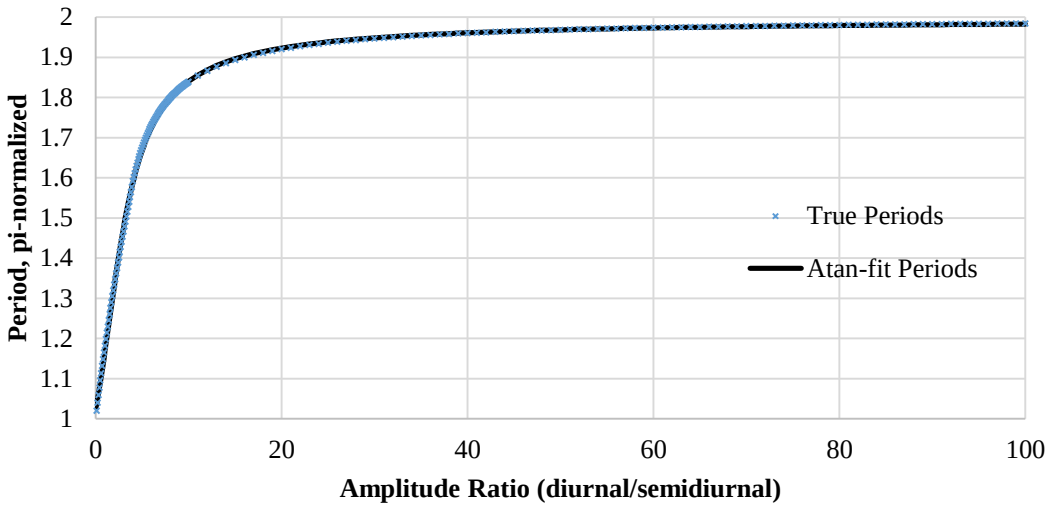

Figure 16: 'Half-periods' generated using interfering sine waves and ratio of diurnal to semidiurnal amplitudes.

Global tide heights are measured by buoys and satellites and have been numerically modeled. Buoy data is accurate but highly localized and lacks the global high-density distribution of data points needed to analyze this data set. The Tidal Model Driver (TMD) developed by Oregon State University has high (15 arc minute) resolution data for the global tide. This data is derived from a barotropic inverse solution from individual tidal constituents; we extracted a global map of tidal amplitude for the M2 (lunar semidiurnal) and O1 (lunar diurnal) harmonics. As with the half period, we averaged the calculated range of each composite sine wave over all phase shifts and fit a curve that related amplitude ratio to total range (Fig. 7). We used least-squares methods

to fit a second order polynomial to the data because the residuals from a first-order (linear) fit showed structure: the residuals from the second-order fit showed no structure.

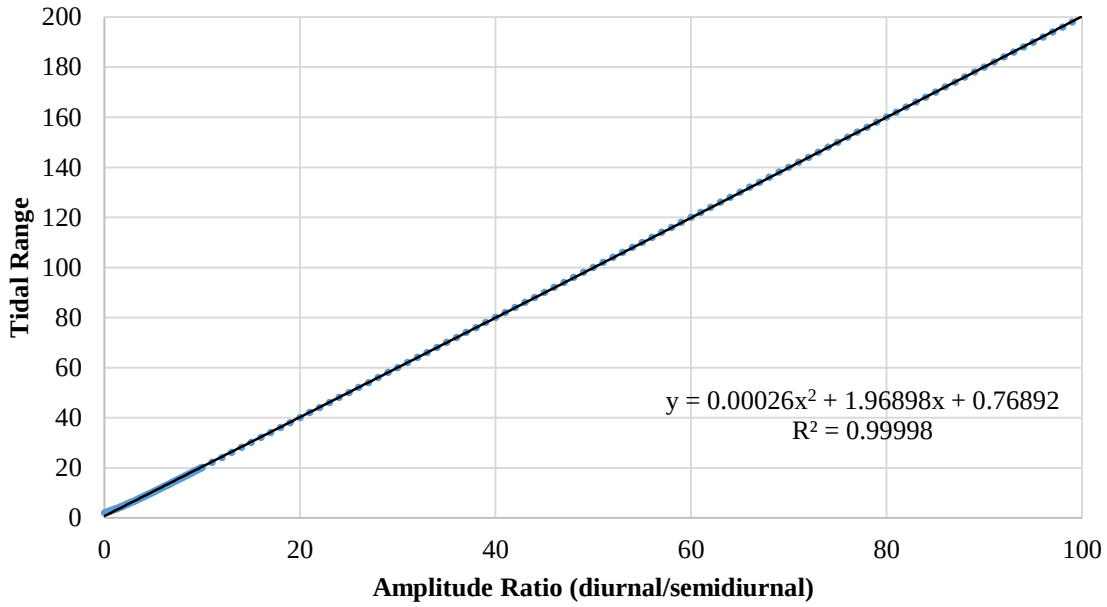

Figure 17: Maximum range as a function of ratio of amplitude of diurnal and semidiurnal tidal constituent.

Because this equation is nearly linear, we multiplied the range predicted by this equation by the amplitude of the semidiurnal component to estimate real tidal range. We used only the lunar constituents of the tide—rather than a combination of lunar and solar—because over the course of a lunar month the net contribution of the solar components to the total range is near zero. Local bathymetry strongly affects tide height: we combined available buoy data with the gridded tidal range data derived from the TMD and performed an inverse distance weighted interpolation (order = 2) to create a global tidal range map (Fig. 18) that balances the need for global coverage with the most

detailed local data available. This map of tidal range slightly (~10%) underpredicts the tide in most coastal areas.

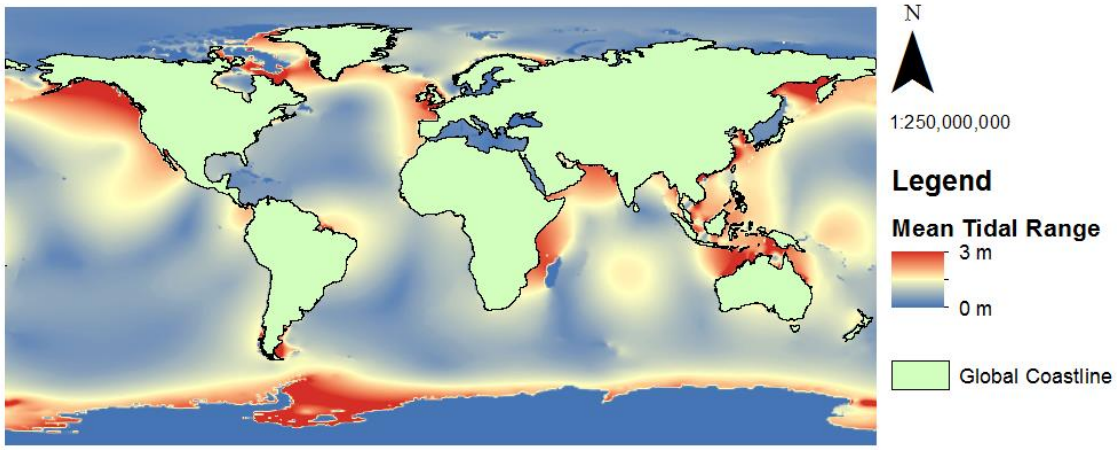

Figure 18: Global map of mean tidal range. Note that the range is highest in coastal areas.

Shoreline Generation:

In order to analyze the shoreline geometry, we created a land-water binarized map of each delta. Water and land have different spectral reflectivities; we selected Landsat bands which maximized these differences in order to discriminate between the two. A pixelwise division of the red band (Landsats 4-7 band 3 (0.63-0.69 microns) or Landsat 8 band 4 (0.64-0.67 microns)), which reflected strongly from water but weakly from land, and a shortwave infrared band (Landsat 4-7 band 5 (1.55-1.75 microns) or Landsat 8 band 6 (1.57 - 1.65 microns)), which reflected weakly from water and strongly from land, further increased the contrast. We scaled the quotient and binarized the image at a threshold pixel value selected on an image-to-image basis. (Fig. 19) We then cropped the full image tile to the area surrounding the delta.

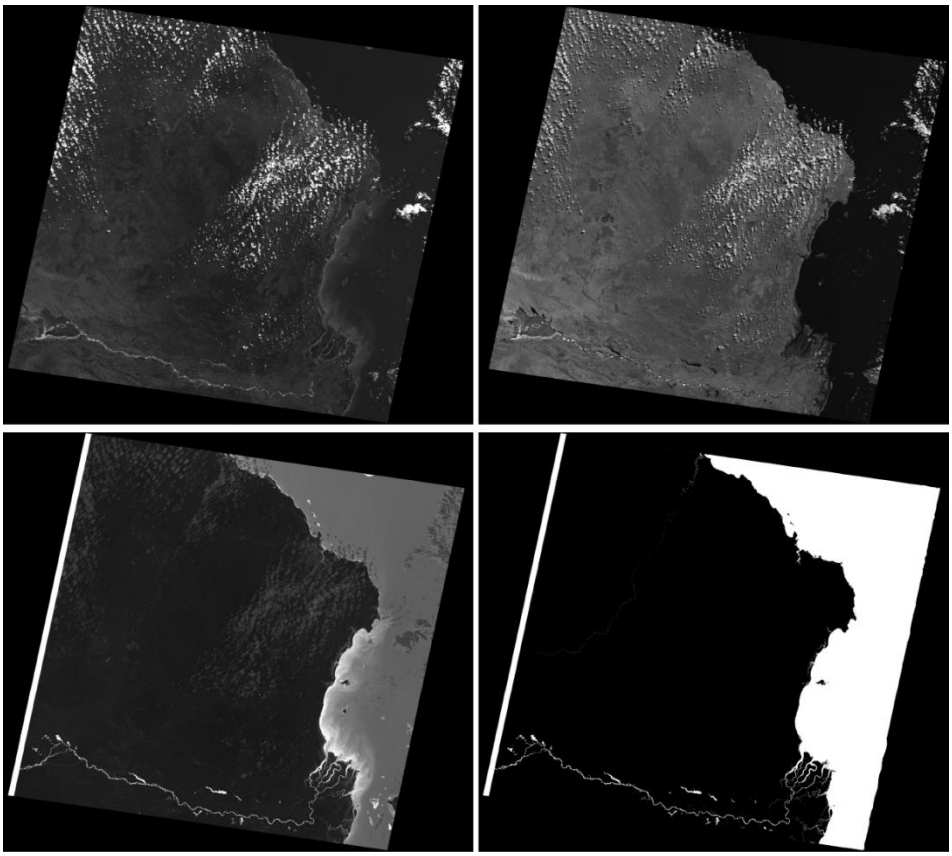

Figure 19: Landsat images of the Rufiji river delta, Tanzania. Band 3 (top left) and Band 5 (top right) maximize the difference in spectral reflectivities of land and water. The scaled quotient of Bands 3 and 5 is shown bottom left; the final thresholded land-water map is shown bottom right.

The shoreline was automatically generated using the "opening angle" method described by Shaw *et al*. (2008). This method queries each 'water' pixel on the map to determine the total arc through which the open water can be viewed. We select a contour (45°) from the resulting map to define the shoreline. (Fig. 20) This method allows the creation of a continuous shoreline across channel mouths and other deep embayments, and around islands; simple edge finding would result in multiple disconnected shoreline fragments, with channel banks reaching farther inland than could

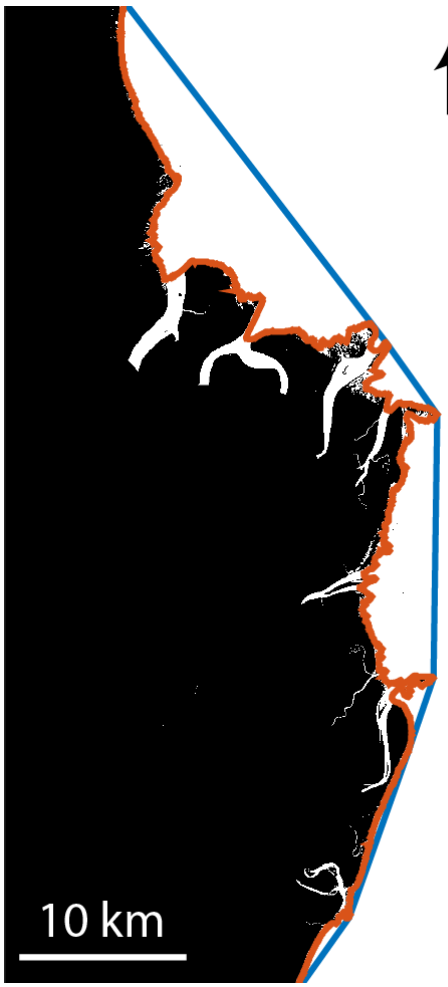

Figure 20: Land-water map of the Rufiji delta, Tanzania. In orange, the OAM-defined shoreline. In blue, the convex hull. Channels and water features in delta interior have been masked out to reduce OAM computational time.

reasonably be considered part of the coastal system. Linear extension of the shoreline across channels and embayments introduces subjectivity (e.g., where does the channel begin?) and could result in the neglect of segments of the land/water interface that could reasonably be expected to receive wave and tidal energy.

Shaw's method is reasonable in the physical sense: field-of-view may be considered a rough measure of exposure to sources of basin energy. This method also allows uniform and objective treatment of islands and spits: if the landform is large enough to completely shelter other portions of the land/water interface from the basin, the basinward edge of the landform must be considered the coastline.

Shoreline Processing:

Here we examine measures of delta shoreline geometry from our global database. We consider the shoreline vector (i.e. a sequence of horizontal *x, y* pairs) produced using the Shaw et al. method to be an accurate representation of the coastline. However, any noise in the original land-water boundary is therefore also found in the shoreline vector.

Shoreline direction and curvature are the first and second derivatives of the shoreline vector with respect to arc length. Since differentiation amplifies noise, smoothing is necessary. We used a Savitzky-Golay filter to do this because the filter preserves the amplitude of (significant) peaks—in contrast to other smoothing methods (e.g., running averages and smoothing splines) which reduce the amplitude of large-scale excursions as well as removing noise (Schaefer, 2011).

Deltas are usually characterized by a large-scale basinward protrusion of the coastline. This excursion represents a systematic change in direction along the length of the shoreline; since our focus here is on the statistics of local shoreline direction, we detrended the shoreline direction vector before further processing.

The shoreline is the interface between the delta and the basin; therefore sediment transport due to basinal processes should affect the shape of the shoreline. Rugosity (shoreline sinuosity) was calculated as a ratio of the shoreline length to the length of the convex hull enclosing that portion of the coast; the use of a convex hull, rather than simple start-to-end linear distance reduces the effects of the overall shape of the shoreline on the measurement. Smoother coastlines have rugosities close to unity. We also computed fractal dimension for each shoreline by a simple box counting method: the shoreline length was measured using a set of rulers with increasing lengths and the resultant shoreline lengths plotted as a function of the ruler size (Feder, 1988).

Shoreline complexity may also be described in terms of the piercing features: the number and spacing of inlets, or the dissection of the shoreline by channels, are other measures of the shape of a delta's shoreline. Because an inlet requires a landward

projection of the shoreline, it must be associated with a (relatively) rapid change in direction—an area of high curvature. To find the average spacing of these shoreline-piercing inlets, we therefore searched the smoothed, detrended vector of shoreline azimuths for runs of low (cumulative) curvature. Because the shorelines generated by Shaw's method are continuous across channels and embayments, we can also use an overlay of the shoreline onto the binary wet-dry map to determine which of the shoreline points are 'wet' (*i.e.* the picked shoreline is crossing an inlet). We can then find continuously wet (or dry) runs of shoreline points. Since many of these runs are a few to a few tens of pixels long, they are often not accurate representatives of the shoreline at the channel scale. We therefore define a 'significant run length'—the mean length of the longest 33% of runs—to compute meaningful data on run length and shoreline azimuth. Furthermore, the length of these runs is dependent on the size of the delta: Landsat imagery has a fixed resolution of 30 m/pixel for the bands we used to generate the shorelines. Therefore, we must divide the length of the mean significant run by some length scale that captures the size of the delta; here, we used the total shoreline length.

Results:

Rivers are far more common than deltas. Over the coastline surveyed, only ~25% of river mouths were associated with deltas. Because delta occurrence is limited by river occurrence under our definition of deltas, we define a delta occurrence frequency: the total number of deltas on a section of coastline divided by the total number of rivers

along the same section. By normalizing by river occurrence, we can eliminate those factors (*e.g.*, precipitation) which control the placement of both rivers and deltas.

The presence or absence of a delta at a river mouth is controlled by net sediment flux, accommodation, and time. Because of the dependence of the tidal energy parameter on slope and the lack of an accurate, global dataset of near-coastal slopes, it was not possible to directly associate tidal strength with delta occurrence. In order to determine whether the tidal and wave energy regime affected delta occurrence, we compared the average values of the cube of the tide height ($H_T^3 \propto \Omega_T$) and the 2.5 power of the wave height ($H_W^{2.5} \propto \Omega_w$), for all river mouths with and without deltas. We found no significant difference (Students' T test, a=0.05) between the average value of H_T^3 at river mouths with and without deltas, but we found that the average values of $H_W^{2.5}$ did differ significantly, with higher wave energy values associated with absence of a delta.

Continental shelf width provides a crude measure of the offshore slope, and thus of static accommodation, i.e. the space available for the delta to fill without accounting for relative sea-level rise. We measured the distance between the 0 m and -150 m contour lines at ~100km intervals along the global coastline and averaged these distances for subsections (e.g., Pacific coast of South America) of the continental coastline. We found a very weak correlation between these values and the delta occurrence frequency for each section of coast (Fig. 21).

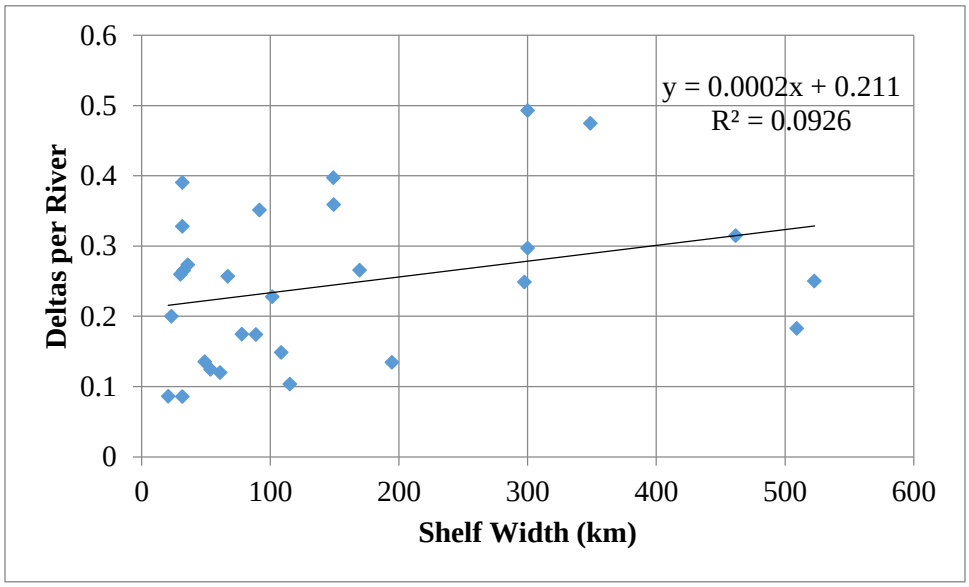

Figure 21: Delta occurrence frequency has a very weak correlation with continental shelf width.

We found no correlation between shoreline rugosity and wave or tide energy (R^2 values <0.05) across all deltas for which we had discharge data (Fig. 22). When that set was reduced to only the largest deltas we found a weak (R^2=0.27) correlation between absolute wave energy and rugosity, but no similar increase in correlation with tidal energy (Fig. 23).

We analyzed the shoreline for runs of low cumulative change in direction as well as for runs of continuously 'dry' pixels. We designated the mean of the longest third of these runs as the mean significant run length (MSRL), and normalized this length by the total shoreline length. This number represents the average proportion of the shoreline found between inlets: higher numbers should represent coastlines with fewer inlets.

We found only a weak correlation between the normalized MSRL of dry pixels and wave energy, and no significant correlation between it and the incident tidal energy

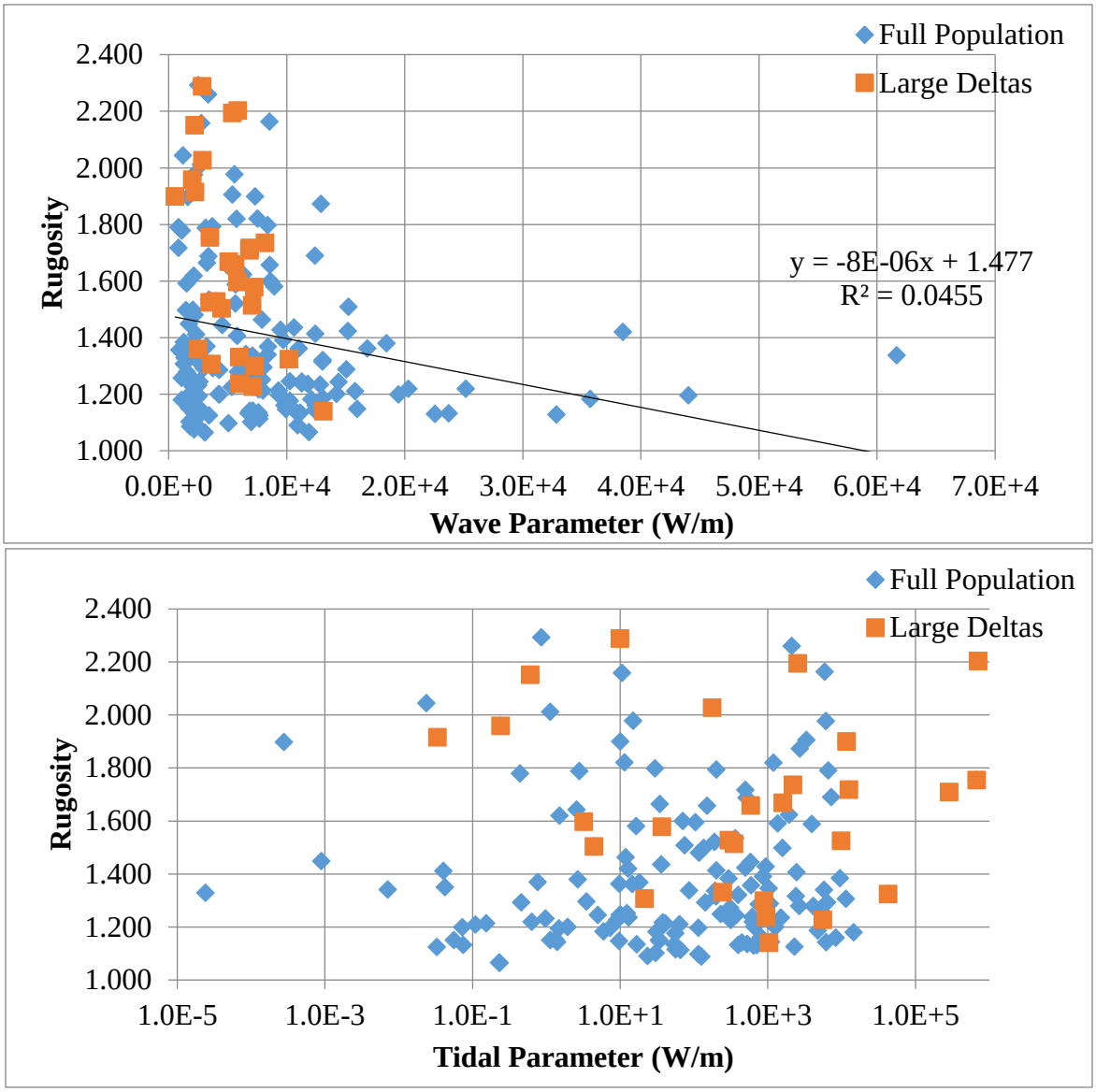

Figure 22: Rugosity of full population (blue diamonds) and large delta subset (red squares) plotted against wave (top) and tidal (bottom) energy. Note the logarithmic scale (and 10 order of magnitude range) on the tidal parameter plot. Note also the distribution of the large delta subset within the full population: large deltas occupy the full range of rugosity values and wave and tidal parameter values.

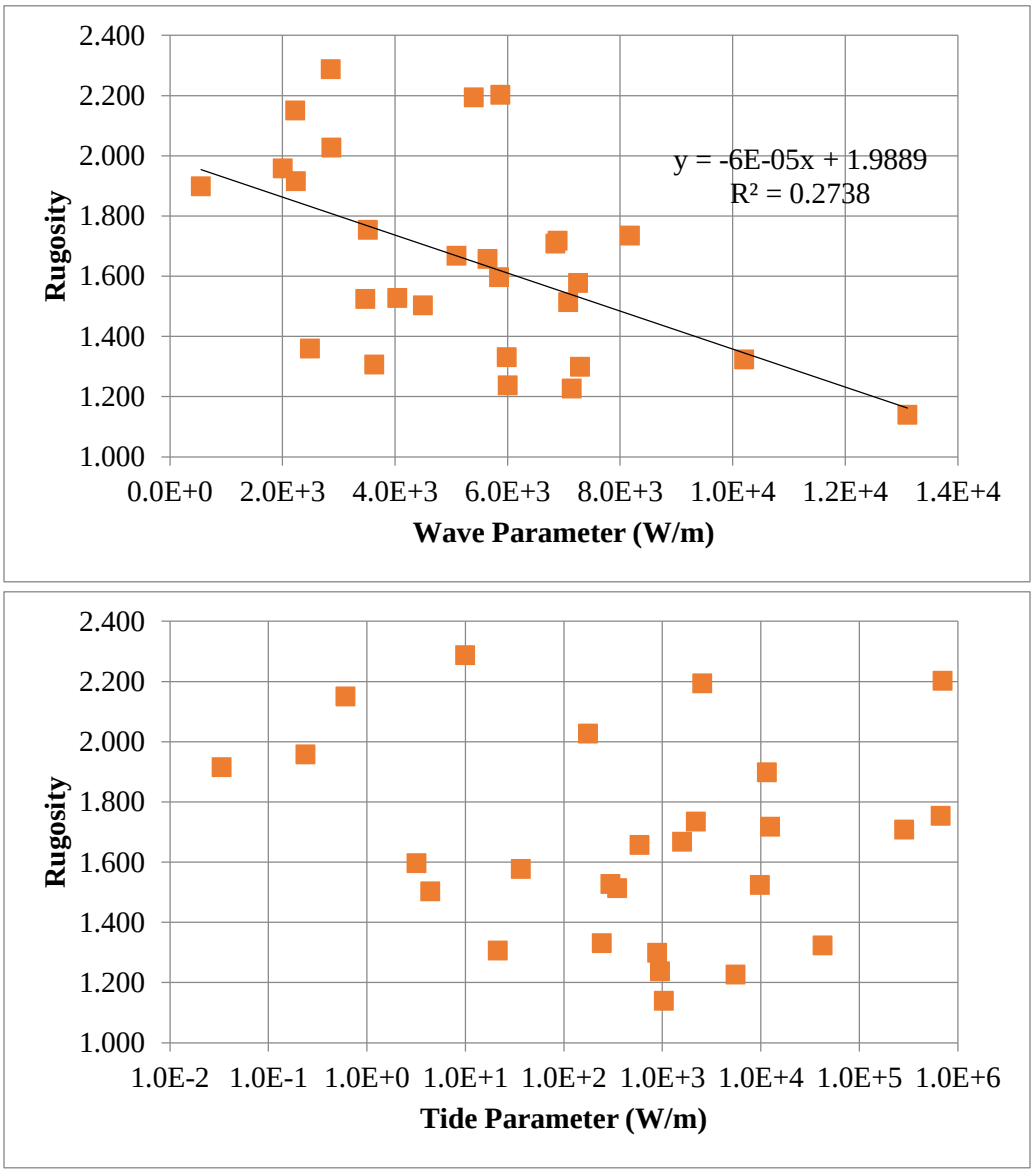

Figure 23: Wave (top) and tidal (bottom) energy as compared to shoreline rugosity for a subset of large deltas. Note the logarithmic scale for the tidal parameter.

(Fig. 24). Neither wave nor tide energy was correlated with the MSRL of runs of low cumulative change in direction (Fig. 25).

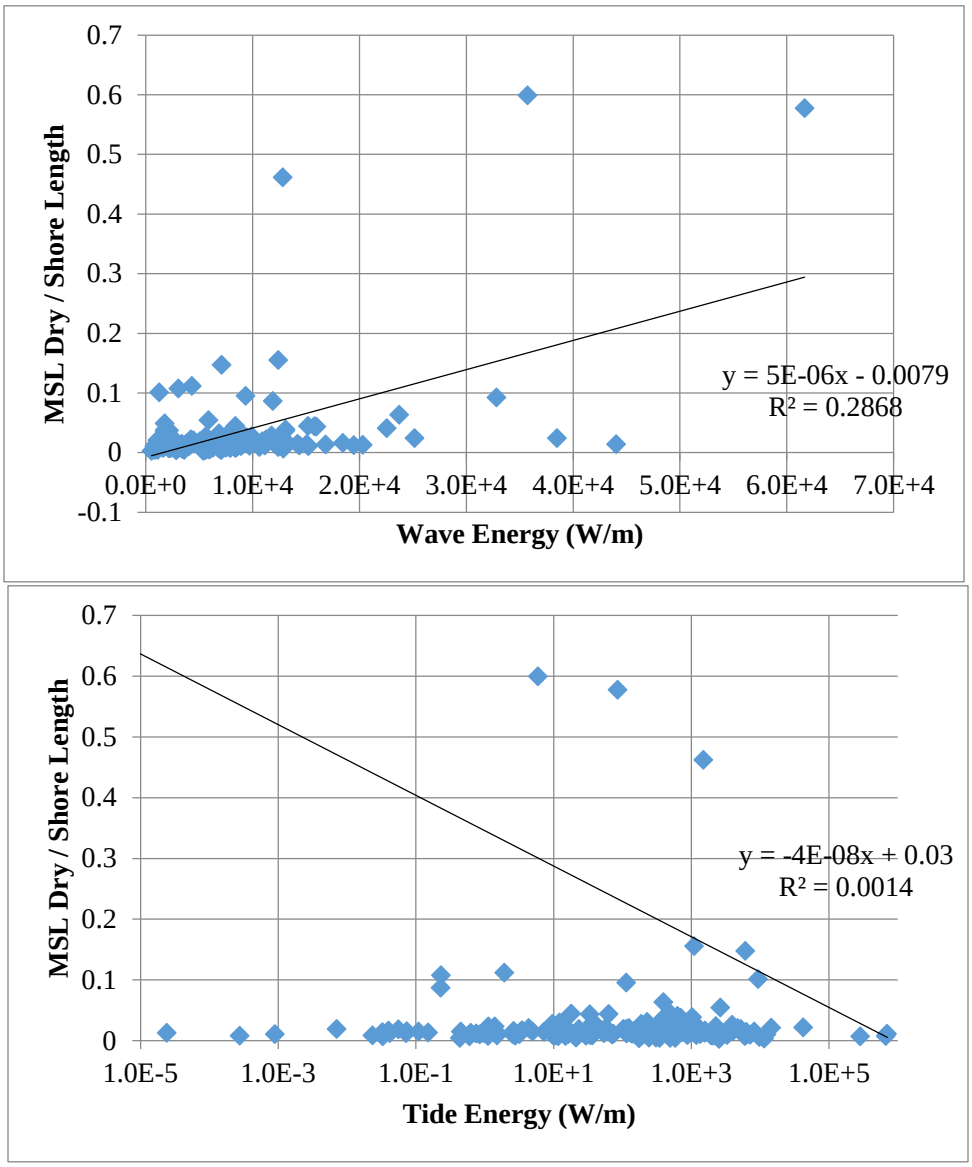

Figure 24: Normalized mean significant length of runs of dry pixels compared to wave (top) and tidal (bottom) energy parameters.

We also analyzed the overall variation in shoreline azimuth, as measured by the standard deviation of the detrended direction vector. Azimuth is not dependent on the size of the original image because it is a spatial derivative; therefore there was no need to normalize these values. We also analyzed the skewness of the curvature vector: high

skews are associated with periods of low curvature punctuated by small areas of rapid change in azimuth, which on a shoreline could indicate the mouth of a channel or inlet. We found no correlation between either shoreline azimuth variability or curvature skewness with either wave or tidal data (Figs. 26 and 27).

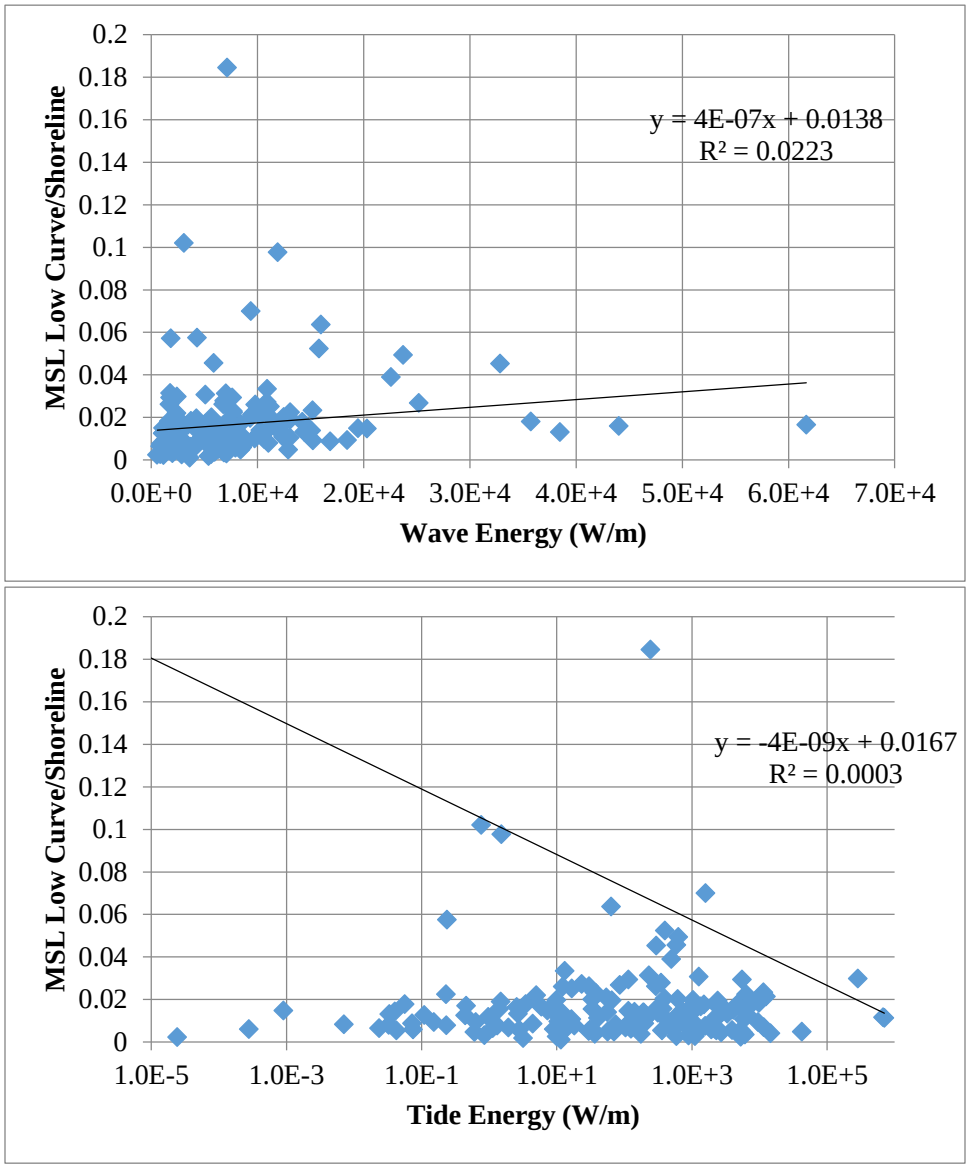

Figure 25: Normalized mean significant length of runs of low cumulative change in direction compared to wave (top) and tidal (bottom) energy parameters.

Figure 26: The standard deviation of shoreline azimuth has no correlation with either wave (top) or tidal (bottom) energy parameter.

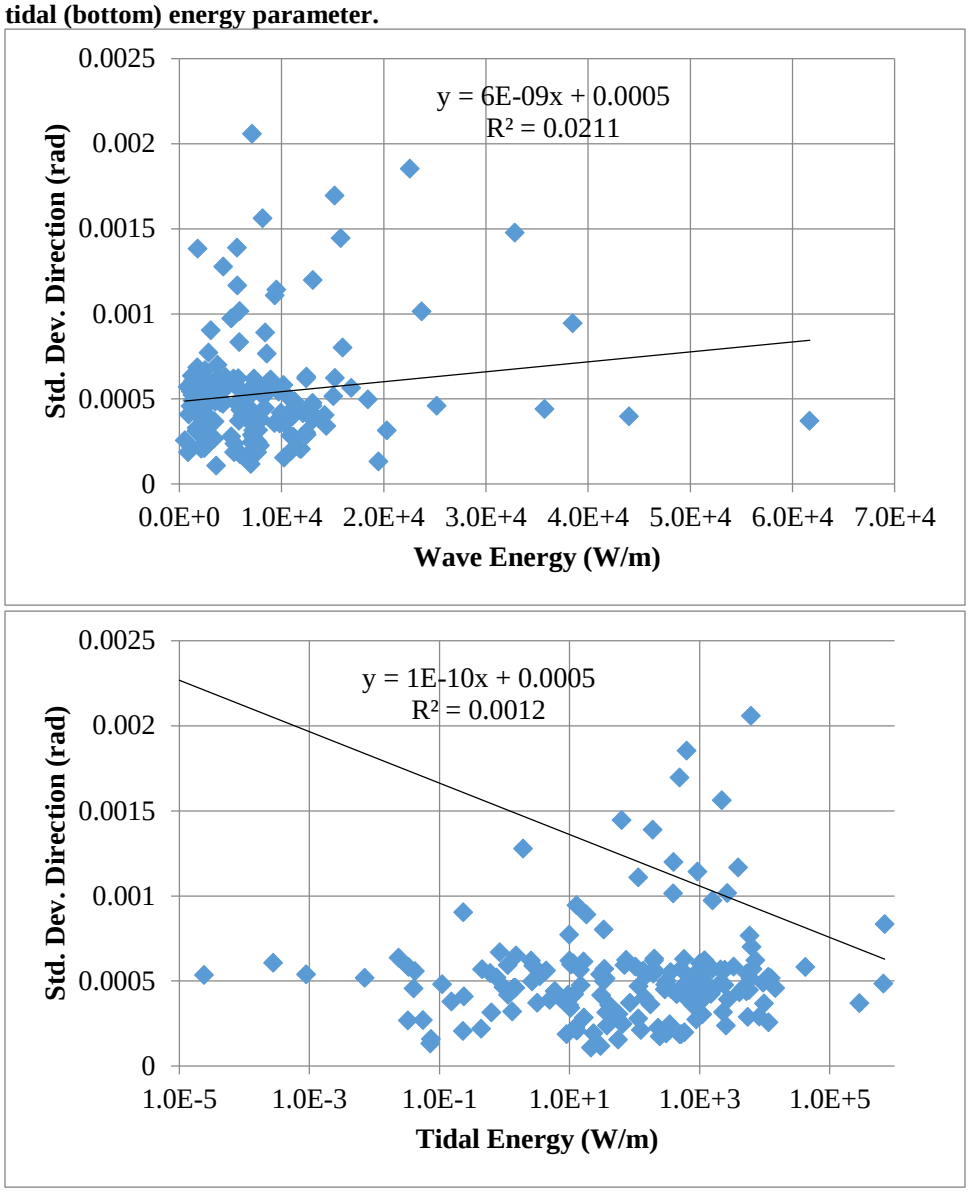

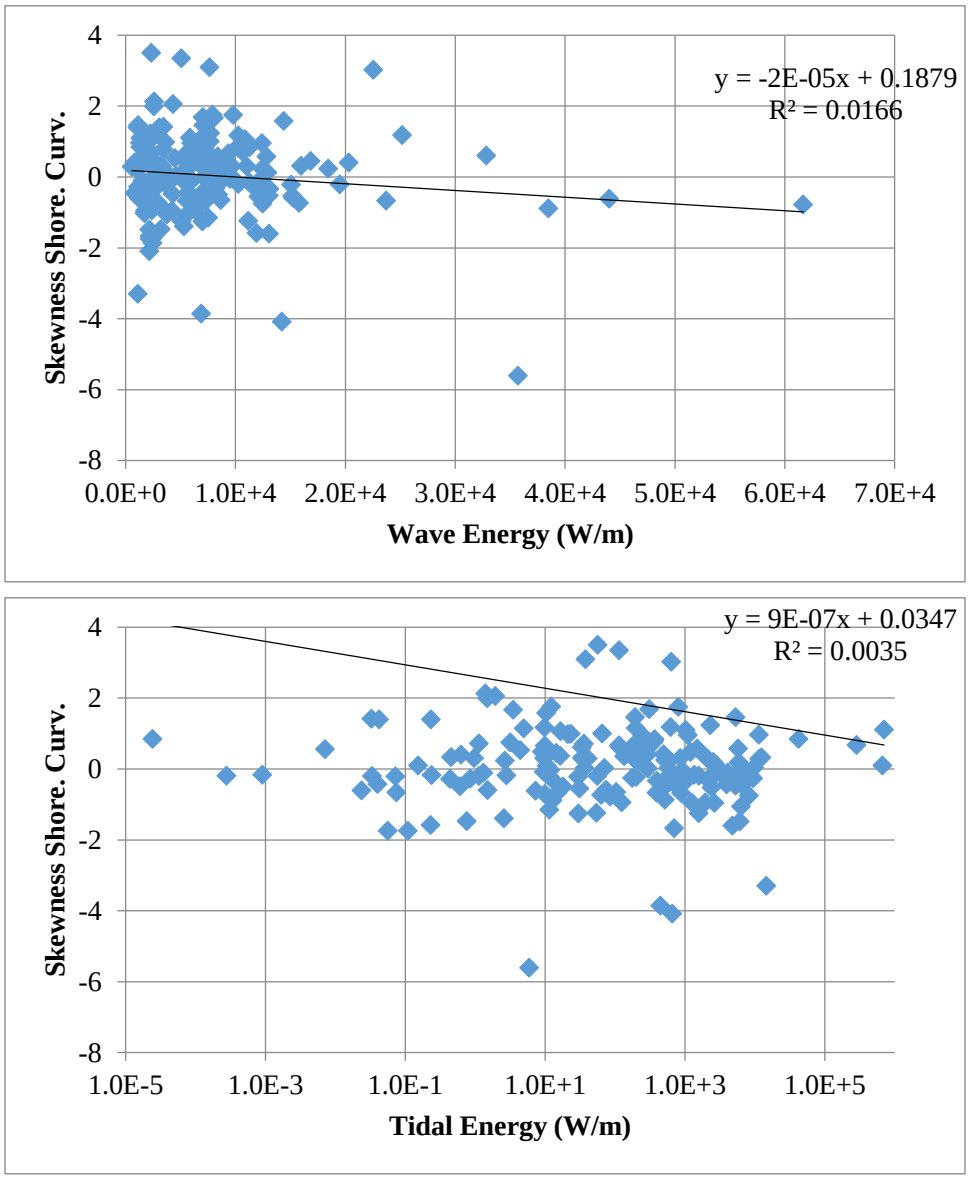

Figure 27: Skewness of shoreline curvature is not correlated with wave energy (top) or tidal energy (bottom).

Discussion:

We found that there was a statistically significant difference in the average wave energy at river mouths without deltas versus those associated with them, but that there was no such difference in the average tidal energy. Thus there is an indication, albeit

weak, that wave action is one factor that suppresses delta formation on coasts. We also found that there was no measureable link between offshore slope (as measured by continental shelf width) and delta occurrence frequency. We could not account for local base level change rates, uplift, or subsidence, but together these data suggest that of net sediment flux and static accommodation, the former exerts the stronger control over delta occurrence, and that of potential contributors to sediment flux away from a river mouth, the waves are the more effective. Neinhuis *et al.* (2013) suggest that wave reworking of inactive or abandoned delta lobes can remove enough sediment to completely obscure the geomorphic signal of a delta. Our results are in accordance with this, in that the greater the wave height—and the more energy available for sediment transport —the faster this process will be and the more likely the river mouth to be considered nondeltaic. In that sense, one might say that the limit of wave influence in deltas is no delta at all, an idea consistent with the work of Neinhuis *et al.* (2013).

In general, wave action tends to create smooth, straight shorelines, as long as the angle of incidence is relatively low (Ashton and Murray 2006). In this study, the correlation between shoreline rugosity and wave energy is weaker than that seen in experiments (Chapter 2) and weaker than this conventional reasoning would suggest. While the rugosity metric effectively differentiated qualitatively smooth and rough shorelines, the differences were not associated with concomitant variation in wave or tidal energy. Neinhuis *et al*. (2013) and Ashton and Murray (2006) also suggest that shoreline smoothing is only one of several potential effects of waves; in cases of oblique incidence, shoreline rugosity may increase. However, large scale features such as they

describe are likely to be accounted for by the combination of the OAM and the convex hull: the shoreline will not extend far into an embayment behind a flying cape, and the hull will follow the basinward edge of the feature.

This lack of correlation may be due, in part, to the presence of confounding factors (e.g., sediment size, vegetation and human modification, see Orton and Reading, 1991 and Edmonds and Slingerland 2010 for discussion of the former) in the field that were held constant in the laboratory-grown deltas. Another possible explanation is that we used the mean annual significant wave height to calculate energy. It may be that shoreline rugosity is set by large, relatively infrequent events (e.g., storms)—an analog to the fluvial 1-2 year flood – and that the wave energy associated with these events is not well correlated with the annual mean value. Further investigation into the correlation between storm-wave heights and mean annual wave heights globally would help determine whether this is the case.

The emergence of greater correlation between shoreline rugosity and wave energy with the restriction of the dataset to the largest deltas cannot be attributed to the greater river flux within those deltas: rugosity is uncorrelated with wave power when normalized by fluvial power (Fig. 24), nor can it be attributed to a greater range in rugosity values- the subset spans the range of both parameter values and rugosities (Fig. 22).

Conclusions:

Based on what we believe to be the first global compilation of coastal rivers and their associated deltas, we find that while the energy supplied by the basin to a river mouth is at least partially responsible for determining whether or not a delta forms, it has little quantitatively measurable effect on the morphology of the resulting delta. Specifically:

1) Delta occurrence is weakly associated with lower average wave energy values. We believe this is due to the removal/transport by waves of sediment away from the river mouth.
2) Shoreline rugosity is not closely correlated with average incident wave and tide energy. A weak correlation with wave energy appears if attention is restricted to relatively large deltas. The unexpectedly poor correlation overall between shoreline smoothing and wave energy may be due to unaccounted-for differences in sediment properties or may signal the influence of intermittent large events.
3) The spacing and azimuths of shoreline piercing features are similarly poorly correlated with the basin energy regime

Chapter 4:

Title: Morphology and dynamics of experimental deltas formed under mixed wave and tide conditions

Authors: Baumgardner, S., Renou, J., and Paola, C.

Abstract:

Deltas in the field display a wide range of planform morphologies and dynamics. Studies of deltas in the field are hampered by the presence of confounding factors that limit comparability across location, and there has been limited computational modeling which incorporates more than one source of energy to a delta other than the river. The Delta Basin facility at St. Anthony Falls Laboratory has combined a previously successful system for tide simulation with a wave generator to study the effects of mixed wave-and-tide energies on fluvial deltas. The deltas produced developed morphologies consistent with field-scale deltas known to have developed in mixed energy systems.

Introduction:

The economic, environmental and agricultural importance of deltas is well-established (Syvitski *et al*., 2009, Han *et al*., 1995). Of particular interest is the morphologic response to allogenic forcing; specifically, response to changes in base level and other consequences of a changing global climate and increased water usage. Inasmuch as planform morphology is represented in the stratigraphic record, a better understanding of the link between morphology, fluvial transport and energy impinging on a delta from the basin will benefit interpretation of depositional environments and

improve prediction of subsurface structures. Diagnosis of fluvial, tidal and wave influence in ancient deposits is made from the facies context as well as from the presence of individual features (e.g., sand ridges) within the study area (Willis, *et al*., 1999, Legler *et al*., 2013). Modern deltas rarely exhibit geomorphic features formed by a single one of these influences. The imperfect nature of the rock record—and its limited accessibility—mean that interpretations of fluvial-, tidal- or wave-influence must be made from a small amount of data. Quantitative study of deltas with known energy influences may help narrow potential interpretations of the suite of features preserved in the field. In addition to studies of exposed rocks, data from high-resolution seismic surveys can be processed to yield surfaces of constant time—creating planform snapshots of depositional systems (Hubbard, *et al*., 2011).

To understand the net effect of allogenic forcing in the field, it is useful to study them in a controlled environment, free of confounding factors such as past history, differing sediment size, vegetation, and anthropogenic effects. While computational and physical methods have been used to study purely fluvial delta formation (Edmonds and Slingerland, 2010, Paola *et al*., 2009, Reitz and Jerolmack, 2012), initiation and evolution of tidal inlets and channels (Marciano *et al*., 2005, Geleynse *et al*., 2011, Kleinhans *et al*., 2012), and wave transport of sediment in the coastal zone (Ashton *et al*., 2013, Kamphuis, 1991) no modeling study has yet combined the three processes. Physical experiments on delta dynamics under wave and tidal influence have only recently begun (see references in Ch. 2 of this thesis, particularly the work of Kleinhans *et al*., 2012),

and have been limited to the study of the wave and tide effects independently, without allowing them to interact.

Building on the success of a previous series of experiments in which tidal forces impinged on an evolving fluvial delta (this thesis, Ch. 2), we have performed a series of experiments in which we subjected a delta to varying fluxes of tidal and wave energy in combination. As in the previous experimental series, the tidal forces are produced by a systematic pseudosinusoidal variation in base level over a timescale chosen to reproduce, to first order, the effects of the propagation of a tidal wave into the shoreline of a delta. The wave energy was produced by a simple oscillating paddle.

Wave, Tide, and River Strength:

Before describing the experiments, it will be useful to define a set of parameters to measure the relative strengths of the three input parameters we are investigating: waves, tides, and rivers. We do this in terms of the energy that each process applies to the delta. Although experimental deltas provide a wealth of data that would allow detailed measurement of energy fluxes, we prefer to use parameters that could be applied to field deltas as well. We therefore prioritized simplicity and "data frugality" (use of data that is widely available) for parameter definition. Because these parameters are intended for cross comparison, the units of each parameter are identical: W/m.

The fluvial strength parameter Ω_f starts with the product of shear stress τ and velocity u (unit stream power), which represents an energy per area per time. To arrive at

energy per unit of distance in the mean transport direction, we then multiply by the channel width *B*:

$$\Omega_f = \tau u B \tag{14}$$

If shear stress is calculated under the assumption of uniform, steady flow, the parameter can be written

$$\Omega_f = (\rho g h S) u B = \rho g S (B h u) = \rho g S Q \tag{15}$$

where ρ is the water density, g is the gravitational acceleration, h the water depth and S the water surface slope. The product Bhu represents the discharge of the river Q. This parameter is a form of the stream power equation and has units of W/m. In our experiments, discharge was held constant (see additional discussion below), causing the value of the parameter to depend entirely on the topset, channel-wise slope of the deposit.

Another version of the fluvial parameter uses the kinetic energy of the water within the channels:

$$\Omega_{f,a} = \frac{1}{2} \frac{\rho Q u^2}{L_s} \tag{16}$$

where u is mean flow velocity and L_s is the width of the channel. This represents the total flux of kinetic energy, rather than the local dissipation rate. We elected to use the shear stress-based method because reliable delta slope data was available from the hourly topographic scans.

The wave strength parameter Ω_w is derived from well-known (see, e.g., Komar, 1971; USACE, 2002; Ashton and Murray, 2006) wave energy equations in combination with empirical relationships. The energy density (J/m^2) of a wave is

$$E = \frac{1}{8}\rho g H_w^2 \quad (17)$$

where H_w is the height of the wave. The product of this with the (group) velocity of the wave field c_g yields an equation for the power per unit length of the wave (perpendicular to travel direction—i.e., along the crest or trough):

$$\Omega_w = \frac{1}{8}\rho g H_w^2 c_g \quad (18)$$

Shallow water wave velocity is dependent only on the local water depth: the waves are non-dispersive and the velocity of a group of waves is equal to the velocity of individual waves. Nearshore bathymetry is laterally variable across a delta front and not universally available; therefore we use an empirically determined equation (USACE, 2002) to relate the depth of the water at wave-break to the height of the wave itself:

$$\Omega_w = \frac{1}{8}\rho g H_w^2 c_g = \frac{1}{8}\rho g H_w^2 \sqrt{\frac{3}{4} g H_w} = \frac{\sqrt{3}}{16}\rho g^{1.5} H_w^{2.5} \quad (19)$$

This parameter is thus strongly dependent on the wave height and represents the wave energy delivered to the coast per second, per meter of wave crest. Since we oriented the wave generator to produce wave crests subparallel to the coast, and since wave-driven sediment transport is primarily directed along the coast, the parameter may also be interpreted as power per unit distance along the coast. In our experiments, the waves produced by the wave generator had energy fluxes several orders of magnitude higher

than those of the fluvial or tidal inputs. Thus we held the wave energy constant and instead adjusted the fraction of time for which the wave generator was active, so that:

$$\Omega_w = f\frac{\sqrt{3}}{16}\rho g^{1.5} H_w^{2.5} \quad (20)$$

where *f* represents the intermittency factor. In the field, $f = 1$ if one is using mean annual wave height, or an appropriately reduced value if one is using storm-wave conditions.

Tides have properties of both fluvial and wave energy: near the coast, they create a periodically reversing, but quasi-steady, flow, although they are waves in a global context. Tidal power may be calculated with this quasi-steady flow as for fluvial power, but such a result would only be accurate within the channel(s) in which flow was measured. Such metrics are used for estimates of potential energy extraction for (electrical) power generation (Bryden, *et al*., 2005). This is not an effective measure of tidal power for the delta as a whole, however, because channel cross sections and flow velocity are highly variable across a network and over the period of a tidal cycle, and therefore no single tidal discharge could be calculated. Although Harris *et al*. (2002) used the wave energy density equation to compare tidal and wave energy in field sites, we do not believe it to be applicable, since tidal waves consist of a pair of bulges on either side of the Earth and the relationship between energy density and wave height is predicated on a near-infinite wave field. Thus, neither the fluvial nor wave strength parameters are the best measure of tidal energy.

Because the dominant feature of a tide is the variation in water elevation, the potential energy stored in water moved from low to high tide is one measure of the input of energy to the coast by tidal forces. The potential energy gained by water lifted by the

tide is simply the product of the weight of the water and the distance it is moved. Weight is the product of mass and gravitational acceleration, and mass is the product of density and volume:

$$PE_T = V_T \rho g H_T \quad (21)$$

where V_T is the volume of water moved and H_T is the tidal range.

The volume of water moved is the tidal prism, which can be approximated as a wedge: the width of the wedge is the width of the delta L_D, the length of the wedge the length of the intertidal zone L_I, and the height of the wedge is the tidal range H_T. (Fig. 28)

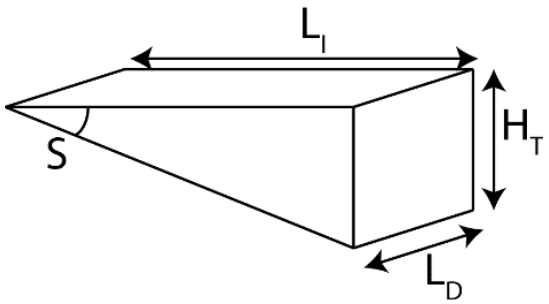

Figure 28: Diagram of a simplified tidal prism.

The volume of the wedge is therefore:

$$V_T = \frac{1}{2} L_i L_D H_T \quad (22)$$

so the potential energy is:

$$PE_T = \frac{1}{2} L_i L_D H_T \rho g H_T \quad (23)$$

In order to match the units of the wave and fluvial parameters, energy must be normalized by a time scale and a length scale. The tidal period T_T is an obvious timescale; we use half the period because that is the length of time over which the water is lifted from low to high tide. We use L_D as the length scale since the tide acts over the full width of the delta:

$$\Omega_T = \frac{\frac{1}{2}L_i L_D H_T \rho g H_T}{\frac{1}{2}T_T L_D} = \frac{\rho g H_T^2}{T_T} L_i \tag{24}$$

The slope of the intertidal zone S is the tidal range divided by the length of the zone. Therefore, the length is the tidal range divided by the slope. The tidal parameter can then be written as

$$\Omega_T = \frac{\rho g H_T^2}{T_T} \frac{H_T}{S} = \frac{\rho g H_T^3}{T_T S} \tag{25}$$

Experimental Setup/Methods:

The Delta Basin facility at St. Anthony Falls Laboratory at the University of Minnesota consists of a basin 5 m by 5 m in area and 0.5 m deep, with a stationary floor. Water and sediment are supplied to the basin to create a delta deposit; in the experiments reported here, the feed point was in one corner of the basin such that the resulting delta spanned a 90° arc. The basin is equipped with a motorized, siphon-connected weir. A computer programmed with the run parameters controls the motor, which drives the weir up and down. This in turn controls the water surface elevation in the main basin: any

elevation difference between the water surface in the basin and the weir leads to an exchange of water between them until equilibrium is reached. (Fig. 29)

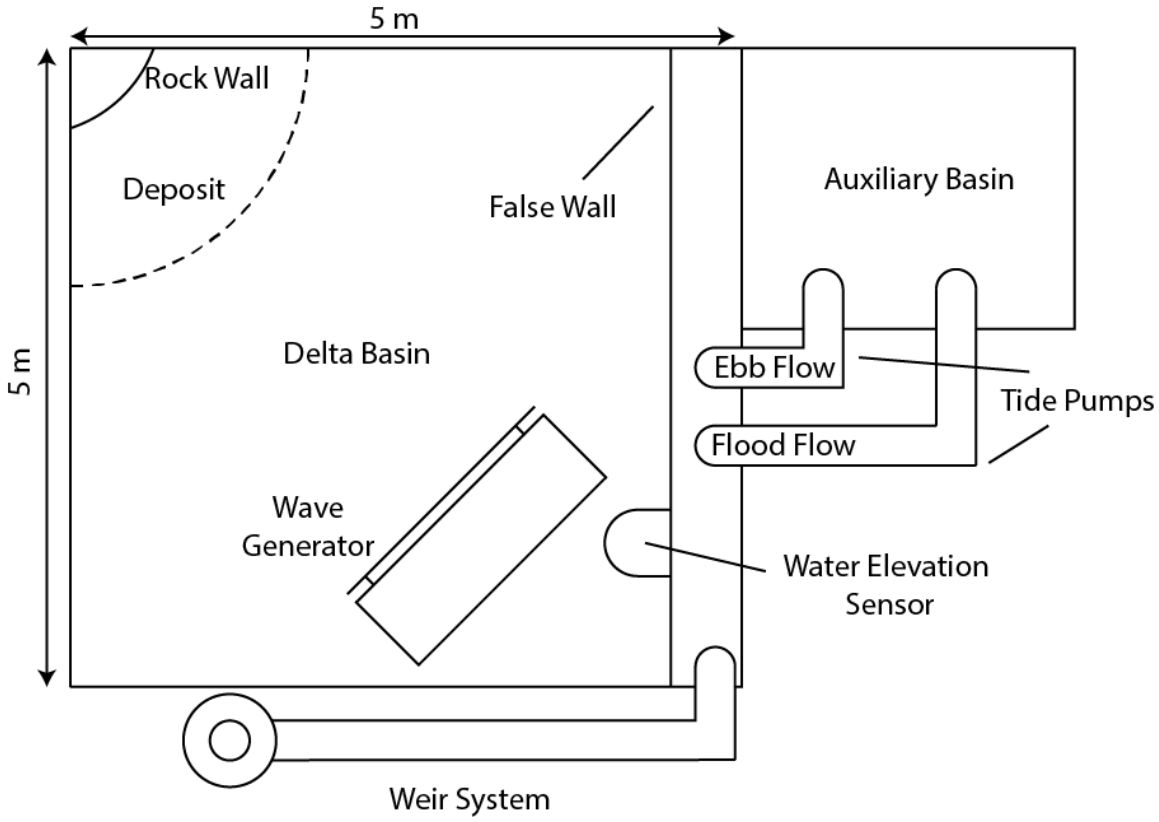

Figure 29: Schematic diagram of the Delta Basin facility. False wall is ~10 mm above the floor of the basin and reduces momentum of flow exiting the flood tidal pump. Wave generator is anchored in place.

The basin has a water-elevation sensor with precision of 0.1 mm, which relays its measurements to the control computer. The true elevation is compared with the programmed elevation, and both the error and the elevation are recorded. Typical errors are 0.1-0.3 mm, or ~0.1%.

The computer uses the programmed parameters to control the rotation rate of the auger that feeds sediment and the pump that supplies water to the basin. The resultant discharge rates are thereby held constant within an error of about 1%.

We took topographic scans every run hour at a resolution of 1 mm horizontally and 0.1 mm vertically. The scanning system is composed of a laser sheet and camera mounted on a motorized, spatially-referenced data cart that runs on rails along the basin walls; perturbations in deposit topography distort the shape of the intersection between the beam and sediment surface, the intersection line is digitized, and the distortion converted to surface elevation trigonometrically. Overhead photographs were taken from a ceiling-mounted camera every 10 s during tidal or wave action; image frequency during the purely fluvial run out phase was one every 30 s. Post-orthorectification image resolution is approximately 1 mm per pixel.

The results discussed in this paper come from a single long experiment with multiple phases. Before the experiment began, we constructed a subdelta sediment step ~2 m in radius and 0.17 m high in the corner of the basin closest to the inflow point. This subdelta was composed mainly of quartz sand ($D_{50} = 0.5x10^{-3}$ m), covered with a layer of fine walnut sand. The step is there simply to reduce the time needed to grow the delta, and the study delta is a self-formed deposit that covers the subdelta surface entirely (Fig. 30).

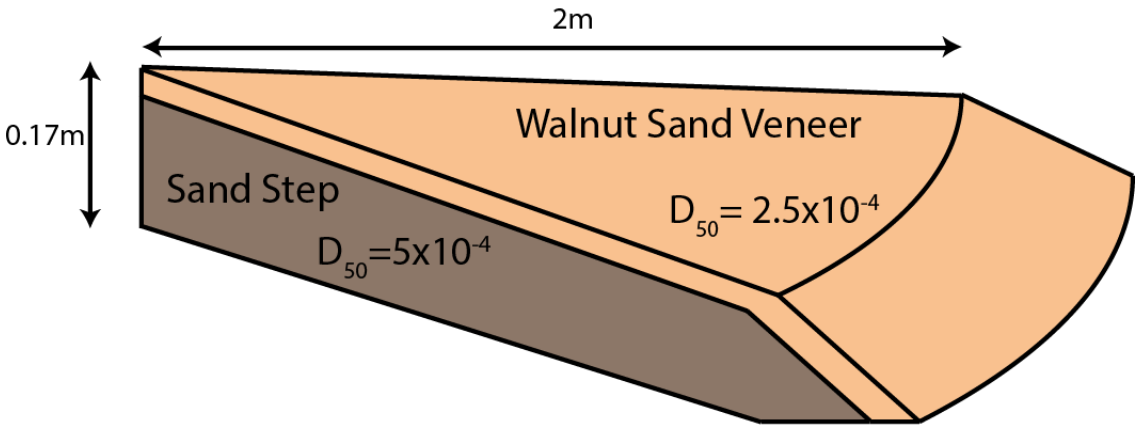

Figure 30: Schematic cross-section through subdelta prior to the beginning of deposition. Note that the total height of the wedge is 0.17m, 0.015m below mean base level for the experiment.

The water surface elevation is held constant at 0.185 m and the deposit progrades rapidly across the subdelta before entering deeper water at the edge of the subdelta. This eliminates the need for time-consuming run-out phases and allows base level and water and sediment discharge to remain constant throughout the experiment.

The sediment used for this experiment was ground walnut shell (D_{50} = 0.25 mm). Walnut shell has a low density (1350 kg/m^3), and is therefore more easily entrained in weak flows than quartz sand. Previous experiments have used coarse (D_{50} = 1 mm) walnut shell sand, but we found that weak tides were unable to transport this sediment. In addition, the lower limit of the size of channels is in part set by the grain size; we chose a finer sediment to allow the formation of smaller features.

The sediment and water were thoroughly mixed in a PVC tube before entering the basin through a flow diffuser. Concentrated dye was added to the tube so that the locations of the channels and shoreline could be more easily identified from overhead imagery. The volume of dye added to the water and sediment mixture was three orders of magnitude less than the water discharge and therefore represented a negligible change

to the total influx. The flow diffuser is a column of pea gravel set into the apex of the deposit; its primary purpose is to reduce the downward momentum of the flow before it encounters the deposit.

To create the tides applied to the deposit, the basin is equipped with a set of pumps connected to an auxiliary basin for rapid cycling of base level. The tidal pumps cycle water between the main basin and a smaller, 2 m by 2 m by 0.5 m auxiliary basin; this allows the water to be reused, rather than pumped anew each tidal cycle. The discharge rate of the pumps is computer controlled and calibrated to produce a pseudosinusoidal variation of a predefined vertical range and period in the water surface elevation in the main basin. This regular, relatively rapid cycling mimics the tidal fluctuation in sea level during a tidal cycle. The waves were generated by a 2 m long, 0.05 m tall oscillating bar. The amplitude of the oscillation was adjustable and the frequency of the oscillation was programmed via the computer that controls the motor driving the arm. The arm is mounted on a floating platform, which allows simultaneous generation of tides and waves. In our experiments, we used a frequency of 1 Hz and measured the height to be 0.04 m. As discussed above, we held both the wave amplitude and frequency constant and instead adjusted the fraction of time for which the wave generator was active, controlling the wave energy via the intermittency factor *f*. For the wave-influenced portion of our experiments, *f* varied between $3x10^{-3}$ and $3x10^{-2}$, or between 16 and 141 seconds per hour of run time (Table 3).

				Percent of Total Energy		
Run Hours	Channel Slope	Tidal Range (m)	Wave Intermittency	Fluvial	Tidal	Wave
0-55	0.0100	0.000	0.000E+00	100.0	0.0	0.0
55-75	0.0110	0.019	1.844E-02	18.9	46.8	34.3
75-90	0.0095	0.022	9.222E-03	14.7	69.8	15.5
90-105	0.0144	0.015	4.380E-03	50.4	32.9	16.6
105-120	0.0131	0.020	6.640E-03	29.7	53.9	16.3
120-135	0.0125	0.010	3.020E-03	65.1	17.9	17.1
135-150	0.0082	0.011	7.684E-03	35.8	27.8	36.4
150-165	0.0120	0.009	1.134E-02	44.3	10.3	45.4
165-180	0.0084	0.015	3.923E-02	12.6	23.4	63.9
180-195	0.0153	0.015	2.324E-02	30.8	18.5	50.7
195-210	0.0135	0.018	1.411E-02	29.3	37.6	33.2
210-225	0.0135	0.020	2.127E-02	0.0	50.0	50.0
215-220	0.0131	0.022	1.418E-02	0.0	67.3	32.7
220-225	0.0136	0.022	1.085E-02	0.0	74.3	25.7
225-230	0.0137	0.040	0.000E+00	0.0	100	0.0

Table 3: Relative fluvial, tidal and wave proportions for each stage of the experiment, with associated (independent) tide and wave variables. Slope was measured but not set.

We held the tidal period constant at 120 s—this allowed a greater tidal range, and thus a greater range of potential parameter values. Tidal range varied between 9 mm and 40 mm (Table 3).

To investigate the interaction of fluvial, wave and tidal effects on the experimental delta, the deposit was subjected to a suite of energy proportions (Table 3). The total power applied to the delta (the sum of fluvial, tide and wave parameters) was not held constant; to do so would have required adjustment of the water discharge since discharge is the only independent variable in the fluvial energy parameter our facility allows us to control. Because the discharge rate sets channel dynamics and topset slope, additional run time would have been required for the deposit to reach equilibrium before applying a particular combination of wave and tide energies. Holding the fluvial

discharge constant ensured that any allogenic changes would be the result of changes in applied basinal effects.

Because of the dependence of the fluvial parameter on the slope of the deposit, we could not determine its exact value in advance of any given phase. Since the value of the fluvial parameter was used to calculate the total power, the values of the tidal and wave parameters—and therefore the tide height and wave intermittency—also could not be calculated prior to the phase itself. In order to estimate the parameter values, and tide and wave generator settings, for a new phase, we used an average of the channel slopes from the previous five hours of topography scans. The use of data from multiple scans allowed us to remove the effects of autogenic variability in the topset slope.

The initial phase of the experiment was purely fluvial: the delta was allowed to grow until it entirely covered the subdelta. This run-out period also provides a set of data to which to compare the dynamics and morphology of tidal- and wave-influenced deltas. We held (mean) water surface elevation, water discharge and sediment discharge constant throughout the run (Table 4).

Parameter	Description	Value
Q_w	Water discharge	10^{-4} m^3/s
Q_s	Sediment discharge	10^{-6} m^3/s
D_{50}	Sediment Size	$2.5x10^{-4}$ m
ρ_s	Sediment Density	1350 kg/m^3

Table 4: Experimental parameters kept constant throughout the run. Note that also the value of Qw was held constant, the fluvial slope was not, which allowed variability in the absolute value of Ωw.

At the end of each phase, the average topset channel slopes were determined and the settings for the next phase calculated. During phases with tidal forcing, the tide generators ran throughout the phase. The wave generator was run close to the midpoint

of a run hour such that the waves were evenly distributed across mid-tide. (If the wave intermittency were 30 seconds per hour, for example, the waves would be run from 15 s before to 15 s after the time of mid-tide.) We also alternated between running the waves during the rising and falling limbs of the tide. The length of each phase was set to 15 hours: this was the time needed for the topset to be resurfaced by channel migration.

Analysis Methods:

The overhead images collected during the experiment were orthorectified using MATLAB image processing tools and a pre-calculated correction matrix, and were then used for both qualitative and quantitative analysis of the subaerial dynamics of the delta.

In order to generate shorelines and quantitatively analyze channel dynamics, we binarized the images into land-water maps. Because the water was dyed blue, there was a significant color contrast between 'dry' areas and channel and basin areas; the ratio of the luminosities of the red and blue bands was computed for each pixel in an image. We then defined a threshold value to convert the grayscale (ratio) images to binary maps of wet and dry pixels.

We used the automatic method developed by Shaw *et al*. (2008) to define one shoreline for every five run hours. This method produces a suite of shorelines by determining, for each wet pixel, the total angle through which basinward open water can

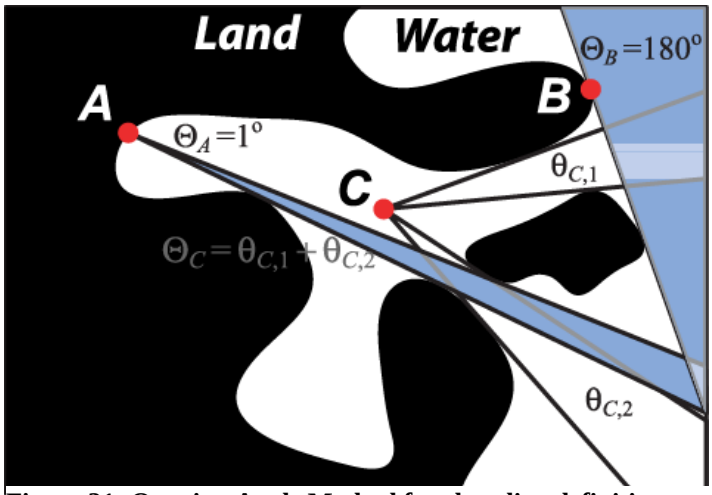

Figure 31: Opening Angle Method for shoreline definition. After Shaw *et al*., 2008.

be viewed without interruption by a dry pixel (Fig. 31).

A single shoreline is defined as the vector produced by a given contour (here, 45°) of this angular view map: shorelines generated from smaller thresholds extend farther into inlets and behind barrier islands. Shaw's method is computationally intensive, but produces a shoreline at the resolution of the image itself that is consistently defined and continuous across channel mouths and inlets.

Rugosity, or shoreline sinuosity, is a measure of the complexity of the shoreline. It is calculated as the ratio between the shoreline length (measured at the highest resolution) and the length of the convex hull around the delta (Fig. 32). We use the convex hull, rather than straight-line distance between the ends of the shoreline vector, to remove the effects of bulk delta shape and focus the metric on roughness caused by features (e.g., channels) much smaller than the scale of the entire delta.

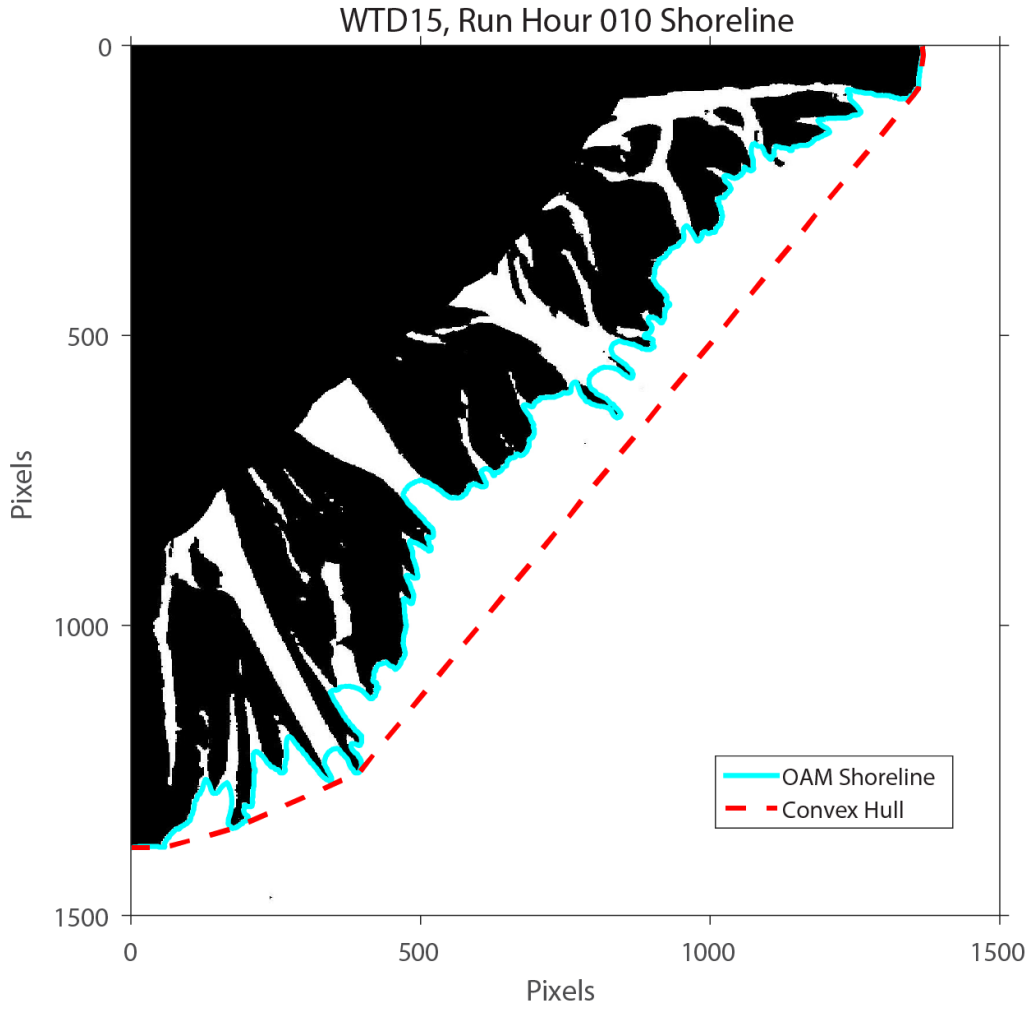

Figure 32: Binarized image of the deposit at run hour 10, with overlay of OAM-generated shoreline (solid cyan) and convex hull (dashed red). Note that the OAM shoreline faithfully follows the land-water interface except for inlet crossings.

Shoreline direction and curvature are the first and second (spatial) derivatives of the shoreline position vector. Because differentiation amplifies noise, we applied a Savitzky-Golay smoothing filter (order=2, filter length=51) on the shoreline position vectors before calculating azimuth. This class of smoothing operations was selected for their ability to remove high-frequency variability while preserving the shape of a curve (Schaefer, 2011). We then detrended the direction vector to remove the effects of bulk shape and orientation: the statistics of a perfectly smooth north-south shoreline should be

the same as the statistics of an equally-smooth east-west trending shoreline. We calculated the curvature of the detrended shoreline using Holoborodko's (2008) smoothing differentiator.

Directional continuity of a shoreline is a measure of the distribution of runs of near-constant azimuth. We separated the detrended direction vector into segments of cumulative azimuthal change of less than 45°, such that the segments did not overlap. We restricted our analysis to segments greater than 1.414 pixels (the maximum distance between two adjacent pixel centers) in length to reduce spurious signals due to imperfect smoothing; these tiny fragments composed nearly half of the original segments. Because the lengths of the remaining segments were positively skewed (mean skewness = 1.65) we declared a significant run to be one in the 66^{th} percentile of length or greater.

Shoreline piercing features are channels and inlets that break the continuous land/water boundary. We analyzed the smoothed shoreline for proximity to land ('dry') pixels; those shoreline positions not adjacent to land pixels were marked 'wet'. 'Wet' pixels represent channel and inlet crossings. As with the directional continuity, we analyzed the dry/wet shoreline vector for runs of consistent value, restricting 'runs' to lengths of greater than 1.414, and analyzing only those runs in the in the 66^{th} (and higher) percentile of length.

Channels on the subaerial portion of the delta are neither stationary nor permanent features. We analyzed channel dynamics by comparing successive pairs of binarized land-water maps. We chose 120 s as the interval between images so that tidal phase (in

this case, low tide) would be consistent across the pairs. Each image was subtracted from its predecessor, and we recorded the number and location of changed pixels.

Results:

As the delta prograded across the top of the step, its area grew linearly with time, as dictated by basic mass balance. Because the basin is flat-bottomed, this linear growth should have continued once the delta prograded over the edge of the step, though at a reduced rate (reflecting the greater water depth). After run hour 55, the topset area of the delta continued to increase, but not nearly as smoothly or regularly as it had during the initial growth phase (Fig. 33).

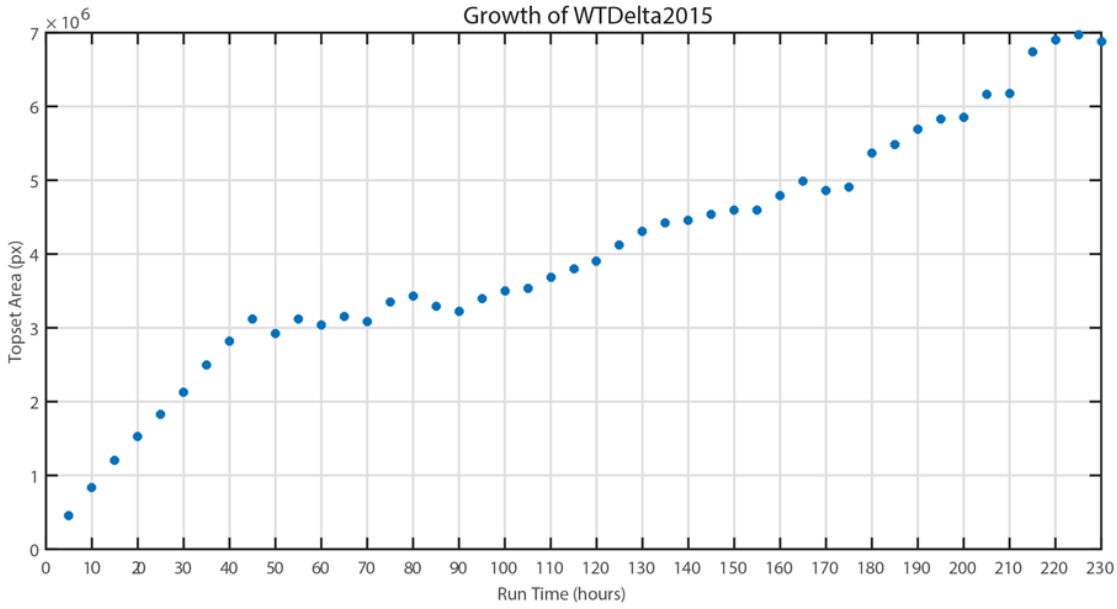

Figure 33: Topset area (pixels) of the deposit through the experiment. Note the smooth, near-linear progression from 0 to 45 hours, and the break in slope and variable growth rate thereafter. (This break occurs earlier than the run hour 55 initiation of waves due to the perturbation to the basin caused by the installation of the wave maker at hour 48.)

Once tide and wave energy were introduced at run hour 55, the delta rapidly (<5 hours) developed a low (~$6x10^{-3}$), shoreline-parallel ridge of sediment immediately landward of the shoreline. This berm was cut by not only the main fluvial outlet but by several smaller (10 – 20 mm wide) channels, which served as conduits for both flood and ebb tidal flow (Fig. 34). These channels were persistent from hour to hour; the largest were maintained through >20 periods of wave activity. Some of these channels formed as a consequence of abandonment of old fluvial mouths, but many formed spontaneously to replace others closed by a wave event. The characteristic feature of these berm-cutting channels is their lack of connection to the main flow: they receive no fluvial input and are wholly maintained by tidally-driven currents. These channels generally traversed the entire intertidal zone. The characteristic shoreward widening seen in tidal channels in the field was present only in those phases with the highest proportions of tidal energy; most notably phase 15 (100% tidal energy, the experimental analog to tidal flats in the field). The sinuosity of the tidal channels was 2-3 times that of single-threaded fluvial channels; however this sinuosity may owe more to the topographic low behind the berm—which encouraged a near right-angle bend—than with any morphodynamic difference.

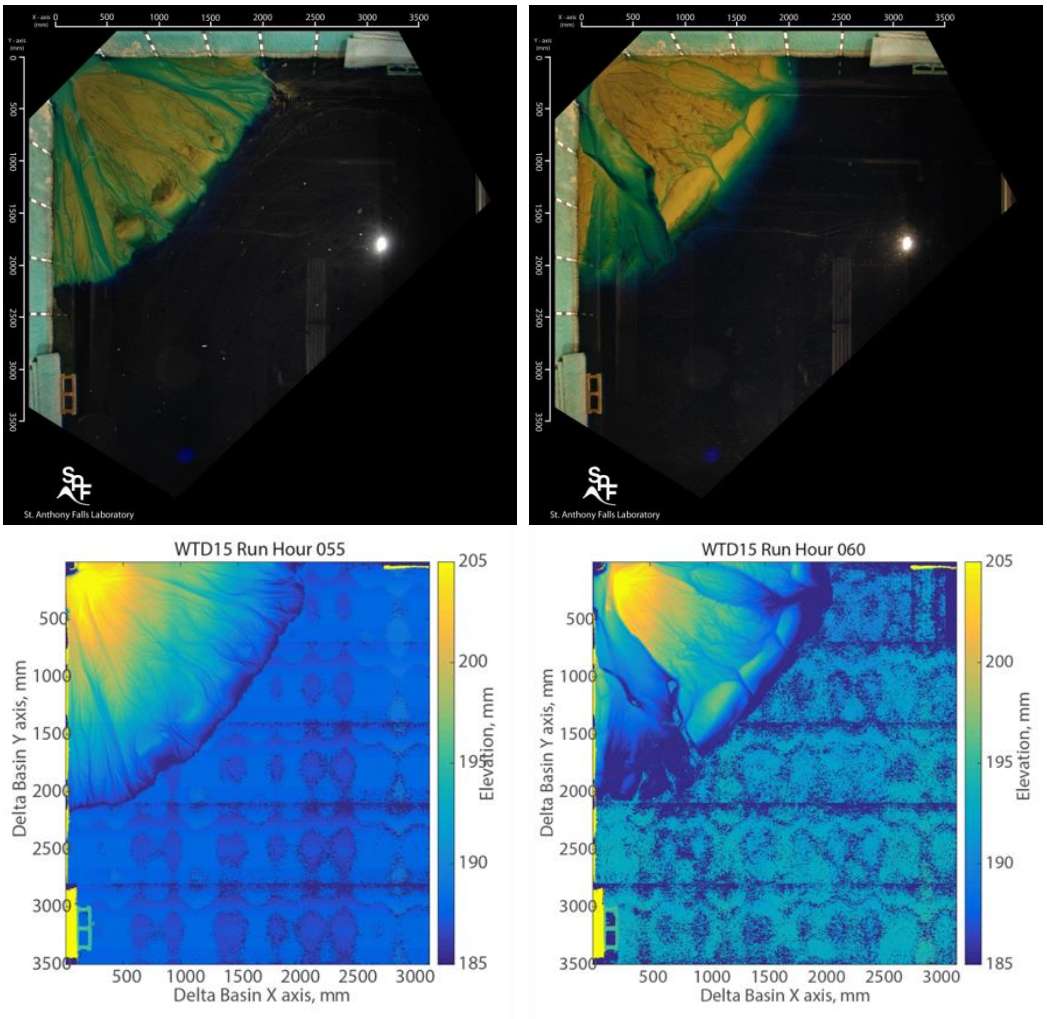

Figure 34: Overhead photographs and topography scans of the deposit at run hour 55 (left) and 60 (right). Note the development of a 100-200 mm wide, shoreline-parallel ridge and the 10-20 mm wide channels cutting through it. The photograph at hour 60 was taken at during the ebb limb at approximately mid tide. Elevation variation in open water is an artefact of the scan process; particulates on the water surface cause variance in reflectivity and false returns.

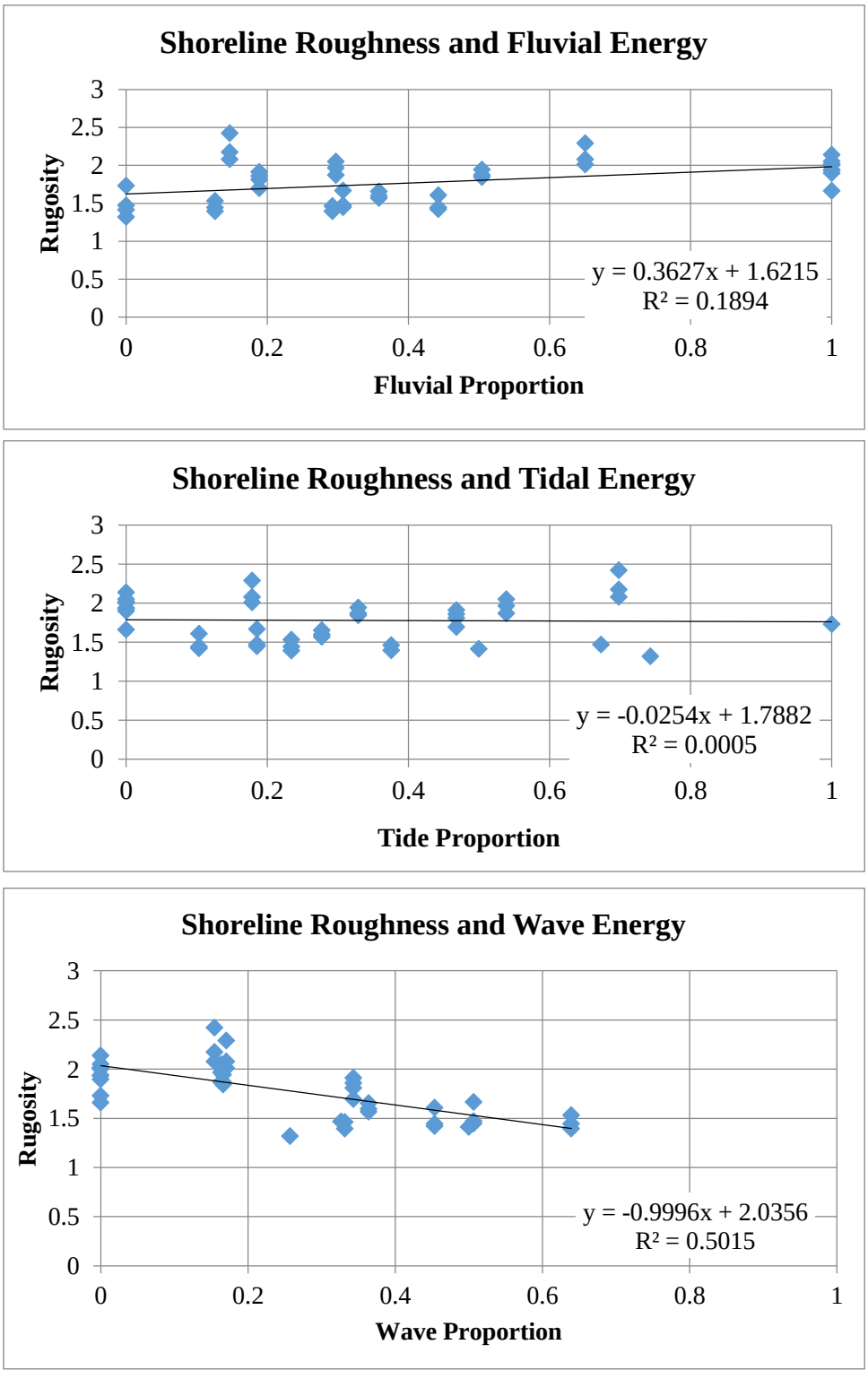

Figure 35: Shoreline roughness compared to energy proportions: note that the strongest correlation is with the proportion of wave energy incident on the deposit.

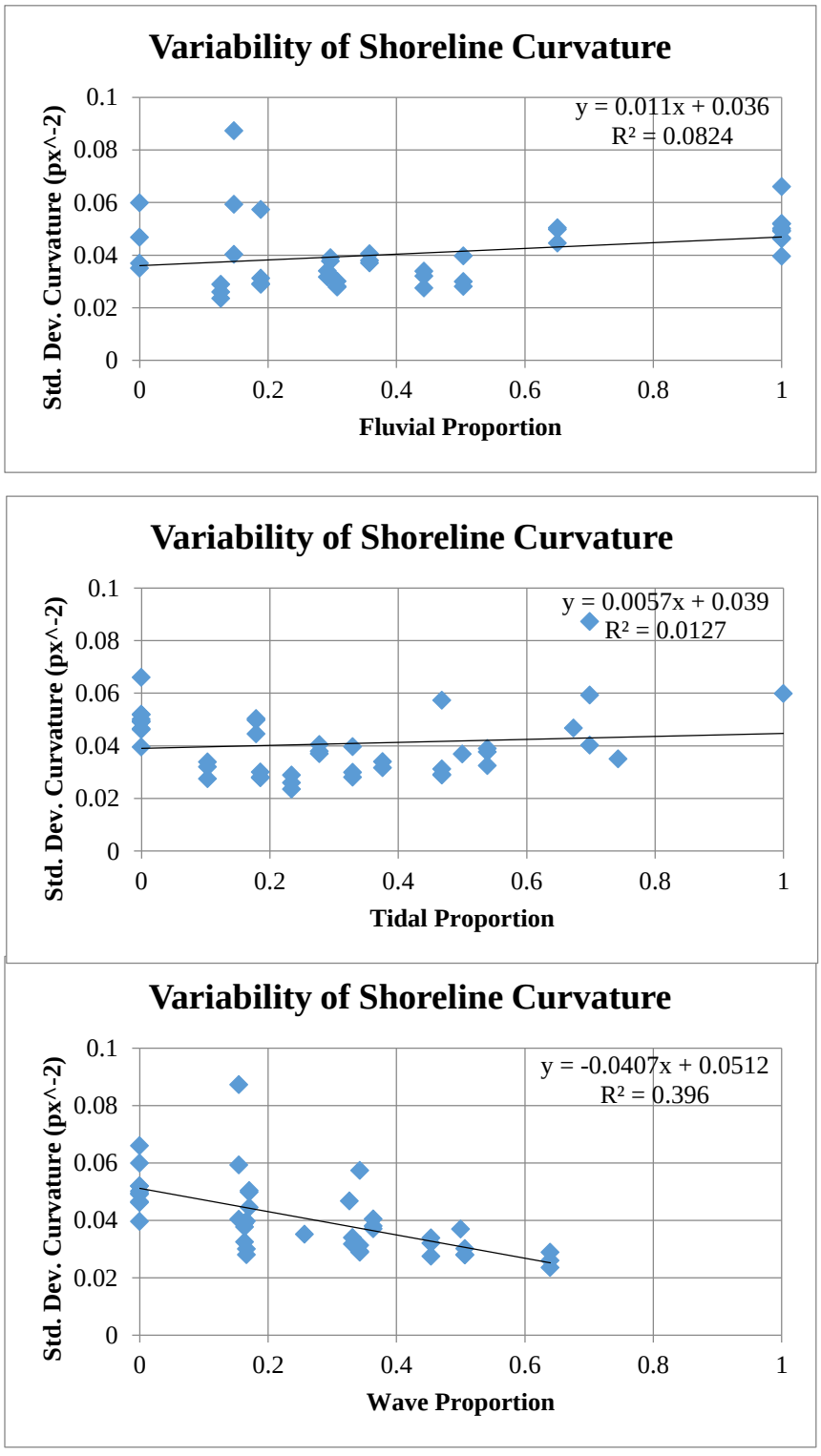

Figure 36: Standard deviation of shoreline curvature values compared to energy proportions.

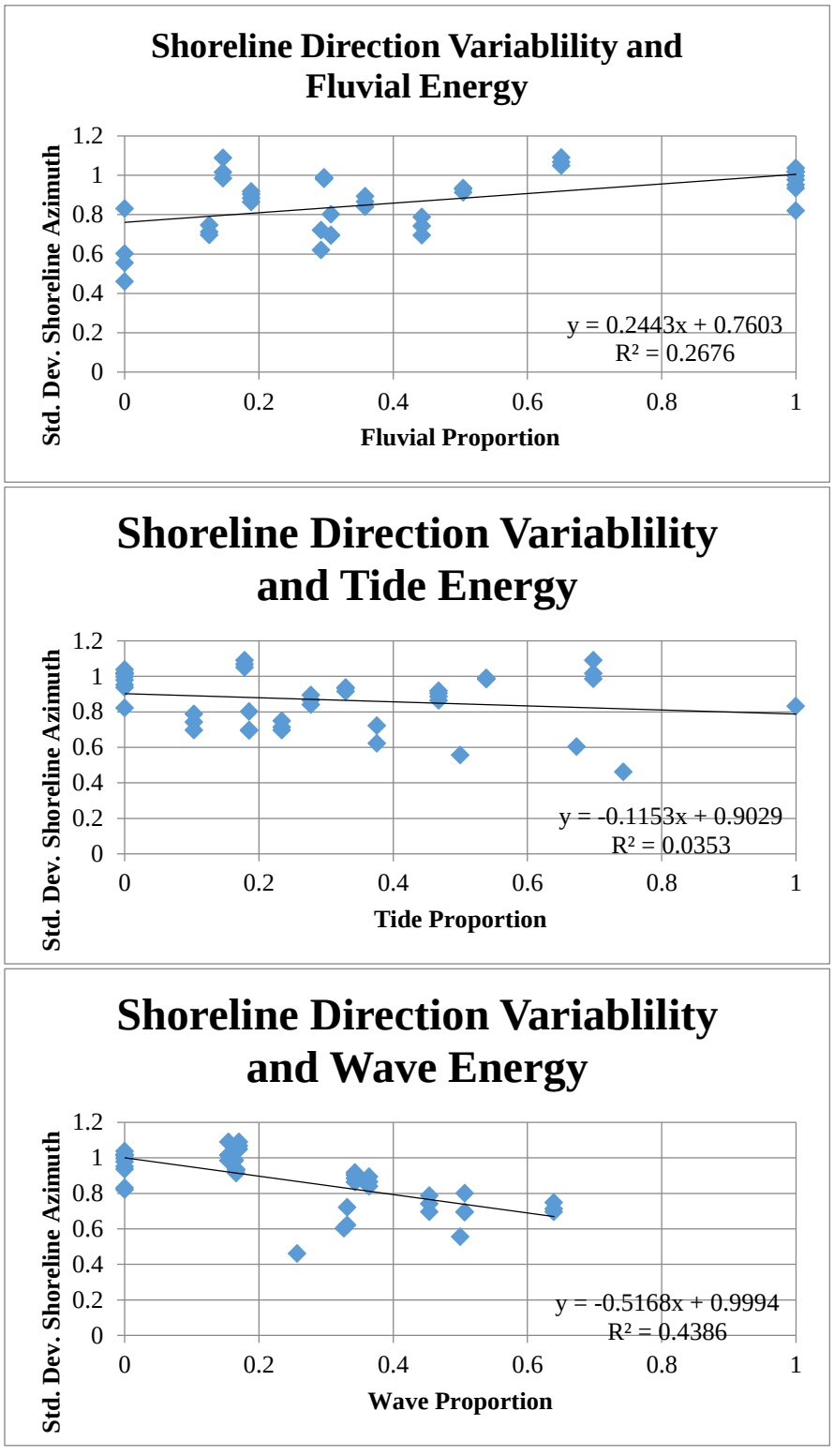

Figure 37: Standard deviation of (mean) shoreline azimuth compared to energy proportions.

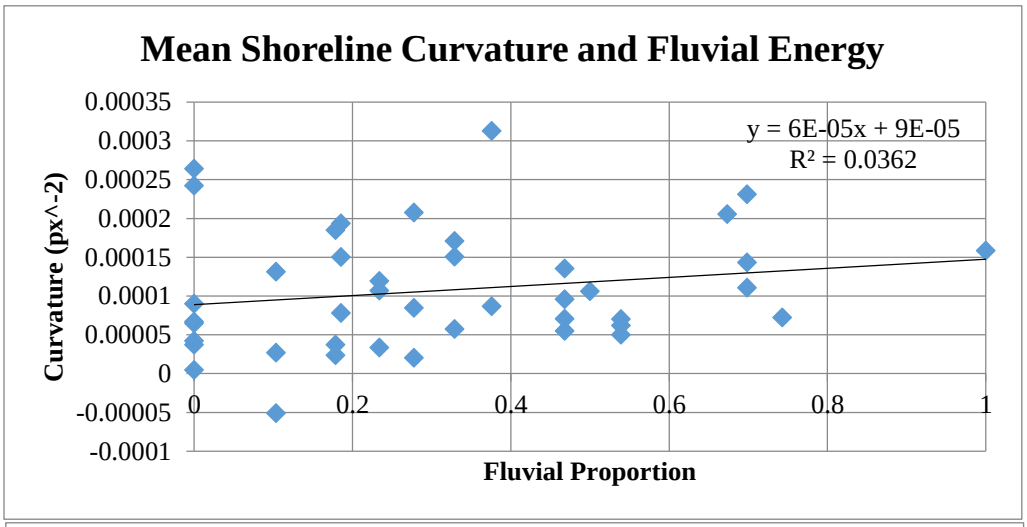

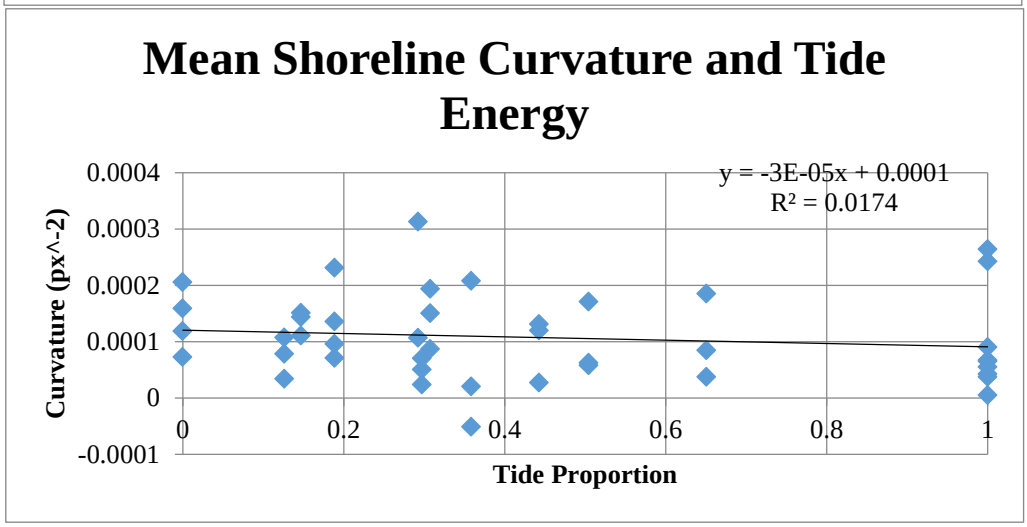

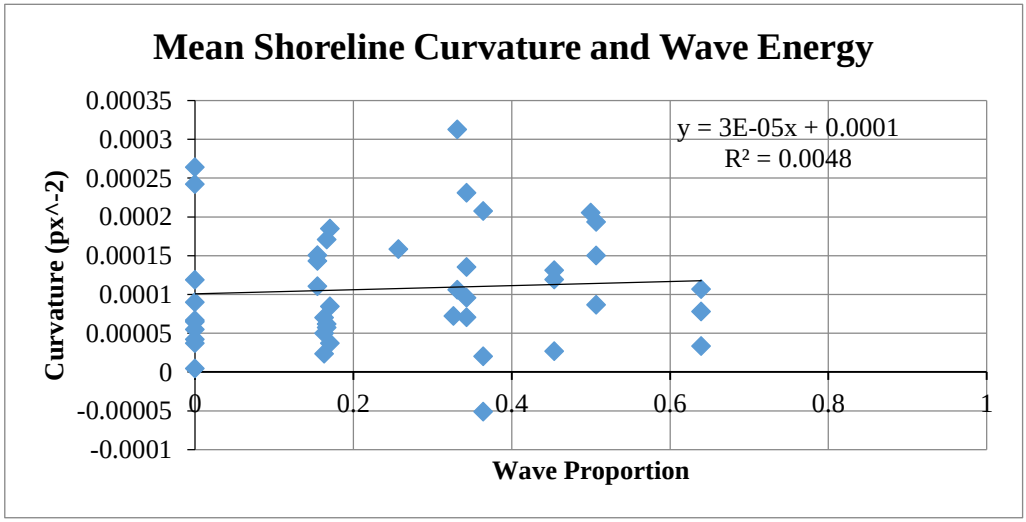

Figure 38: Mean shoreline curvature compared to energy proportions

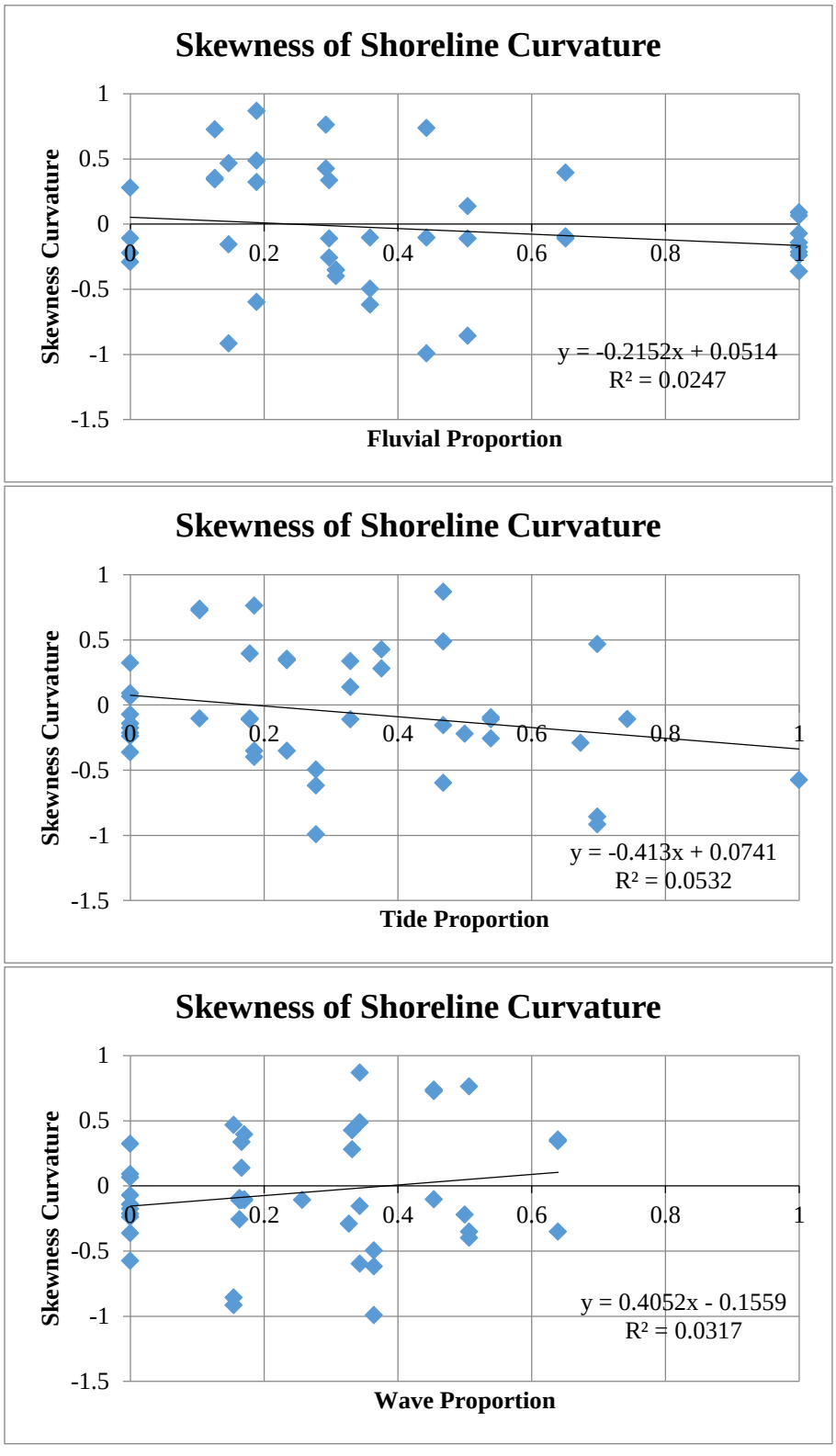

Figure 39: Skewness of shoreline curvature values compared to energy proportions.

Channel slope did not vary systematically, either with time or with wave or tidal energy proportion (Table 3). Shoreline rugosity was most strongly correlated to the proportion of wave energy over the course of the run: the greater the wave contribution to the total energy, the lower the roughness. Rugosity was weakly positively correlated with fluvial proportion, and no correlation was found between tidal energy proportion and rugosity (Fig. 35).

Overall variability of shoreline curvature (Fig. 36) and shoreline direction (Fig. 37) (as measured by their standard deviations) were also most strongly correlated with the proportion of incident wave energy, and most weakly correlated with tidal energy. Shorelines experiencing relatively greater amounts of wave energy tended to have lower azimuthal variability. Mean curvature and the skewness of the curvature of the shorelines were not correlated with any of the three (Figs. 38 and 39).

Directional continuity—that is, the mean significant length of low-curvature segments of the shoreline—was most closely correlated with wave energy proportion, with higher relative wave energies yielding longer runs. (Fig. 40) The mean direction of these significant runs was not well correlated with any energy input (Fig. 41). The longest mean continuous runs of dry points along the shoreline vector were associated with the highest proportion of wave energy: more wave energy is associated with fewer inlets (Fig. 42). Table 5 summarizes correlation coefficients for these shoreline metrics.

We measure channel stability using the rate of change in wetness state of the topset. The number of pixels that change value between two sequential images is normalized by the total pixels held in common between them and is a measure of the rate

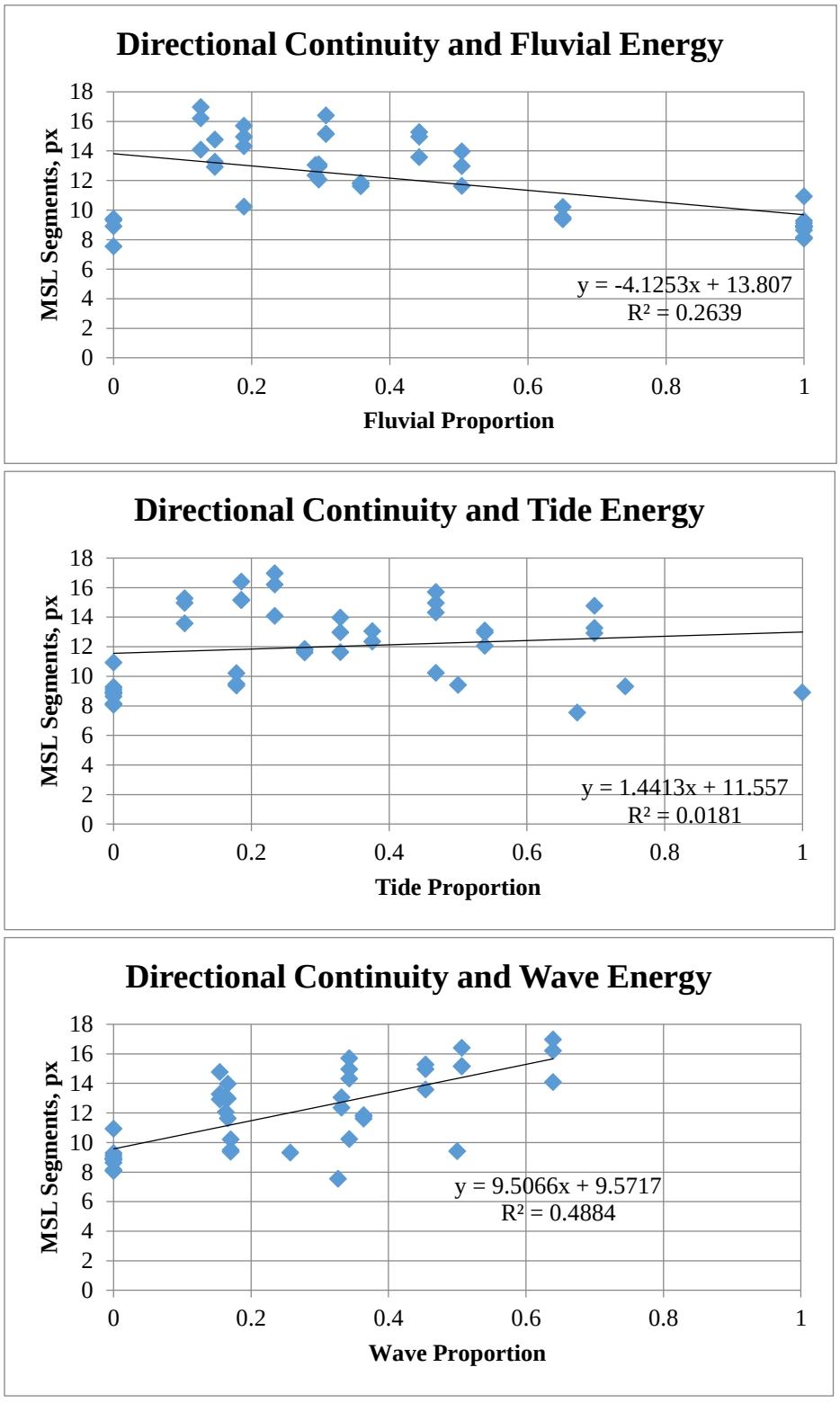

Figure 40: Directional continuity compared to energy proportions.

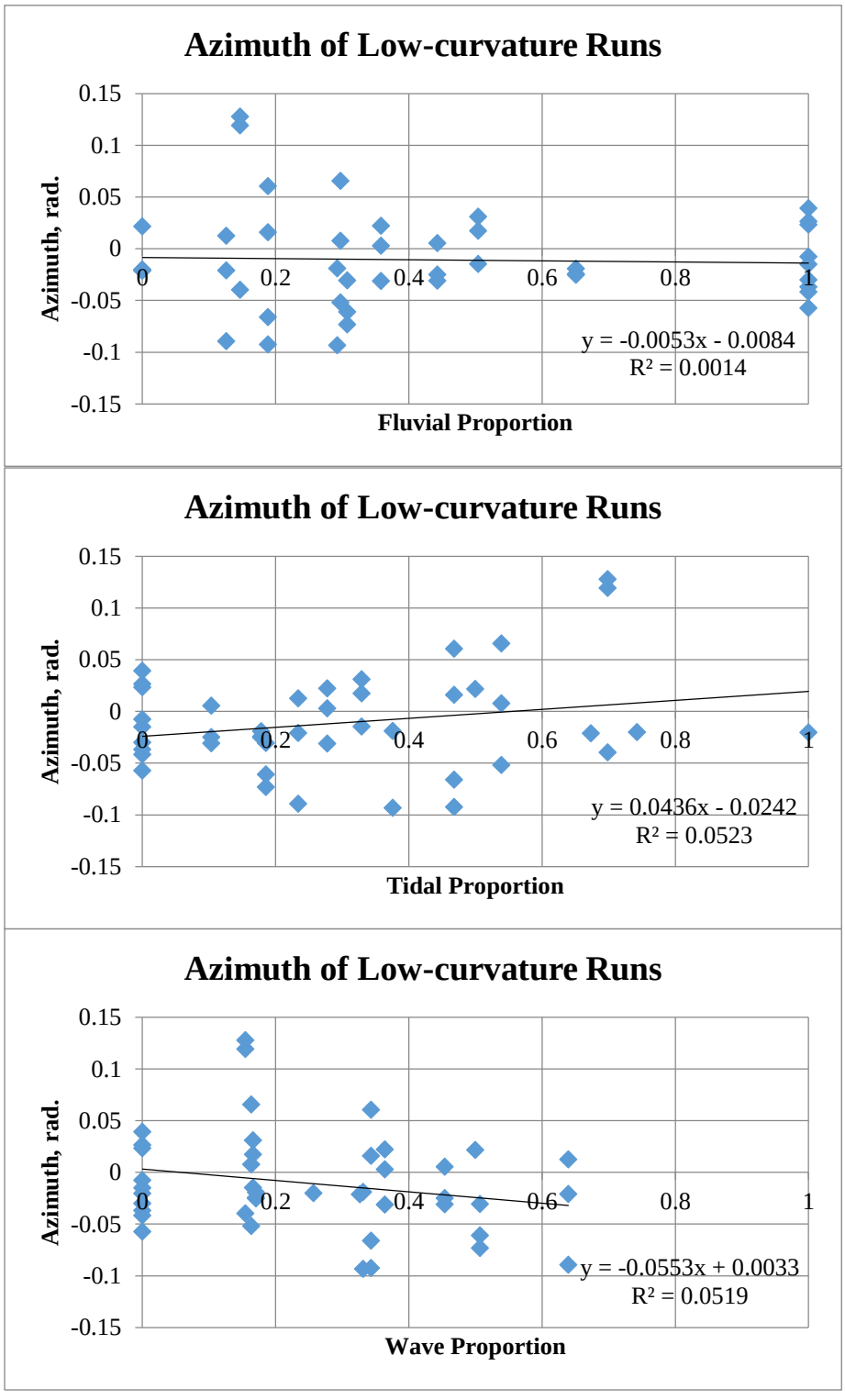

Figure 41: Azimuth of runs of low total change in direction compared to energy proportions.

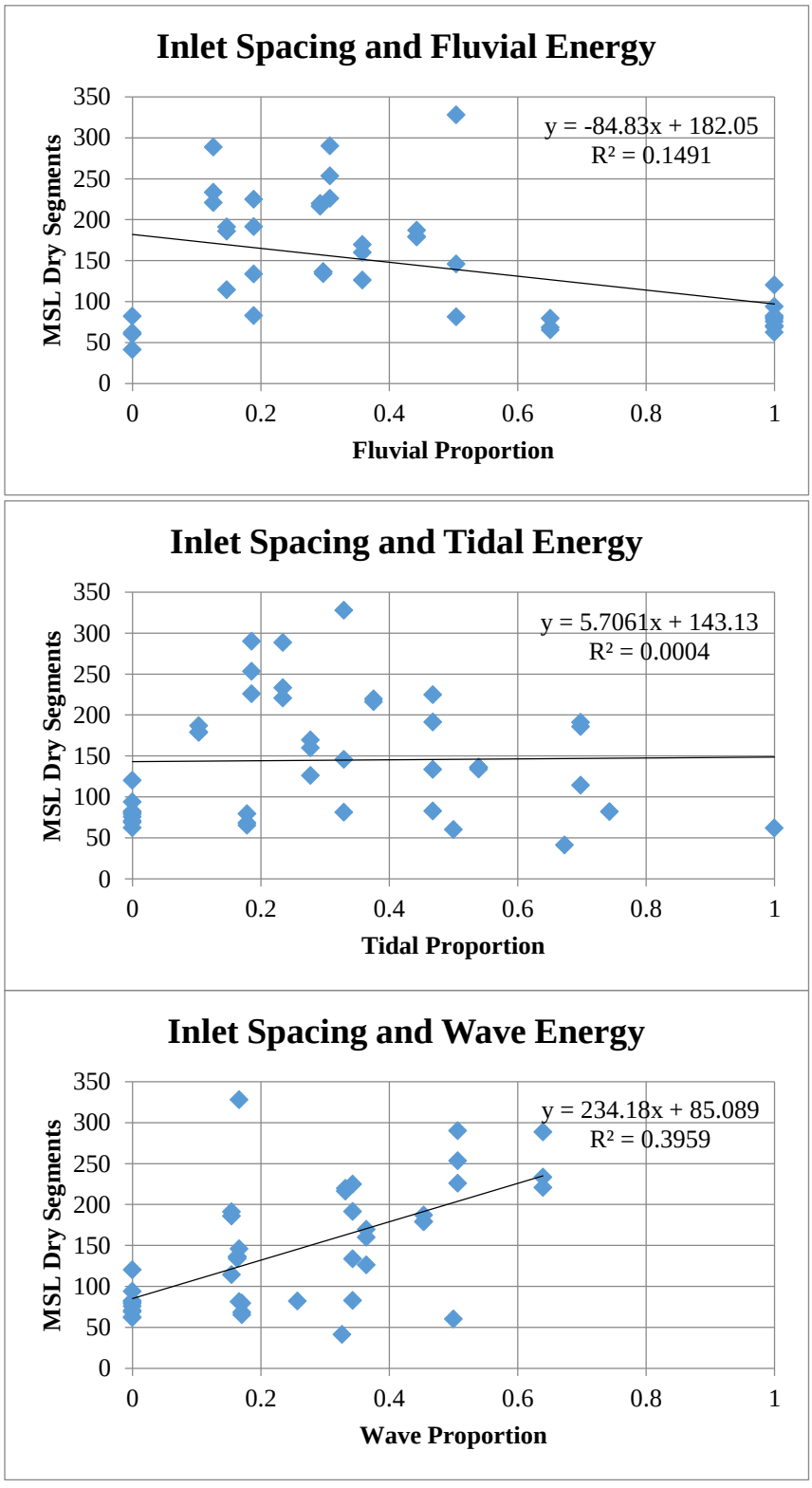

Figure 42: Mean length of significant runs of dry pixels along the shoreline.

	Fluvial	Tidal	Wave
Rugosity	0.189406	0.000523	0.501458
St. Dev. Shoreline Curvature	0.082382	0.0126664	0.396018
St. Dev. Shoreline Azimuth	0.2831	0.0353279	0.438626
Mean Shoreline Curvature	0.017354	0.0146738	0.004778
Curvature Skewness	0.004634	0.053201744	0.031675
Length (Runs low Δ Direction)	0.26387	0.018149185	0.48837
Azimuth (Runs low Δ Direction)	0.001383	0.052295105	0.051883
Length (Runs of dry pixels)	0.149063152	0.00038004	0.395906

Table 5: Summary of the correlation coefficients between the values of each metric and fluvial, tidal and wave energy proportions.

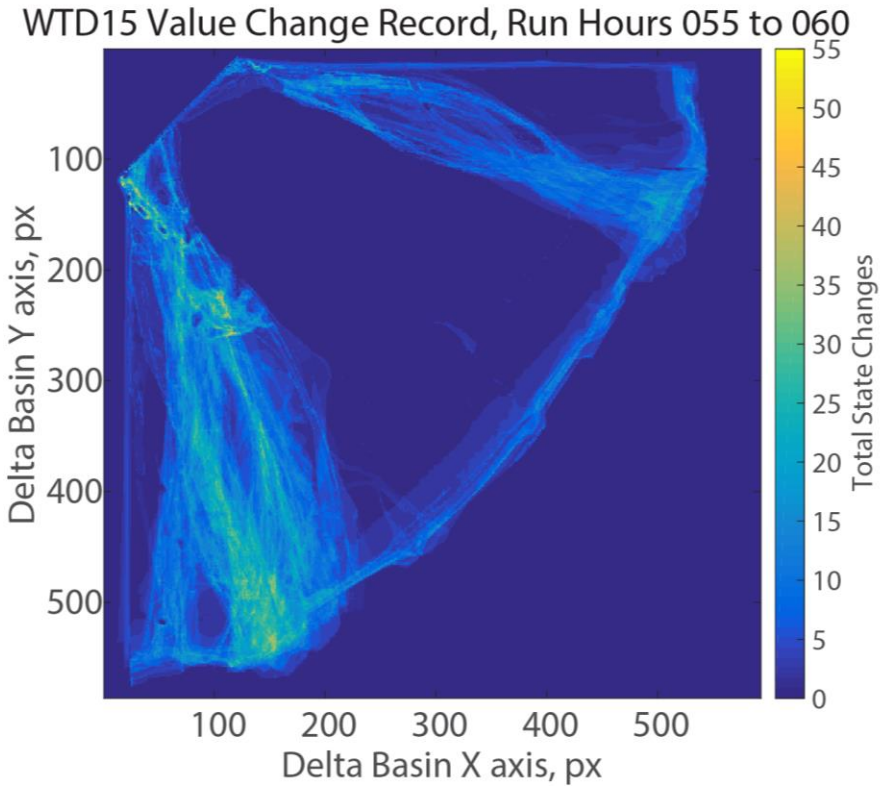

Figure 43: Five hour record of wetness state changes. Note that the areas with the greatest number of wet/dry changes are the channels. The changes around the edges and the shoreline are mainly due to fluctuations in lighting.

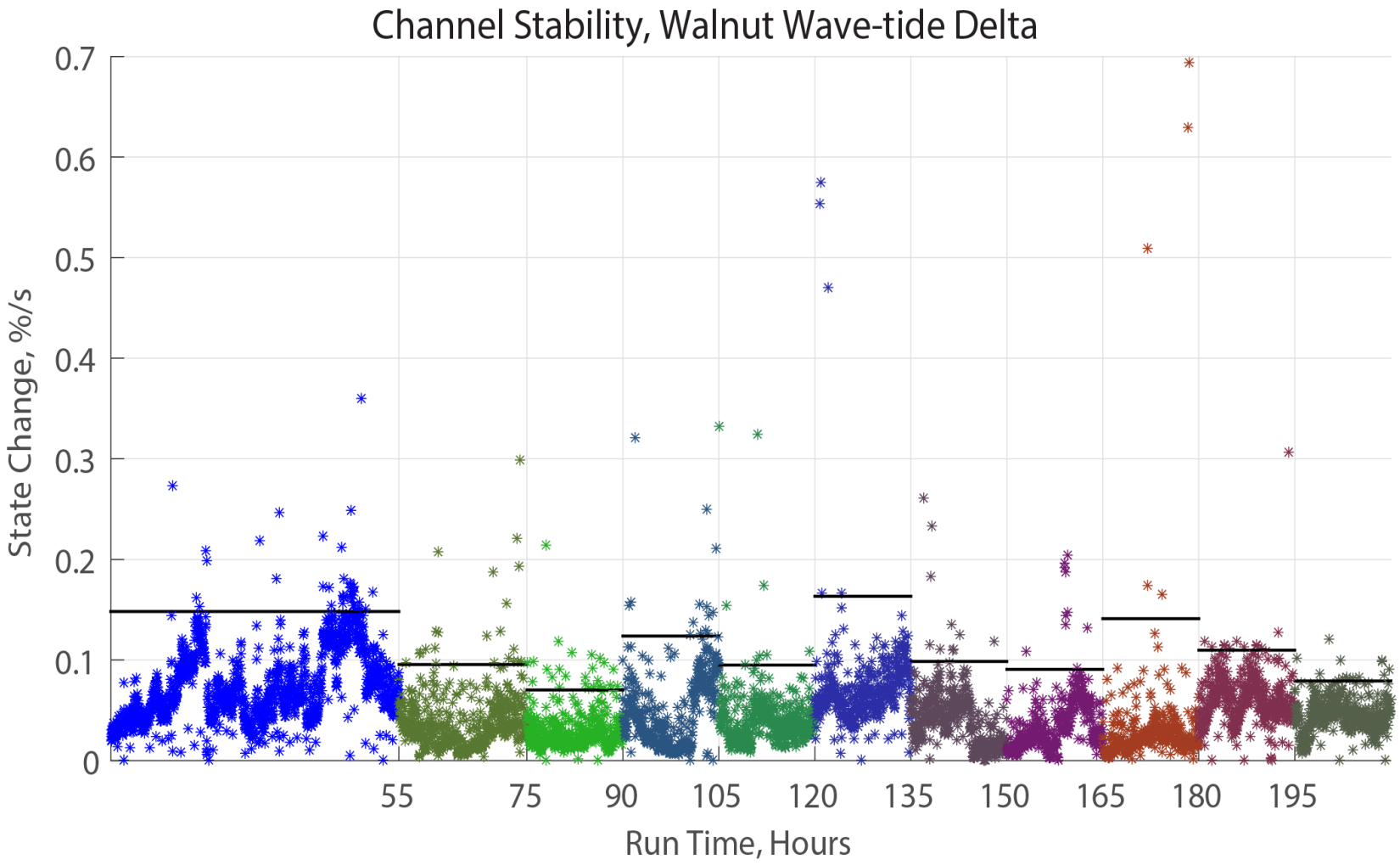
Channel Stability, Walnut Wave-tide Delta
State Change, %/s
0.7
0.6
0.5
0.4
0.3
0.2
0.1
0
55
75
90
105
120
135
150
165
180
195
Run Time, Hours

Figure 44 (previous page): Percent of topset changing state between land and water per second. Markers denote the value for each image pair; RGB value of pixels is set by the wave, tidal and fluvial energy proportion, respectively. Black bars show the lower limit of instantaneous change that could signal an avulsive event. The final 20 run hours are not shown because there was no fluvial input and thus no channels.

at which the channels are changing: shrinking, growing or migrating. A static system would have only a small background rate of change as minute fluctuations in discharge, bed elevation, base level and lighting cause pixels close to the land-water threshold value to flicker. Most value changes are restricted to the edges of the deposit and the area immediately adjacent to the fluvial channels (Fig. 43). Channel migration results in a sustained elevated rate of change as pixels on the cut bank are wetted and pixels on the lee side become dry. Hard avulsions are recorded as short-lived spikes in the rate of change as a river abruptly abandons its channel and occupies another. Changes around the edges of the deposit are caused by small fluctuations in lighting and base level.

We defined an avulsive event as one in which one or more sequential pairs show pixel change percentage values two standard deviations above the mean change rate for a phase (Fig. 44). The phases with the highest proportion of fluvial energy show the greatest 'background' rate of channel activity, but also tend to have the highest pairwise change rates. Both increased wave and increased tidal energy lead to lower rates of fluvial change: fewer avulsion cutoffs and fewer pixels changing value.

Discussion:

Subaerial delta area growth slowed—and even reversed—after the onset of tidal and wave forcing. In part, the decrease in growth rate is due to the progradation of the deposit past the edge of the subdelta: there was an abrupt increase in water depth—and thus accommodation—and the rate of new topset area creation decreased as a matter of mass balance. This does not account for the topset area loss, however. Base level, sediment, and water supply were held constant, and the land loss occurred over timescales (<5 run hours) too small to be the result of deposit-wide autogenic reorganization. Rather, we believe that the reduction and/or reversal of delta growth is the result of wave reworking, possibly combined with modification of underwater topography.

We observed the formation of a low barrier at the shoreline upon the onset of waves, and observation of the formation of the barrier suggests that most of the sediment forming it was transported onto the topset from the offshore by wave action. Consolidation of the topset into a locally thicker layer would lead to loss of area. Another potential cause of reduced topset area is the reorganization of the foreset: the slope of the offshore portion may have decreased due to the increased basinal energy, as suggested by the modeling work of Hutton and Syvitski (2008). The sediment to fill the extra volume required may have been supplied by the topset.

The development and persistence of blind channels cutting through the berm suggests that in that area, tidal forcing was stronger than wave transport. That these channels continued to form even at the highest proportion of wave energy (and that at

least some became defunct even at the highest proportion of tidal energy) suggests that basinal effects can become focused on small features and, locally, dominate even when the overall relative proportion of the effect is small. Thus we expect that as long as wave and/or tidal effects are present in a delta, even at very small relative levels, there will be locations where their signature is present in the morphology. This is consistent with, for example, the observations of Shaw and Mohrig (2014) that even the relatively weak tides in the Gulf of Mexico influence morphology in the generally river-dominated Wax Lake Delta, and the obvious presence of wave-generated barriers in the generally river-dominated Mississippi Delta.

Although there is a clear visible signature of waves and tides on delta morphology, the quantitative measures we used of geometric properties of the shoreline were generally only moderately correlated with the proportion of wave and tide energy impinging on it. The correlations were the strongest with the wave energy parameter, and confirm the visual observation that waves reduce shoreline roughness. Because waves act directly on the shoreline and only a short way into inlets, their energy is spent in a relatively narrow band, in comparison to fluvial and tidal processes, which are spread over the entire topset and the intertidal zone, respectively. This dilution of energy may partially explain the dominance of waves and wave-generated morphology at the shoreline regardless of the overall energy proportion (Fig. 45).

We observed channels to be more stable in the presence of increased wave and tidal energy. Thus we find that both waves and tides limit channel dynamics, although we believe that they do so in different ways. Wave action causes the formation of a low

barrier, through which the fluvial channel must cut to reach the basin. As predicted by the modelling work of Jerolmack and Swenson (2007), increased alongshore transport of sediment decreases the total number of distributary mouths the river could maintain at once, as well as suppresses the formation of new mouths. By redistributing sediment along shore, wave action also suppresses channel lengthening and the subsequent slope reduction that can also set the system up for avulsion.

The tidal mechanism for limiting channel migration and avulsion is somewhat different: ebb currents remove sediment from the mouths of the channels so efficiently that channel slope does not decrease with time, nor does the channel bed elevation rise with respect to the surrounding floodplain. This reduces the gravitational advantage that drives change in channel configuration on the topset, and thus stabilizes the channels.

Figure 45 (following page): Clockwise from top, overhead images from the phases with proportionally the most fluvial (run hour 45), wave (run hour 180), and tide (run hour 230) phases. Center, the phase with most equal proportions (run hour 140). Upper left, detail showing the development of berm-cutting, sinuous, mouth-widening tidal channels. Note that wave energy is confined to the portion of the deposit basinward of the shoreline parallel bar; tidal energy passes through this bar to the interior via inlets.

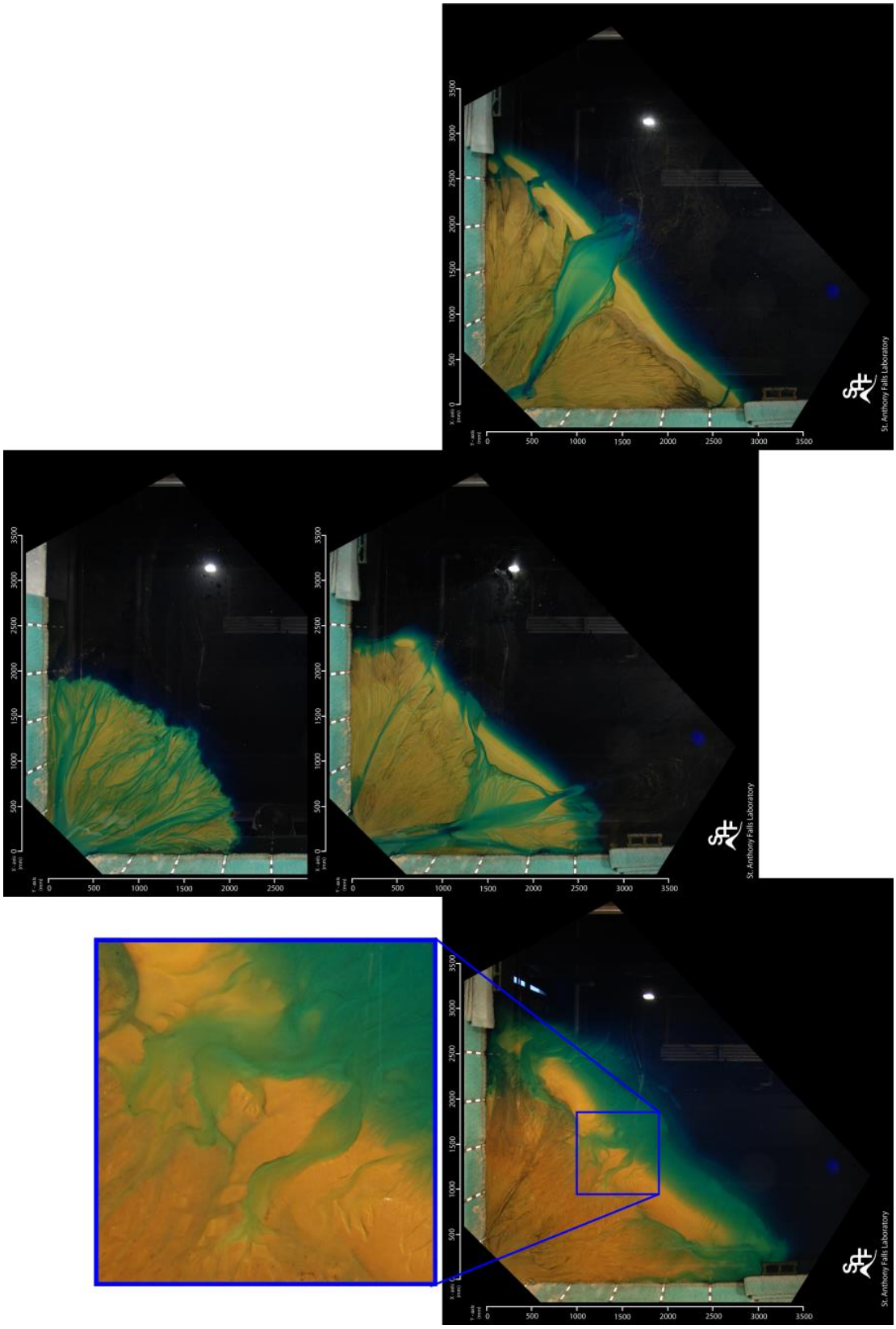
St. Anthony Falls Laboratory
St. Anthony Falls Laboratory
St. Anthony Falls Laboratory

Conclusions:

Using the delta basin facility at St. Anthony Falls Laboratory, a system of powerful pumps, and an oscillating arm, we have created laboratory-scale deltas that exhibit the morphological features most often associated with mixed wave and tidal influence in the field, including barriers, (persistent) tidal inlets, spaced tidal channels, smoothed shorelines, and alongshore migrating bars. From qualitative and quantitative analysis of overhead imagery and topographic scans, we find that:

- Laboratory deltas undergoing tidal and wave action of comparable strength display a mix of morphological features classically associated with each;
- Wave influence produces a distinctive smoothing of the shoreline that is only partially captured by quantitative measures of shoreline roughness
- The morphologic signature of tides combined with waves is an increase in the number of shoreline piercing points (inlets) as relative tidal energy increases
- Beyond the two effects above, simple quantitative geometric measures of static morphology are largely unsuccessful at capturing visible differences in morphology produced by differing proportions of fluvial, tidal and wave energies
- Both waves and tides substantially and measurably reduce the mobility of channels on the delta top. Thus, the chief difference between fluvial- and tidally-influenced deltas may be expressed via channel dynamics, rather than (quasi)static morphology.

Chapter 5:

In the previous four chapters we have 1) established the importance of deltas as a landscape, 2) introduced a new method for generating pseudotides and tidal morphologies in an experimental setting, 3) developed a global database of river mouth and delta locations, 4) developed metrics to quantify the relative strengths of the three main processes (fluvial, tidal and wave) that determine the planform shape of a delta, as well as 5) geomorphic metrics to measure their effects, and finally 6) applied both sets of metrics to experimental deltas under both wave and tide influence.

Our overall findings from this work are that:

1) a rapid, pseudosinusoidal variation in water surface elevation produces, to a first order, delta morphologies similar to features at the field scale interpreted to have formed under tidal influence,

2) that incident wave energy at a river mouth is a more effective indicator of whether there will be a delta there than either tidal energy or large-scale bathymetry,

3) that although features such as shoreline roughness, curvature and channel spacing are generally considered to be indicators of the dominant processes which act on a delta, quantitative measurements of these features and incident energy regimes show that they are not well correlated, and

4) that the shoreline of a delta, no matter how well described, may not hold geomorphic indicators for the relative strength of the fluvial and tidal energy delivery.

While this project has thus far not succeeded in our ultimate goal to create a full, quantitative version of Galloway's (1975) famous delta classification diagram, it has

succeeded in establishing the potential of quantitative geometric parameters for the description of planform morphologies and in the development of quantitative, physically-plausible, energy-based parameters to describe process strength. It has also pioneered the use of a pseudotide and wave generator to create tidal and wave-influenced morphologies as well as establishing that mixed wave and tidal morphologies do occur when the tidal and wave energy parameters are near parity. It has also led to the development of the first truly global survey of the distribution and occurrence of river mouths and their associated deltas.

Future Directions:

The ineffectiveness of our quantitative measures of delta geometry in terms of expressing the effects of wave, tide, and fluvial energy inputs is puzzling. Planform geometry has been used to qualitatively classify deltas since at least the early 1970s (see, e.g., Wright and Coleman, 1973, and Galloway, 1975) and has proven an effective—and true—enough system to be in widespread use today.

We believe that the various shoreline geometry measurements were computed correctly for the datasets we used. There then seem to be two possible explanations for their disappointing performance in comparison to the imposed tidal and wave forcing. One is that the metrics we applied do not measure the essential geometric properties of the delta that are so qualitatively apparent, in which case the problem is one that has vexed image analysts for years in many other applications (see, e.g., Preston, 1972, Penn *et al*., 1993 and Leite, and Filho, 2009), which is that it is sometimes difficult to teach a computer to discern patterns and features that are readily apparent to the human eye-brain

combination – facial recognition is a good example. In that case, a fruitful next step would be to attempt to use more sophisticated methods of analysis for the delta images, perhaps borrowing from fields such as computer vision (e.g., Schalkoff, R.J., 1989) and/or multi-point geostatistics (e.g., Pyrcz and Deustch, 2014).

For the field cases (Chapter 3), another possibility is that the average fluvial, tidal and wave conditions do not represent the energy that sets the geomorphic properties of the coastline. This is consistent with the observation that some of the measures (e.g. shoreline roughness) correlated better with the imposed energy conditions for the laboratory cases than in the field. Here, the next steps likely require more finely resolved data on, for example, storm-wave statistics than are generally available globally at present.

In addition to these ideas, I suggest that following avenues of investigation: First, a second round of analysis of the field delta database could focus on showing that the datasets (images) of the deltas analyzed for their geometry are in fact representative of the surrounding coastline and are not part of larger features (e.g. large-scale coastal capes) with different planform morphology.

Second, again focusing on the field data, it would be worth verifying that the tidal and wave data used are representative of the actual tidal regime and wave climate in the ultra-nearshore area: although we used the highest resolution data sets available, features below the scale of our models may cause conditions to differ from the predictions: e.g., Ashton and Murray (2006) present a compelling case for the significance of the angle of

approach of waves in influencing shoreline morphology. We could not account for this with the data that were available.

Third, it would be worthwhile to investigate the effects of the temporal variability in tide and wave intensity. We did not account for neap-spring cycles in our tidal range calculation: from the standpoint of energetics, the smaller tidal range during neap tide exactly balances the larger range during spring tide. Sediment transport is nonlinear with flow energy, however, and therefore the spring-neap cycle may not be balanced from a transport perspective. Similarly, as mentioned above, because we used daily average wave heights to generate our dataset, we did not account for the possibility that extreme events might set the morphology of a wave-influenced coast.

Finally, we return to a point made above: we must also develop metrics that more accurately describe the qualitative features of wave and tidal deltas that appear to be so obvious to the eye: although the metrics we presented here perform adequately to describe simple geometric aspects of the planform morphology, they apparently are not up to the task of fully extracting the essence of what we recognize as wave and tidal delta morphology.

Bibliography:

Ashton, A. D., and Giosan, L., 2011. Wave-angle control of delta evolution. Geophysical Research Letters 38, doi:10.1029/2011GL047630.

Ashton, A. D., and Murray, A. B., 2006. High-angle wave instability and emergent shoreline shapes: 1. Modeling of sand waves, flying spits, and capes. Journal of Geophysical Research 111, doi:10.1029/2005JF000422.

Ashton, A.D., Hutton, E.W.H., Kettner, A.J., Xing, F., Kallumadikal, J., Neinhuis, J. and Giosan, L., 2013. Progress in coupling models of coastline and fluvial dynamics. Computers and Geosciences 53, 21-29, doi: 10.1016/j.cageo.2012.04.004.

Aviso: The altimeter products were produced by Ssalto/Duacs and distributed by Aviso, with support from Cnes: http://www.aviso.altimetry.fr/duacs/

Battjes, J. A., 1974. Surf similarity. Proceedings of the 14th International Conference on Coastal Engineering, 466–480, American Society of Civil Engineers, New York.

Beltaos, S., 1997. Onset of river ice breakup. Cold Regions Science and Technology 25 (3), 183-196.

Bhattacharya, J.P., and Walker, R.G., 1991. River- and wave-dominated depositional systems of the Upper Cretaceous Dunvegan Formation, northwestern Alberta. Bulletin of Canadian Petroleum Geology 39 (2), 165-191.

Boyd, R., Dalrymple, R. and Zaitlin, B.A., 1992. Classification of clastic coastal depositional environments. Sedimentary Geology 80, 139-150.

Bryden, I.G., Grinsted, T., and Melville, G.T., 2005. Assessing the potential of a simple tidal channel to deliver useful energy. Applied Ocean Research 26, 198-204, doi:10.1016/j.apor.2005.04.001

Cohen, H.A., and McClay, K., 1996. Sedimentation and shale tectonics of the northwestern Niger Delta front. Marine and Petroleum Geology 13 (3), 313-328.

Cram, J.M., 1979. The Influence of Continental Shelf Width on Tidal Range: Paleoceanographic Implications. Journal of Geology 87 (4), 441-447.

D'Alpaos, A., Lanzoni, S. and Marani, M., 2005. Tidal network ontogeny: Channel initiation and early development. Journal of Geophysical Research 110, doi:10.1029/2004JF000182.

Davis, R. A., Jr., and Hayes, M. O., 1984. What is a wave-dominated coast? Marine Geology 60, 313-329.

Edmonds, D. A. and Slingerland, R. L., 2010. Significant effect of sediment cohesion on delta morphology. Nature Geoscience 3, doi: 10.1038/NGEO730.

Edmonds, D. A., Hoyal, D.C.J.D., Sheets, B.A., and Slingerland, R.L., 2009. Predicting delta avulsions: Implications for coastal wetland restoration. Geology 37, 759-762, doi: 10.1130/G25743A.1.

Edmonds, D. A., Paola, C., Hoyal, D. C. J. D., and Sheets, B. A., 2011. Quantitative metrics that describe river deltas and their channel networks. Journal of Geophysical Research 116, F04022, doi:10.1029/2010JF001955.

Fagherazzi, S., Gabet, E. J., and Furbish, J., 2004. The effect of bidirectional flow on tidal channel planforms. Earth Surface Processes Landforms 29, 295-309, doi: 10.1002/esp.1016.

Feder, Jens, 1988. Fractals. New York: Plenum.
Galloway, W.E., 1975. Process Framework for Describing the Morphologic and Stratigraphic Evolution of Deltaic Depositional Systems, in Deltas, M.L. Broussard, ed., Houston Geological Society, 87-98.
Geylense, N., Storms, J. E. A., Walstra, D. J., Jagers, H. R. A., Wang, Z. B. and Stive, M. J. F., 2011. Controls on river delta formation; insights from numerical modelling. Earth and Planetary Science Letters 302, 217-226, doi:10.1016/j.epsl.2010.12.013.
GRDC, The Global Runoff Data Centre, 56068 Koblenz, Germany, http://www.bafg.de/GRDC/EN/02_srvcs/21_tmsrs/riverdischarge_node.html
Han, M., Hou, J. and Wu, L., 1995. Potential Impacts of Sea-Level Rise on China's Coastal Environment and Cities: A National Assessment. Journal of Coastal Research, 14, 79-95.
Harris, P.T., Heap, A.D., Bryce, S.M., Porter-Smith, R., Ryan, D.A., and Heggie, D.T., 2002. Classification of Australian clastic coastal depositional environments based upon a quantitative analysis of wave, tidal and river power. Journal of Sedimentary Research 72 (6), 858-870.
Harris, P.T., Hughes, M.G., Baker, E.K., Dalrymple, R.W., and Keene, J.B., 2004. Sediment transport in distributary channels and its export to the pro-deltaic environment in a tidally dominated delta: Fly River, Papua New Guinea. Continental Shelf Research 24, 2431-2454, doi:10.1016/j.csr.2004.07.017.
Holodboroko, P., 2008. Smooth Noise Robust Differentiators. http://www.holoborodko.com/pavel/numerical-methods/numerical-derivative/smooth-low-noise-differentiators/
Hubbard, S. M., Smith, D. G., Nielsen, H., Leckie, D. A., Fustic, M., Spencer, R. J., and Bloom, L., 2011. Seismic geomorphology and sedimentology of a tidally influenced river deposit, Lower Cretaceous Athabasca oil sands, Alberta, Canada. AAPG Bulletin, 95 (7), 1123-1145, doi: 10.1306/12131010111.
Hutton, E. W. H. and Syvitski, J. P. M, 2008. Sedflux 2.0: An advanced process-response model that generates three-dimensional stratigraphy. Computers & Geosciences 34, 1319-1337, doi: 10.1016/j.cageo.2008.02.01.
Jerolmack, D. J., and Swenson, J. B., 2007. Scaling relationships and evolution of distributary networks on wave-influenced deltas. Geophysical Research Letters 34, L23402, doi:10.1029/2007GL031823.
Kamphuis, J.W., 1991. Alongshore Sediment Transport Rate. Journal of Waterway, Port, Coastal and Ocean Engineering 117 (6), 624-640.
Kim, W, Sheets, B. A., and Paola, C., 2012. Steering of experimental channels by lateral basin tilting, Basin Research 22, 286-301, doi: 10.1111/j.1365-2117.2009.00419.x.
Kim, W. and Jerolmack, D. J., 2008. The Pulse of Calm Fan Deltas. Journal of Geology 116, 315-330, doi: 10.1086/588830.
Kim, W., Paola, C., Swenson, J. B., and Voller, V. R., 2006. Shoreline response to autogenic processes of sediment storage and release in the fluvial system, Journal of Geophysical Research 111, F04013, doi:10.1029/2006JF000470.

Kleinhans, M.G., Van der Vegt, M., Terwisscha van Scheltinga, R., Baar, A.W. and Markies, H., 2012. Turning the tide: experimental creation of tidal channel networks and ebb deltas. Netherlands Journal of Geosciences 91-3, 311-323.

Komar, P.D., 1971. The Mechanics of Sand Transport on Beaches. Journal of Geophysical Research 76 (3), 713-721.

Lanzoni, S. and D'Alpaos, A., 2015. On funneling of tidal channels, Journal of Geophyical Research 120, 433-452, doi:10.1002/2014JF003203.

Legler, B., Johnson, H.D., Hampson, G.J., Massart, B.Y.G., Jackson, C.A-L., Jackson, M.D., El-Barkooky, A., and Ravnas, R., 2013. Facies model of a fine-grained, tide-dominated delta: Lower Dir Abu Lifa Member (Eocene), Wester Desert, Egypt. Sedimentology 60, 1313-1356, doi: 10.1111/sed.12037.

Leopold, L. and Maddock, T., 1953. The Hydraulic Geometry of Stream Channels and Some Physiographic Implications. USGS Professional Paper 252, U.S. Government Printing Office, Washington, D.C.

Longhitano, S. G., Mellere, D., Steel, R. J. and Ainsworth, R. B., 2012. Tidal depositional systems in the rock record: A review and new insights. Sedimentary Geology 279, 2-22, doi: doi:10.1016/j.sedgeo.2012.03.024

Lorenzo-Trueba, J., Voller, V. R., Paola, C., Twilley, R. R., and Bevington, A. E., 2012. Exploring the role of organic matter accumulation on delta evolution. Journal of Geophysical Research, 117, F00A02, doi:10.1029/2012JF002339.

Marciano, R., Wang, Z.B., Hibma, A. and De Vriend, H.J., 2005. Modeling of channel patterns in short tidal basins. Journal of Geophysical Research 110, doi:10.1029/2003JF000092.

Martin, J., Sheets, B., Paola, C., Hoyal, D., 2009. Influence of steady base-level rise on channel mobility, shoreline migration, and scaling properties of a cohesive experimental delta. Journal of Geophysical Research 114, F03017, doi:10.1029/2008JF001142.

Meybeck, Michel and Ragu, Alain, 2012. GEMS-GLORI world river discharge database. Laboratoire de Géologie Appliquée, Université Pierre et Marie Curie, Paris, France, doi:10.1594/PANGAEA.804574.

Miall, A. D. (1976), Facies Models 4. Deltas, Geoscience Canada, 3(3), 215-227.

Milliman, J. D., and Syvitski, J. P. M., 1992. Geomorphic/tectonic control of sediment discharge to the ocean: the importance of small mountainous rivers. Journal of Geology 100, 525–544.

Milliman, J.D. and Farnsworth, K.L., 2011. River Discharge to the Coastal Ocean: a global synthesis. Cambridge University Press.

Muto, T. and Steel, R. J., 1992. Retreat of the front in a prograding delta. Geology 20, 967-970

Neinhius, J. H., Ashton, A. D., Poos, P.C., Hulscher, S.J.M.H., and Giosan, L., 2013. Wave reworking of abandoned deltas. Geophysical Research Letters 40, 5899-5903, doi: 10.1002/2013GL058231, 2013.

Orton, G.J, and Reading, H. G., 1993. Variability of deltaic processes in terms of sediment supply, with particular emphasis on grain size. Sedimentology, 40, 475-512.

Padman, L. and Erofeeva, L. OSU tidal inversion software documentation. Source: http://polaris.esr.org/ptm_index.html (accessed 11/30/2015)

Paola, C. and Voller, V.R., 2005. A generalized Exner equation for sediment mass balance. Journal of Geophysical Research, 110, doi:10.1029/2004JF000274.

Paola, C., Straub, K., Mohrig, D., and Reinhardt, L., 2009. The "unreasonable effectiveness" of stratigraphic and geomorphic experiments. Earth-Science Reviews, 97, 1-43, doi: 10.1016/j.earscirev.2009.05.003

Parker, G., Wilcock, P.R., Paola, C., Dietrich, W.E., and Pitlick, J., 2007. Physical basis for quasi-universal relations describing bankfull hydraulic geometry of single-thread gravel bed rivers. Journal of Geophysical Research 112, doi:10.1029/2006JF000549.

Piper, D.J.W., Kontopoulos, N., Anagnostou, C., Chronis, G., and Panagos, A.G., 1990. Modern Fan Deltas in the Western Gulf of Corinth, Greece. Geo-marine Letters, 10 (1), 5-12, doi: 10.1007/BF02431016.

Pyrcz, M. J. and Deustch, C.V., 2014. Geostatistical Reservoir Modeling, 2nd ed., OUP USA.

Rainwater, E. H. (1966), The Geological Importance of Deltas, in Deltas in Their Geologic Framework, edited by M.L. Shirley, 1-15.

Reimnitz, E., and Bruder, K.F., 1972. River Discharge into an Ice-Covered Ocean and Related Sediment Dispersal, Beaufort Sea, Coast of Alaska. Geological Society of America Bulletin 83 (3), 861-866.

Reitz, M. D., and Jerolmack, D. J., 2012. Experimental alluvial fan evolution: Channel dynamics, slope controls, and shoreline growth. Journal of Geophysical Research 117, F02021, doi:10.1029/2011JF002261

Reitz, M. D., Jerolmack, D. J., and Swenson, J. B., 2010. Flooding and flow path selection on alluvial fans and deltas. Geophysical. Research Letters 37, L06401, doi:10.1029/2009GL041985.

Schaefer, R. W., 2011. What *Is* a Savitzky-Golay Filter? IEEE Signal Processing Magazine, doi: 10.1109/MSP.2011.941097.

Schalkoff, R.J., 1989. Digital image processing and computer vision. Wiley and Sons, Australia.

Schulze, K., Hunger, M. and Döll, P., 2005. Simulating river flow velocity on global scale. Advances in Geosciences 5, 133-136.

Shaw, J.B. and Mohrig, D., 2014. The importance of erosion in distributary channel network growth, Wax Lake Delta, Louisiana, USA. Geology, 42 (1), 31-34, doi:10.1130/G34751.1.

Syvitski, J. P. M and Milliman, J. D., 2007. Geology, Geography and Humans Battle for Dominance over the Delivery of Fluvial Sediment to the Coastal Ocean. Journal of Geology 115 (1), 1-19.

Syvitski, J. P. M., Vörösmarty, C., Kettner, A. J. and Green, P., 2005. Impact of humans on the flux of terrestrial sediment to the global coastal ocean. Science 308, 376–380

Syvitski, J. P.M., Kettner, A. J., Overeem, I., Hutton, E. W. H., Hannon, M. T., Brakenridge, G. R., Day, J., Vörösmarty, C., Saito, Y., Giosan, L., Nicholls, R. J., 2009. Sinking deltas due to human activities. Nature Geoscience 2, 681-686, doi: 10.1038/ngeo629

U.S. Army Corps of Engineers, 2002. EM 1110-2-1100, Coastal Engineering Manual (CEM), Part III, Chapter 2: Longshore Sediment Transport.

Vlaswinkel, B.M., and Cantelli, A., 2011. Geometric characteristics and evolution of a tidal channel network in experimental setting. Earth Surface Processes and Landforms 36, 739-753, doi: 10.1002/esp.2099.

Vörösmarty, C.J., Moore, B., Grace, A., and Gildea, M.P., 1989. Continental scale models of water balance and fluvial transport: an application to South America. Global biogeochemical cycles 3 (3), 241-265.

Walcott, R. I., 1972. Late Quaternary Vertical Movements in Eastern North America: Quantitative Evidence of Glacio-Isostatic Rebound. Reviews of Geophysics and Space Physics, 10 (4), 849-884.

Wickert, A.D., Martin, J.M., Tal, M., Kim, W. Sheets, B., and Paola, C., 2013. River channel lateral mobility: metrics, time scales, and controls. Journal of Geophysical Research: Earth Surface 188, 396-412, doi:10.1029/2012JF002386.

Willis, B.J., Bhattacharya, J.P., Gabel, S.L., and White, C.D., 1999. Architecture of a tide-influenced river delta in the Frontier Formation of central Wyoming, USA. Sedimentology 46, 667-688.

Wilson, C.A. and Goodbred, S.L, 2015. Construction and Maintenance of the Ganges-Brahmaputra-Meghna Delta: Linking Process, Morphology and Stratigraphy. Annual Review of Marine Science 7, 67-88, doi: 10.1146/annurev-marine-010213-135032

Wright, L. D., Coleman, J. M., and Thom, B. G., 1973. Processes of Channel Development in a High-Tide-Range Environment: Cambridge Gulf-Ord River Delta, Western Australia. Journal of Geology 81, 15-41.

Wright, L.D. and Coleman, J. M., 1972. River Delta Morphology: Wave Climate and the Role of the Subaqueous Profile. Science 176 (4032), 282-284.